INSTITUTO POLITÉCNICO DE BRAGANÇA
Escola Superior de Tecnologia e Gestão

ADSORPTION OF CO_2, CH_4 AND N_2 IN POWDER AND BINDER-FREE ZEOLITE 13X

IKRAM BEN CHEIKH

THESIS PRESENTED TO
ESCOLA SUPERIOR DE TECNOLOGIA E GESTÃO
INSTITUTO POLITÉCNICO DE BRAGANÇA
TO OBTAIN A MASTER'S DEGREE IN
CHEMICAL ENGINEERING

SUPERVISOR
PROF. DOCTOR JOSÉ ANTÓNIO CORREIA SILVA

BRAGANÇA, PORTUGAL
OCTOBER, 2025

Acknowledgement

I wish to begin by expressing my profound gratitude to God, whose guidance, strength, and grace have illuminated every step of my personal and academic journey. His constant presence has sustained me through the challenges and milestones that shaped this work.

My deepest appreciation goes to my family and to my husband, whose unwavering love, patience, and encouragement have been an unfailing source of strength and motivation. Their faith in me has inspired perseverance and commitment throughout this demanding yet rewarding journey.

I extend my sincere and heartfelt thanks to my supervisor, Professor José António Correia Silva, for his exceptional mentorship, continuous guidance, and intellectual insight. His expertise, trust, and constructive feedback have been invaluable in shaping the direction and quality of this research.

I am also sincerely grateful to Ezzeldin Aly for his dedicated technical assistance and valuable support during the experimental phase of this study. My special thanks are equally extended to Kristin Gleichmann from Chemiewerk Bad Köstritz GmbH (Germany) for generously providing the zeolite materials used in this research a contribution that was instrumental to the success of this project.

Finally, I would like to convey my heartfelt appreciation to all those who have encouraged, supported, and believed in me throughout this academic pursuit. To all who genuinely care for me and have shared in my efforts, challenges, and achievements your kindness and faith have made this journey deeply meaningful.

ABSTRACT

The increasing concentration of greenhouse gases (GHGs), particularly CO_2, is a main driver of climate change, demanding effective mitigation strategies. Carbon Capture and Storage (CCS) technologies, especially adsorption-based processes using porous materials, offer an efficient route to reduce CO_2 emissions from industrial sources. Zeolite 13X has gained prominence due to its high surface area, well-defined pore structure, and strong affinity toward CO_2. While typically synthesised in powder form, the use of commercial binder-free Zeolite 13X (13X-BF) beads may offer potential advantages over conventional structures, including improved mechanical strength, enhanced mass transfer, and a higher effective capacity due to the reduced presence of inert components.

This work systematically investigates the adsorption equilibrium of CO_2, CH_4, and N_2 on both lab-agglomerated powder (13X-P) as synthesised and commercial binder-free (13X-BF) forms of zeolite 13X. A custom fixed-bed unit was used to measure breakthrough curves at temperatures of 308,328 and 348 K and partial pressures ranging from 10 to 350 kPa to measure adsorption equilibrium isotherms. The experimental equilibrium data were rigorously fitted using the Langmuir model for N_2 and CH_4 and the Dual-Site Langmuir (DSL) model for CO_2.

The 13X-BF material exhibited a superior thermodynamic performance comparable to the pure lab-agglomerated powder (13X-P) as synthesised. Adsorption equilibrium capacities followed the order $CO_2 > N_2 > CH_4$. At 308 K and 150 kPa, the maximum uptake reached 7.57 mol·kg^{-1} for 13X-BF, even outperforming the 7.11 mol·kg^{-1} observed on 13X-P. Under typical post-combustion conditions (15% CO_2, 308K, 101kPa), 13X-BF achieved a superior CO_2/N_2 selectivity of 70, comparable to 61 observed for the 13X-P.

The working capacity performance parameter (important for cyclic processes such as PSA and TSA) highlighted also a critical operational trade-off: 13X-BF exhibited a working capacity of 3.10 mol.kg^{-1} under aggressive deep vacuum regeneration (in the pressure range 100 to 3 kPa at 308 K) compared to 2.56 mol.kg^{-1} to the 13X-P. However, 13X-P performed slightly better under milder vacuum regeneration (10 kPa and 15 kPa). Overall, the results indicate that commercial binder-free Zeolite 13X preserves the intrinsic adsorption characteristics of the powder form while providing comparable adsorption capacity, selectivity, working capacity and mechanical

viability, suggesting its potential suitability for adsorption processes such as PSA and VPSA for CO_2 capture and biogas purification.

Keywords: Zeolite 13X; Binder-free adsorbents; CO_2 adsorption; Dual-Site Langmuir model; Breakthrough curves; Working capacity; PSA/VPSA processes; Biogas purification.

RESUMO

O aumento da concentração de gases com efeito de estufa (GEE), em particular do dióxido de carbono (CO_2), constitui uma das principais causas das alterações climáticas, exigindo estratégias de mitigação eficazes. As tecnologias de Captura e Armazenamento de Carbono (CCS), especialmente os processos baseados em adsorção com materiais porosos, oferecem uma via eficiente para reduzir as emissões de CO_2 provenientes de fontes industriais. O zeólito 13X tem ganho destaque devido à sua elevada área superficial, estrutura de poros bem definida e forte afinidade para o CO_2. Embora seja normalmente sintetizado sob a forma cristalina em pó com um tamanho na ordem micrométrica, a utilização sob a forma de partículas esféricas com tamanho na ordem dos milímetros e isenta de ligante (13X-BF) para a aglomeração dos cristais, apresenta vantagens potenciais em relação às estruturas convencionais, nomeadamente maior resistência mecânica, melhor transferência de massa e maior capacidade efetiva, resultante da ausência de componentes inertes.

Neste trabalho investigou-se de forma sistemática o equilíbrio de adsorção do CO_2, CH_4 e N_2 no zeólito 13X nas seguintes formas comerciais: i) cristais micrométricos aglomerados pós-síntese (13X-P) e ii) na forma de partículas esféricas comerciais "Binder-Free" (13X-BF). O estudo foi realizado numa unidade de leito fixo dedicada para medir curvas de rutura a temperaturas de 308, 328 e 348 K e pressões parciais compreendidas entre 10 e 350 kPa através de uma técnica cromatográfica. Os dados experimentais de equilíbrio de adsorção foram ajustados utilizando o modelo de Langmuir para o N_2 e o CH_4, e o modelo de Langmuir de Duplo Sítio (DSL) para o CO_2.

O material 13X-BF apresentou de forma consistente um desempenho termodinâmico semelhante ao material cristalino sintetizado. As capacidades de adsorção seguiram a ordem CO_2 > N_2 > CH_4. A 308 K e 150 kPa, a capacidade máxima de adsorção de CO_2 atingiu 7,57 mol·kg^{-1} para a 13X-BF, superando mesmo os 7,11 mol·kg^{-1} obtidos para a 13X-P. Em condições típicas de pós-combustão (15% de CO_2, 308 K, 101 kPa), a 13X-BF atingiu uma seletividade CO_2/N_2 de 70, comparável com a observada para a 13X-P (61).

A análise da capacidade de trabalho, um parâmetro de relevância industrial em processos PSA e TSA, evidenciou um compromisso operacional importante: o zeólito 13X-BF apresentou uma capacidade de trabalho 21% superior (3,10 mol·kg^{-1}) sob regeneração a vácuo (3 kPa), quando

comparada com a 13X-P (2,56 $mol \cdot kg^{-1}$). No entanto, a 13X-P apresentou desempenho ligeiramente superior em condições de regeneração a vácuo moderado (10 e 15 kPa).

De forma geral, os resultados indicam que a zeólita 13X-BF comercial, preserva as características intrínsecas de adsorção da forma em pó e apresenta um desempenho de adsorção e uma estabilidade mecânica comparáveis, evidenciando o seu potencial para aplicação em processos PSA e VPSA destinados à captura de CO_2 e/ou à purificação de biogás.

Palavras-chave: Zeólita 13X; Adsorventes sem aglutinante; Adsorção de CO_2; Modelo Dual-Site Langmuir; Curvas de breakthrough; Capacidade de trabalho; Processos PSA/VPSA; Purificação de biogas.

Table of Contents

INDEX OF FIGURES

INDEX OF TABLES

LIST OF ABBREVIATIONS

Nomenclature

$b_{1,2}$	Adsorption affinity constant of adsorption sites 1 and 2, respectively (kPa $^{-1}$)
b_∞	Adsorption affinity constant at infinite temperature (kPa $^{-1}$)
b_i	Adsorption affinity constant of component i (kPa $^{-1}$)
C_{0i}	Initial gas-phase concentration of component i at the inlet of the bed (mol.m^{-3})
F_0	Molar flow rate at the inlet of the bed (mol. s $^{-1}$)
F_i	Molar flow rate of component i (mol. s $^{-1}$)
m_s	Adsorbent mass in the column (kg)
p	Partial pressure (kPa)
p_i	Partial pressure of component i, respectively (kPa)
q	Adsorbed concentration at equilibrium conditions (mol.kg^{-1})
q_m	The maximum adsorbed concentration capacity (mol.kg^{-1})
$q_{mi,j}$	The maximum adsorbed concentration capacity at sites i, j (mol.kg^{-1})
R	Universal gas constant (J.mol^{-1}.K^{-1})
t	Time (min)
t_n	Saturation time (s)
T	Temperature, (K)
Q	Volumetric flow rate of the mobile phase (m ^{3} .s $^{-1}$)
V_c	Column volume (m^3)
ΔH	Heat of adsorption (kJ .mol $^{-1}$)
ΔH_i	Heat of adsorption of component i (kJ .mol $^{-1}$)

$\alpha_{i/j}$	Ideal selectivity of component i over component j (–)
β_i	Working capacity of component i (mol .kg $^{-1}$)
$\beta_{1,2,3}$	Working capacity under conditions 1, 2, and 3 (mol .kg $^{-1}$)
ε_b	Bed porosity (–)

Abbreviations

CCS	Carbon Capture and Storage
CCU	Carbon Capture and Utilization
CLC	Chemical looping combustion
CWK	Chemiewerk Bad Köstritz
DAC	Direct air capture
DSL	The Dual-Site Langmuir model
FAU	Faujasite-type zeolite
GHGs	Greenhouse gases
IEA	International Energy Agency
IUPAC	The International Union of Pure and Applied Chemistry
IZA	International Zeolite Association
LTA	Linde Type A zeolite
MOFs	Metal-organic frameworks
PCC	Post-combustion capture
PSA	Pressure swing adsorption
TSA	Temperature swing adsorption
VPSA	Vacuum pressure swing adsorption
VSA	Vacuum swing adsorption

Motivation

The escalating concentration of greenhouse gases (GHGs), particularly carbon dioxide (CO_2), in the atmosphere is a primary driver of climate change, demanding urgent and effective mitigation strategies. Carbon Capture and Storage (CCS) technologies offer a promising pathway to reduce CO_2 emissions from both industrial sources and the atmosphere. Among these technologies, adsorption processes using porous materials, especially zeolites, have emerged as a leading approach due to their potential for high selectivity and regenerability.

Zeolite 13X, a crystalline aluminosilicate with a well-defined pore structure and high surface area, exhibits a strong affinity for CO_2. While Zeolite 13X is synthesized in powder form, the development and application of binder-free Zeolite 13X structures (beads or pellets) offer potential advantages, including improved mass transport, higher adsorption capacities (potentially), and reduced material costs due to the absence of binders. However, a direct comparison of the CO_2, CH_4, and N_2 adsorption behavior of commercial binder-free beads or pellets versus powdered Zeolite 13X (consisting of fine crystals) is lacking, creating a critical knowledge gap to understand the effect of aggregation of the powder to form the binder-free particles used directly in fixed beds in cyclic industrial operations.

This research aims to address this gap by systematically investigating the adsorption equilibrium of CO_2, CH_4, and N_2 on both commercial binder-free beads and powdered Zeolite 13X as directly synthesized. By measuring single- and multi-component adsorption isotherms at varying temperatures and pressures, this study will: (1) determine the relative adsorption performance of the two Zeolite 13X structures (binder-free and powder) for CO_2 capture in the presence of CH_4 and N_2 (representative of biogas or flue gas mixtures); (2) elucidate the influence of binder presence/absence on the adsorption mechanisms and selectivity; and (3) provide fundamental data for the design and optimization of advanced CO_2 capture technologies and biogas purification processes.

Objective

This study aims to investigate the adsorption behaviour of CO_2, CH_4, and N_2 on powdered and commercial beads of binder-free 13X zeolites. Equilibrium adsorption isotherms will be measured at temperatures of 308, 328, and 348 K and pressures up to 350 kPa. The research will be divided into two key separation processes: CO_2/N_2 for post-combustion CO_2 capture and CO_2/CH_4 for biogas upgrading. Additionally, the adsorption capacity and performance of the zeolite 13 X in both forms will be explored to provide insight into its ideal selectivity and working capacity in realistic gas separation scenarios.

For that a comparative analysis of the adsorption equilibrium between 308,328 and 348 K and pressures up to 350 kPa on both powdered (as synthesized) and commercial binder-free beads of 13X zeolites will be measured to assess the impact on adsorption capacity, selectivity, working capacities and kinetic properties. The adsorption data will be modeled using isotherm equations such as Langmuir and Extended Langmuir, which will support the optimization of CO_2 separation processes in industrial applications. We expect that the findings will contribute for better understanding and improving commercial adsorbent materials for carbon capture technologies by addressing the impact of the formation of beads/pellets from the powder for industrial operations.

Structure of the Thesis

This dissertation is structured into six chapters, which together outline the progression of the research from theoretical foundations to the final conclusions and recommendations for future work.

Chapter 1 provides the theoretical framework, presenting the main concepts, principles, and studies relevant to the subject under investigation.

Chapter 2 details the materials employed, and the experimental procedures followed, covering all stages of preparation, operation, and characterization that supported the study.

Chapter 3 reports the results obtained and offers a critical discussion of their scientific and technical implications.

Chapter 4 synthesises the key conclusions drawn from the research and identifies potential directions for further development.

Chapter 5 compiles all bibliographic references cited throughout the dissertation, formatted according to the required academic standards.

Finally, Chapter 6 includes supplementary information considered relevant, such as preliminary tests and supporting data that contributed to the development of the work.

Chapter 1
State of Art and Study of Tools

1. Literature review

1.1. Introduction Climate Change, CO2 Emissions

Climate change is an undeniable reality, posing urgent environmental and political challenges due to its growing impact on ecosystems and future generations. While natural climate variations have occurred throughout history, the past century has seen a dramatic acceleration, primarily driven by human activities and the excessive emission of greenhouse gases (GHGs) (Magalhães Ferreira, 2018).

GHGs vary in type and global warming potential, with carbon dioxide (CO_2), methane (CH_4), and nitrous oxide (N_2O) being the most significant contributors. These gases occur naturally in the atmosphere but have increased substantially due to fossil fuel combustion, deforestation, agriculture, and industrial processes (Stern, 2016). Among them, CO_2 is the most prevalent, accounting for about 76% of global anthropogenic emissions, followed by CH_4 (16%) and N_2O (6%) (European Parliament, 2023; IPCC, 2023). Fossil fuels, which supply over 80% of the world's energy demand, contribute to approximately 90% of CO_2 emissions, leading to severe consequences such as rising sea levels and ocean acidification (Selim et al., 2024).

To mitigate CO_2 emissions, countries are adopting various strategies, including improving energy efficiency, transitioning to low-carbon fuels like hydrogen and nuclear power, expanding renewable energy (e.g., solar, wind, bioenergy), and employing geoengineering solutions such as afforestation and reforestation (Leung et al., 2014). Another critical approach is Carbon Capture and Storage (CCS), which has gained significant attention for its potential to reduce emissions from industrial sources and power plants while the energy sector transitions to cleaner technologies.

CCS captures CO_2 before its release into the atmosphere and can be classified into three main methods: pre-combustion, oxy-fuel combustion, and post-combustion capture (Lins et al., 2012). Among these, post-combustion capture is particularly attractive due to its compatibility with existing power plants, enabling widespread implementation without requiring major infrastructure changes.

Several CO_2 separation technologies have been developed to improve capture efficiency, including chemical and physical absorption, pressure and temperature swing adsorption

(PSA/TSA), membrane separation, and cryogenic separation. Among these, adsorption-based methods, particularly PSA and TSA, have been widely studied due to their high selectivity, energy efficiency, and scalability (Meng et al., 2020).

Solid adsorbents have gained prominence for CO_2 capture due to their high selectivity at low pressures, reusability, and relatively low investment costs (Figueroa et al., 2008). These materials are typically used in fixed or fluidized bed columns, where CO_2 is selectively adsorbed from gas mixtures. However, the efficiency of adsorption-based systems depends largely on the choice of adsorbent material and the regeneration strategy. In recent years, zeolites have been extensively studied due to their thermal stability, tunable porosity, and strong CO_2 affinity (Pera-Titus, 2013). Compared to conventional liquid absorption methods, solid sorbents generally require less energy and have already been successfully applied in natural gas processing and other industrial applications (Berg et al., 2019).

Biogas upgrading is another key process for reducing GHG emissions, as it involves removing CO_2 from raw biogas to produce high purity biomethane. According to the International Energy Agency (IEA), Carbon Capture, Utilization, and Storage (CCU and CCS) are essential for achieving net-zero emissions. While CO_2 is often treated as a waste product, it can also be used as a valuable resource for producing fuels, chemicals, and building materials. Unlike fossil-based CO_2, biogenic CO_2 such as that derived from biogas upgrading does not contribute to net climate change, as it originates from short-term carbon cycles.

Despite its potential, CCU is not yet widely integrated into biogas systems, and CO_2 from biogas upgrading is typically released into the atmosphere. Future advancements in CCU could enhance the sustainability of biomethane plants, particularly as demand for renewable carbon sources and biomethane production continues to grow (Cordova et al., 2023).

Additionally, adsorption-based technologies, including zeolites, could play a key role in optimizing CO_2 removal in both biogas upgrading and post-combustion gas separation, as well as in other industrial applications.

1.1.1. Carbon Capture and Storage (CCS)

Carbon capture and storage (CCS) is a crucial technology for reducing CO_2 emissions from industrial sectors and power generation. The choice of CO_2 capture method depends on factors such as the emission source, gas composition, and process conditions. The primary approaches include post-combustion, pre-combustion, and oxy-fuel combustion (Wilberforce et al., 2020). Additionally, emerging technologies such as chemical looping combustion (CLC) and direct air capture (DAC) offer alternative pathways for CO_2 removal (Dubey & Arora, 2022). In addition to traditional CCS applications, biogas upgrading is another important process that involves CO_2 separation.

1.1.2. Post-Combustion CO_2 Capture

Post-combustion capture is one of the most studied methods for reducing CO_2 emissions because it can be added to existing power plants and industrial facilities without major changes. This process removes CO_2 from flue gases after fuel combustion, making it a practical option for emission control (Metz et al., 2005). Since fossil fuels burn in air, the flue gas mainly contains nitrogen (N_2), oxygen (O_2), water vapor, and CO_2, with CO_2 concentrations ranging from 3% to 15%, depending on the fuel type (D'Alessandro et al., 2010). The main challenge is to separate CO_2 efficiently while keeping energy use and costs low (Wang et al., 2011).

One major benefit of post-combustion capture is that it works with current infrastructure. Several technologies can be used for CO_2 separation, including chemical absorption, adsorption, membrane separation, and cryogenic methods (Di Gianfrancesco, 2017). The effectiveness of each method depends on factors like material selectivity, energy needed for regeneration, and tolerance to gas impurities. Among these options, adsorption-based processes, such as pressure swing adsorption (PSA) and temperature swing adsorption (TSA), are promising due to their lower energy consumption compared to chemical absorption (Meng et al., 2020).

1.1.3. CO_2 Separation from Biogas

CO_2 separation is also important for biogas upgrading, where raw biogas is purified to produce high-quality biomethane. Biogas comes from the breakdown of organic materials, such as agricultural waste and sewage sludge, through anaerobic digestion. It mainly consists of methane (CH_4) and carbon dioxide (CO_2), along with small amounts of other gases like hydrogen sulfide (H_2S), nitrogen (N_2), oxygen (O_2), and water vapor. Methane is a strong greenhouse gas, with a global warming potential 28 times higher than CO_2 (Pinault, 2018). Therefore, capturing and using it efficiently is essential for both energy production and environmental protection. The energy value of biogas depends on methane concentration, so CO_2 removal is necessary to improve its quality for industrial use (Silva & Rodrigues, 2014). Similar to post-combustion capture, biogas upgrading can be done using chemical absorption, membrane separation, cryogenic methods, and adsorption-based techniques like PSA.

1.1.4. Pre-Combustion Capture

The carbon capture process in pre-combustion systems involves converting the fuel into a mixture of H_2 and CO_2 using oxygen or steam. After this step, CO_2 can be separated from H_2, allowing pure hydrogen to be burned with air. The separation of CO_2 from H_2 can be achieved through absorption, adsorption, or membranes, with the objective of separating CO_2 from the fuel to produce a hydrogen-rich stream, thereby reducing carbon emissions (Plasynski et al., 2009). During the separation process, CO_2 is initially dissolved in solvents under high pressure and subsequently released as the pressure is reduced. However, solvent regeneration typically requires heat to release the captured CO_2. Since CO_2 can be released at a pressure above atmospheric levels, the energy requirements for CO_2 capture and compression in pre-combustion systems can be significantly lower than in post-combustion systems, depending on the specific technology and process conditions. Another significant advantage of pre-combustion systems is the higher concentration of CO_2 in the gas stream, which facilitates its separation (Pires et al., 2011). However, these systems face challenges, such as the reduction in efficiency of the fuel

conversion process due to the additional steps required for gasification and CO_2 separation (Gibbins & Chalmers, 2008).

1.1.5. Oxy-Fuel Combustion Capture

Combustion with oxyfuel (O_2), also known as oxyfuel, is a process in which pure oxygen is used instead of air for combustion. As a result, the gases produced consist almost exclusively of CO_2 and water vapor, which can be removed by cooling and compression, generating a practically pure CO_2 stream. Although oxyfuel does not require a post-combustion capture device, the process demands gas treatment to remove impurities and pollutants such as sulfur oxides, nitrogen oxides, and particulate matter. This step is essential to meet environmental standards and CO_2 purity requirements before storage. Additionally, the use of pure oxygen typically requires a prior purification stage, with oxygen purity levels often ranging between 95% and 99%, depending on the specific process and application. This purification process is often carried out using cryogenic air rectification, although other methods such as pressure swing adsorption (PSA) or vacuum pressure swing adsorption (VPSA) can also be employed (Metz et al., 2005; Gür, 2022).

1.1.6. Chemical Looping Combustion (CLC)

Chemical looping combustion (CLC) is a novel approach that inherently separates CO_2 during combustion, eliminating the need for additional separation steps. Uses metal oxides (such as Fe_2O_3 or NiO) act as oxygen carriers, transferring oxygen from the air to the fuel in a cyclic process (Dubey & Arora, 2022). The absence of nitrogen in the process improves efficiency and reduces energy penalties compared to conventional oxy-fuel combustion (Raganati et al., 2021).

1.1.7. Direct Air Capture (DAC)

Direct air capture (DAC) is an advanced technology designed to remove CO_2 directly from ambient air using liquid or solid sorbents (Dubey & Arora, 2022). Unlike other CCS methods, which

capture CO_2 from point sources, DAC can reduce atmospheric CO_2 concentrations, making it a crucial tool for achieving net-zero emissions, offering a long-term decarbonization pathway but facing challenges in cost and scalability (Lorenzo et al., 2021, Wilberforce et al., 2020).

The various CO_2 capture routes presented in this section require the integration of CO_2 capture and separation technologies, namely: absorption, adsorption, cryogenic separation, membrane-based separation, and ionic liquids, among others. These technologies are employed in combination with CO_2 capture methods to effectively extract and purify CO_2 from fuel or flue gas streams.

1.2. CO_2 Separation Processes and Technologies

Various technologies have been developed for CO_2 separation and capture in industrial emissions, utilizing both chemical and physical processes. The choice of an appropriate method depends on process characteristics and flue gas composition (Rao & Rubin, 2002). The most widely studied techniques include absorption, adsorption, membrane separation, and cryogenic methods (Liu et al., 2023)

Absorption is the most established CO_2 capture method, employing liquid solvents such as amines or chilled ammonia. Despite its industrial maturity and high efficiency, this process has significant drawbacks, including high energy consumption, solvent degradation, and equipment corrosion. The energy required for solvent regeneration alone accounts for approximately 20–30% of the electricity generated in combustion processes (Song et al., 2018). Nonetheless, absorption remains the dominant post-combustion CO_2 capture technology (Darde et al., 2009).

Membrane separation relies on selective materials to separate CO_2 from other gases. This technique is attractive due to its continuous operation and low energy demand; however, its large-scale application is hindered by challenges related to membrane selectivity and permeability (Yuan, Eden, & Gani, 2015). Similarly, cryogenic separation involves cooling gas mixtures until CO_2 condenses. While capable of producing high-purity CO_2, this method is energy-intensive and is only cost-effective when an inexpensive cooling source is available (Song et al., 2018).The various technologies and materials used in carbon capture are summarized in Figure 1.

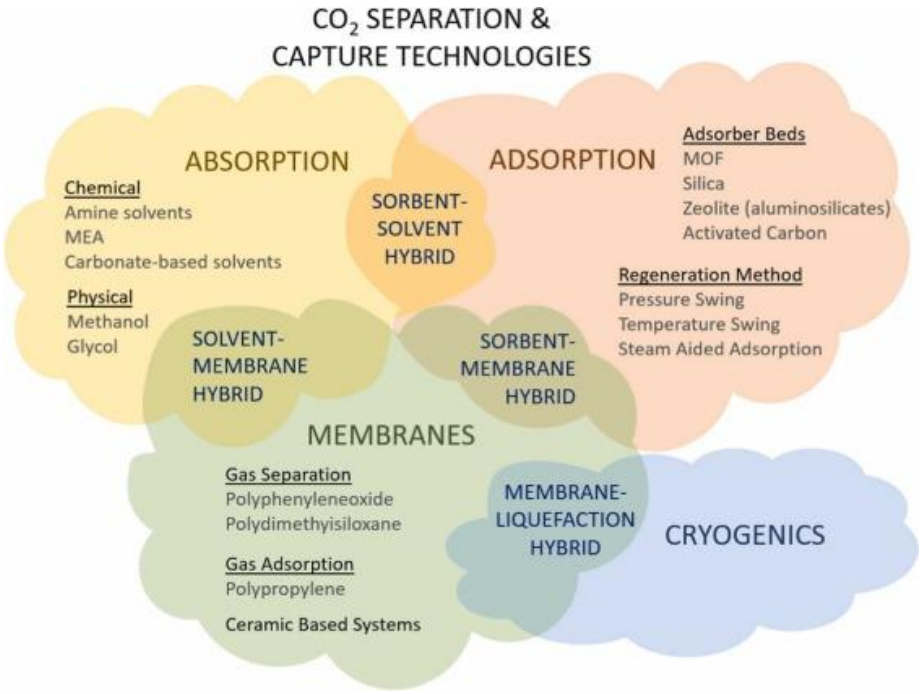

Figure 1. Technologies and materials used in carbon capture Source from (Rezaei et al., 2023).

Source from (Rezaei et al., 2023) with permission of Elsevier, copyright 2025.

Adsorption is emerging as a viable alternative to absorption. In this process, solid materials such as zeolites, metal-organic frameworks (MOFs), and activated carbon selectively adsorb CO_2 from gas mixtures (Figueroa et al., 2008; Park et al., 2015). Compared to liquid absorption, adsorption offers advantages including lower energy consumption, higher CO_2 selectivity at low pressures, and the reusability of adsorbents. The process typically operates in packed columns, where CO_2 binds to the adsorbent surface. On an industrial scale, adsorption runs in continuous cycles, alternating between capture and regeneration phases (Aaron & Tsouris, 2005; Song et al., 2019). The regeneration step can be achieved through pressure swing adsorption (PSA), vacuum swing adsorption (VSA), or temperature swing adsorption (TSA), depending on the process requirements (Yong, Mata, & Rodrigues, 2002).

Adsorption-based CO_2 capture is already applied in natural gas processing and chemical industries, and ongoing research aims to enhance its efficiency and cost-effectiveness (Berg et al., 2019). While absorption remains the predominant technology for post-combustion capture, adsorption is gaining traction due to its lower energy demands and potential for seamless

integration into existing industrial systems (Chen et al., 2011; Zhou et al., 2012; Khnifira et al., 2021).

1.2.1. CO_2 Capture by Adsorption

Among various separation and purification techniques, adsorption has gained significant attention due to its cost-effectiveness, simplicity, and environmental benefits. According to IUPAC, adsorption is defined as "the increase in the concentration of a substance at the interface of a condensed and a liquid or gaseous layer owing to the operation of surface forces" (Mozaffari Majd et al., 2021). In this process, the substance being adsorbed is called the adsorbate, while the material onto which it adheres is the adsorbent.

Adsorption can be classified as either physical (physisorption) or chemical (chemisorption). Physisorption is a general phenomenon occurring whenever an adsorptive is carried into contact with the surface of a solid (the adsorbent). The intermolecular forces involved are of the same type as those responsible for the imperfection of real gases and the condensation of vapors. In addition to the attractive dispersion forces and the short-range repulsive forces, specific molecular interactions generally occur because of the geometric and electronic properties of the adsorbent and adsorptive. In chemisorption, the intermolecular forces involved lead to the formation of chemical bonds (Thommes et al., 2015).

Adsorption is a physicochemical process where molecules from a fluid phase (liquid or gas) adhere to the surface of a solid adsorbent through intermolecular interactions (McCabe et al., 1993). In CO_2 capture, adsorption enables the selective removal of CO_2 from gas mixtures, driven by the affinity between the adsorbate (CO_2) and the adsorbent. Mass transfer during adsorption occurs in two steps: (1) gas molecules diffuse toward the adsorbent surface due to a concentration gradient, and (2) these molecules then diffuse into the internal pores of the solid, where they are retained at active sites with high adsorption potential (McCabe et al., 1993).

The efficiency of CO_2 capture by physisorption depends significantly on the adsorbent's textural and surface properties, including specific surface area, pore size distribution, pore volume, and surface polarity (Nanda et al., 2016). These characteristics directly influence the

adsorbent's selectivity for CO_2 over other gases commonly found in industrial streams, such as N_2, CO, and CH_4. While high surface area is important, it's crucial to understand that selectivity arises from a combination of factors, including preferential adsorption sites, pore size matching the CO_2 molecule, and specific interactions between the CO_2 quadrupole moment and the surface charge density of the adsorbent. Surface functional groups, even in physisorbents, can play a significant role in enhancing CO_2 selectivity.

Advanced porous materials like zeolites, metal-organic frameworks (MOFs), and activated carbons have significantly improved CO_2 adsorption performance (Neves & Schvartzman, 2005). These materials offer high surface areas, tunable pore structures (especially MOFs), and the potential for improved CO_2 selectivity. Activated carbons, for example, can be surface modified to enhance CO_2 capture. Pressure swing adsorption (PSA) and vacuum swing adsorption (VSA) are efficient cyclic processes for CO_2 capture, optimizing adsorbent regeneration (desorption of CO_2 by changing pressure or temperature) while maintaining energy efficiency (Neves & Schvartzman, 2005).

Typical flue gas from a coal-fired power plant contains a relatively low CO_2 concentration (14-16% vol.), with the majority being N_2 (73-78% vol.) and smaller amounts of H_2O (5-7% vol.), O_2 (3-4% vol.), CO, NOx, and SOx (ppm) (Bahamon & Vega, 2016). This low CO_2 partial pressure and complex gas mixture necessitate adsorbents with high CO_2 affinity for effective capture. Beyond selectivity, key adsorbent properties include high CO_2 adsorption capacity (mmol/g), fast adsorption/desorption kinetics (related to the sharpness of the breakthrough curve), facile regeneration (minimizing the energy required for desorption), and good thermal, mechanical, and chemical stability (Songolzadeh et al., 2012). While many materials have been explored (activated carbon fibers, silica gel, ion exchange resins, zeolites, porous silicates**,** activated alumina, metal oxides, MOFs, hybrid materials, etc.), practical applications require materials that are not only effective but also available in large quantities and at low cost.

An ideal CO_2 adsorbent should possess several key characteristics:

- High CO_2 adsorption capacity: The amount of CO_2 adsorbed at operating pressure and temperature (Ho et al., 2008; Samanta et al., 2011).

- High working capacity: The difference in adsorption capacity between operating and regeneration conditions, which influences equipment size and cost (Ho et al., 2008; Samanta et al., 2011). While adsorption capacity is important, working capacity also depends on operating conditions.
- Selective CO_2 adsorption: High selectivity for CO_2 over other gases like CH_4 and N_2 is crucial for product purity and cost reduction (Ho et al., 2008; Sayari et al., 2011).
- Fast adsorption/desorption kinetics: Rapid mass transfer is essential for efficient cycling and shorter cycle times (Samanta et al., 2011).
- Facile regeneration: The adsorbent should require minimal energy for CO_2 desorption, which is related to the enthalpy of adsorption. Physisorption enthalpies typically range from -25 to -50 kJ/mol (Samanta et al., 2011).
- High mechanical strength and thermal stability: The adsorbent must withstand operating pressures and temperatures without structural damage, ensuring a longer lifespan (Samanta et al., 2011).
- High chemical stability and impurity tolerance: The adsorbent should be resistant to degradation by water vapor and other impurities present in flue gas (Sayari et al., 2011).
- Low production costs: Cost-effectiveness is essential for large-scale industrial applications.

1.2.2. Adsorbent Materials

A wide range of materials has been investigated for use as solid adsorbents in gas separation systems. Key properties such as microporosity, chemical composition, surface area, thermal and chemical stability, and adsorption capacityare critical for efficient operation. These properties collectively influence a material's selectivity, regenerability, and overall performance, particularly in CO_2 capture applications.

To aid in material selection, Table 1 summarizes the key adsorbents reported in the literature, highlighting their characteristics and limitations.

Table 1. Key adsorbents highlighted in the literature, detailing their characteristics and limitations to aid in the selection process.

Materials	Characteristics	References
Activated Carbon (AC)	High degree of porosity, adjustable textural properties, high selectivity for CO_2 capture, high thermal stability, and efficient regeneration	(Vizcarra Valencia, 2007) (De Oliveira et al., 2021)
Zeolites	High thermal stability, large surface area, strong affinity for polar molecules, ion-exchange capacity, and resistance to spontaneous combustion in adsorption beds. Relatively low cost	(Kumar et al., 2020)
MOFs (Metal-Organic Frameworks)	" Highly designable crystalline porous solids with interesting potential, but with low resistance to humidity and low chemical and mechanical stability "	(Gutierrez-Ortega et al., 2022)
Sílicas	Require surface functionalization (e.g., amine grafting) for efficient CO_2 capture; however, they suffer from slow regeneration and long-term degradation, limiting their practical application	

Among the various adsorbent materials, zeolites stand out due to their well-defined crystalline structure, high adsorption capacity, and tunable selectivity, making them a preferred choice for CO_2 capture. Their unique properties allow for efficient separation and purification processes, making them widely used in industrial applications such as gas separation, catalysis, and environmental treatment.

1.2.2.1. Zeolites

Zeolites were first identified in 1756 by the Swedish mineralogist Baron Axel Fredrik Cronstedt, who coined the term *zeolite* from the Greek words *zeo* (to boil) and *lithos* (stone), referring to the material's ability to release water when heated. Their ion-exchange properties were later recognized in soil chemistry studies, and in 1925, Weigel and Steinhalf demonstrated their ability to selectively adsorb smaller molecules while rejecting larger ones. This molecular sieving effect was formally named by McBain in 1932 (Luz, 1995).

The industrial significance of zeolites grew in the mid-20th century, particularly after the synthesis of zeolites A, X, and Y in 1948. These synthetic materials provided precise control over pore size and chemical composition, enabling their use in catalysis, adsorption, ion exchange, and selective separation (Figueiredo & Ribeiro, 1987). By 1962, synthetic faujasites (zeolites X and Y) revolutionized the petroleum industry as catalysts for fluid catalytic cracking, improving efficiency and product purity (Luna & Schuchardt, 2001). Subsequent advances allowed the incorporation of metals such as iron, gallium, and titanium into zeolitic frameworks, broadening their catalytic applications and reducing costs in petrochemical processes.

Since the 1990s, research has expanded into tailored synthetic zeolites, leading to novel applications in environmental remediation, gas separation, and water treatment (Hölderich et al., 1994; Meynen et al., 2009). The International Zeolite Association (IZA) currently recognizes more than 67 natural zeolites and 256 synthetic framework types, highlighting the extensive variety of structures available for different applications.

Zeolites are crystalline aluminosilicates belonging to the tectosilicate family, composed of a three-dimensional framework of SiO_4 and AlO_4 tetrahedra connected by oxygen atoms (Ferreira Falcão, 2005). creates uniformly sized pores and cavities that accommodate cations, water molecules, and adsorbates. The porosity of zeolites allows them to function as molecular sieves, selectively adsorbing gases and ions based on size and polarity (Braga & Morgon, 2007).

Zeolites can be classified as natural or synthetic. Natural zeolites form over thousands to millions of years through volcanic and sedimentary processes, often containing impurities that limit their industrial use (Souza Pinto et al., 2018). In contrast, synthetic zeolites are produced

under controlled conditions, offering tailored pore structures, thermal stability, and optimized adsorption properties. Their synthesis frequently utilizes industrial byproducts from organic and inorganic ash through hydrothermal or microwave-assisted methods.

Zeolites exhibit key properties that make them valuable for gas separation and adsorption-based processes, including:

- High porosity: Their well-defined microporous structure provides a large surface area for gas adsorption.
- Cation exchange capacity: The presence of exchangeable cations influences the affinity for polar and nonpolar gases.
- Selective adsorption: Zeolites can separate molecules based on size, shape, and polarity, making them effective for gas purification.
- Thermal and chemical stability: Zeolites remain stable under industrial operating conditions (MAT, 2023).

The composition of a zeolite can be described by three fundamental components: its crystalline framework, compensating cations, and the adsorbed phase (Auerbach et al., 2003). This relationship is expressed by the general formula:

$$M(nx)\cdot[(AlO_2)x(SiO_2)y]\cdot wH_2O$$

where M is the compensating cation of valence n, w is the number of water molecules, and x + y represents the total number of SiO_4 and AlO_4 tetrahedra in the unit cell. The substitution of Si^{4+} by Al^{3+} introduces a negative charge, which is balanced by exchangeable cations such as Na^+, K^+, Ca^{2+}, and Mg^{2+}. The substitution of Si^{4+} by Al^{3+} introduces a negative charge, which is balanced by cations. These cations influence adsorption selectivity and capacity for different gases.

Zeolites have a strong affinity for water due to their charge-balancing cations, which form strong interactions with water molecules. While silicon atoms in the framework remain electrically neutral, aluminum atoms introduce negative charges that require stabilization by positive exchangeable cations. These cations, located at specific sites in the framework, play a crucial role in defining adsorption properties (Al Ezzi & Ma, 2017).

Zeolites are classified based on here structure characteristics. One of the most recognized classification systems is that of the International Union of Pure and Applied Chemistry (IUPAC),

which considers only the structure, regardless of chemical composition. In this system, the structures are identified by a three-letter code, as established by the International Zeolite Association (IZA).

Zeolites are crystalline, microporous materials with large surface areas and molecular size pore structure. zeolites such as type X and type A are widely used for CO_2 removal from natural gas streams due to their high adsorption capacity and selectivity (Chen et al., 2016). Among these, zeolites LTA and FAU have gained particular attention due to their well-defined pore structures and tunable adsorption properties, making them highly effective in gas separation and purification processes.

1.2.2.2. Zeolite LTA (Linde Type A)

Zeolite LTA, commonly referred to as Zeolite A, is a crystalline aluminosilicate with a well-defined porous structure. The most widely used variants, 4A and 3A, are distinguished by their effective pore sizes of approximately 4 Å and 3 Å, respectively. These pore dimensions directly correspond to the presence of cations that influence adsorption behaviour.

Structurally, LTA consists of two primary cage types: α-cage (supercage): Internal diameter of ~11.4 Å, accessible through octagonal windows (8 oxygen atoms) with entry sizes of ~4 Å (4A) or 3 Å (3A).β-cage (sodalite cage): Free diameter of 6.6 Å, connected by hexagonal windows (6 oxygen atoms) with apertures of ~2.2 Å (Al Ezzi & Ma, 2017).

The cation distribution within the framework plays a key role in adsorption selectivity. Sodium ions (Na^+) in Na-LTA can be replaced by other cations such as Li^+ (Li-LTA), K^+ (K-LTA), or Ca^{2+} (Ca-LTA), modifying ion-exchange and adsorption properties. The cubic framework of LTA is built from sodalite cages linked by four-membered rings, forming a highly accessible pore system, making it effective for gas separation and drying applications (Julbe & Drobek, 2016).

1.2.2.3. Zeolite FAU (Faujasite-Type Zeolite)

The FAU-type zeolites, including Zeolite X and Zeolite Y, are synthetic crystalline aluminosilicates with a three-dimensional porous structure. Like LTA, FAU consists of interconnected α- and β-cages but with larger pore dimensions.

The α-cage (supercage) in FAU has a free diameter of approximately 12 Å and is accessible through four dodecagonal (12-ring) windows, each composed of 12 oxygen atoms, with an effective pore size of 7.4–8 Å, depending on the cations present. β-cage (sodalite cage): Free diameter of 6.6 Å, connected by hexagonal (6-ring) windows (double 6 rings) with openings of ~2.2 Å.

A key distinction between Zeolite X (high aluminum content) and Zeolite Y (higher silica content) is the Si/Al ratio and the number of exchangeable cations. The number of cations per cage varies from 10–12 in high-alumina Zeolite X to as low as 6 in high-silica Zeolite Y. These cations occupy specific sites within the framework, influencing the adsorption properties.

These cations occupy specific framework sites, influencing adsorption properties. The five primary cation sites in FAU are: Site I: Center of the double 6 rings. Site I': Inside the β-cage, near a hexagonal ring shared with a double 6 ring. Site II: Inside the α-cage, near an unshared hexagonal face of a β-cage. Site II': Inside the β-cage, adjacent to an unshared hexagonal face. Site III: Near the center of the 12-ring aperture between adjacent α-cages (Al Ezzi & Ma, 2017).

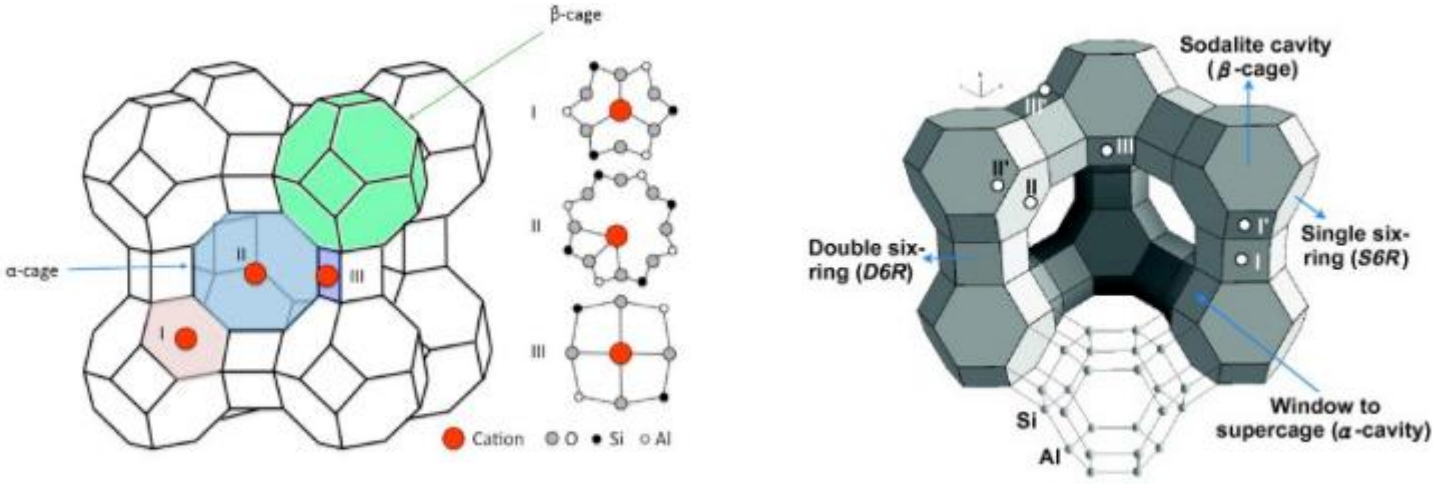

Figure 2. Zeolite LTA (right) and FAU (left) framework structures. Source from (Al Ezzi & Ma, 2017).

The unit cell of FAU zeolites measures approximately 25 Å and consists of 192 tetrahedra of SiO_4 and AlO_4, linked by oxygen atoms. This structure is highly stable and has the largest spatial volume among known zeolites, enhancing their gas adsorption capacity (Powroznik & Castillo Alonso, 2018).

1.2.2.4. Structural Characteristics and Pore

In the framework, Al or Si atoms occupy the center of the tetrahedra, while oxygen atoms are positioned at the vertices. When Si^{4+} is replaced by Al^{3+}, the framework acquires a negative charge, which must be balanced by compensating cations—typically alkali or alkaline earth metals (Luz, 1995).

The Si/Al ratio in zeolites can range from 1 to ∞, but Si/Al < 1 is not feasible because having two adjacent aluminum tetrahedra would lead to electrostatic repulsion, preventing the formation of such structures (Auerbach et al., 2003).

Based on their silica-to-aluminum ratio, zeolites are categorized into different groups, as shown in Table 2.

Table 2. Zeolite Classification Based on Si/Al Ratio. Source from (Auerbach et al., 2003)

Silica Content	Si/Al Ratio	Example
Low silica	1 a 1.5	A and X (natural and synthetic)
Intermediate silica	~2 a 8	Synthetic Y, natural mordenite
High silica	~10 a < ∞	Synthetic ZSM-5

The micropores of zeolites are classified by size into four categories: small pores (<4 Å), medium (4–6 Å), large (6–8 Å), and extra-large (>8 Å). Pores larger than 20 Å are classified as mesoporous (Luna & Schuchardt, 2001).

Table 3. Characteristics of Some Molecular Sieves. (Sources: Luna & Schuchardt, 2000; Rouquerol et al., 2014)

Pore Size	No.of Tetrahedra	Pore Diameter (Å)	Common Name	Structural Symbol
Small	8	4.1	Zeolite A	LTA
Medium	10	5.3 - 5.6	TS-1, ZSM-5	MFI
		3.9 - 6.3	AlPO-11	AEL
		5.5 - 6.2	ZSM-12	MTW
Large	12	7.3	AlPO-5	AFI
		7.4	Zeolite X, Y	FAU
		6 - 7	Zeolite β	BEA
Extra-large	>12	7.9 - 8.7	AlPO-8	AET
		12.1	VPI-5	VFI
		13.2 - 4.0	Cloverita	CLO
Mesoporous	14 or more	15-100	MCM-41	

The zeolites listed in Table 3 are widely used in ion exchange, catalysis, and selective adsorption due to their unique structural features, such as high hydration capacity, low density when dehydrated, stable crystalline frameworks, and uniform pore channels, which enable effective molecular sieving (Harben & Kužvart, 1997).

1.2.2.5. Zeolite 13X for CO_2 Separation and Gas Purification

Faujasite-type zeolites (FAU), whether synthetic or natural, exhibit superior performance in gas separation processes due to their high porosity, numerous active sites, and low diffusional restrictions. A defining feature of faujasite zeolites is their low Si/Al molar ratio, which results in a high density of negative charges, enhancing interactions with adsorbed molecules (Gonçalves et al., 2020).

The historical evolution of zeolite research, particularly for zeolite X and zeolite A, underscores their growing importance in gas separation and CO_2 capture applications. As illustrated in Figure 3, these materials have been progressively optimized over the decades for industrial use.

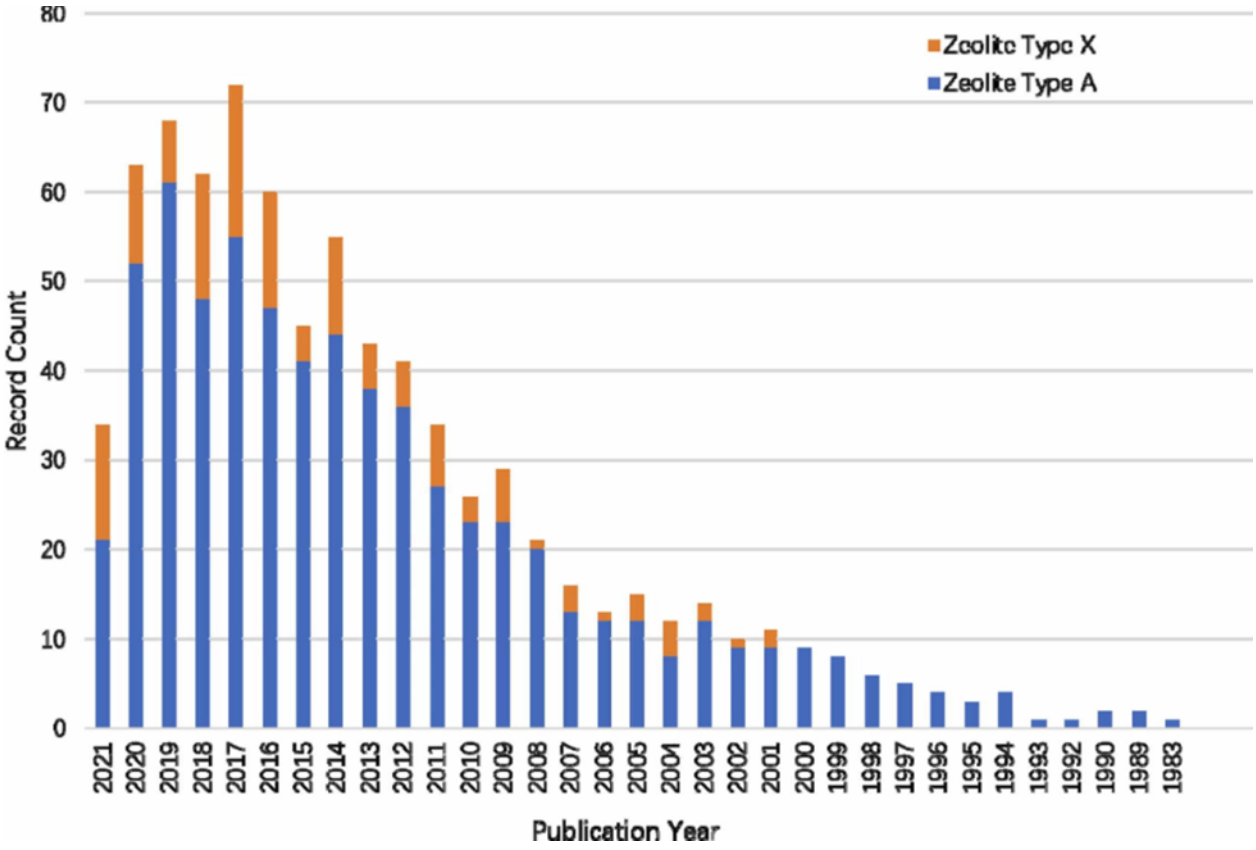

Figure 3. Historical evolution of zeolite X and zeolite A research, highlighting their key applications in gas separation and CO_2 capture over the decades. Source from (Gao et al., 2023).

Among FAU-type zeolites, zeolite 13X stands out as one of the most effective materials for CO_2 separation. It has been widely used in natural gas upgrading, post-combustion CO_2 capture, and pressure swing adsorption (PSA) processes due to its high adsorption capacity, mechanical

and thermal stability, and large-scale availability (Bahamon & Vega, 2016; Harlick & Tezel, 2004; Streb & Mazzotti, 2021).

Zeolite 13X demonstrates exceptional selectivity for CO_2 due to the strong electrostatic interactions between CO_2 and charge-balancing cations within its framework (Samanta et al., 2011). The preferential adsorption of CO_2 over other gases makes it ideal for applications such as:

- Methane purification from natural gas
- Carbon capture from flue gases
- Gas separation via pressure swing adsorption (PSA)

Studies have shown that CO_2 diffusion in zeolite 13X plays a crucial role in determining the adsorption efficiency (Jedli et al., 2024). Furthermore, experimental and modeling research confirms its high adsorption capacity, stability under high temperatures, and regenerability, making it a reliable adsorbent for continuous operation (Hedlund et al., 2021; Aleksandrzak et al., 2024).

In PSA systems, zeolite 13X has been widely investigated for CO_2 separation at relatively low pressures, demonstrating promising results in fluidized bed adsorption and cyclic operation for long-term CO_2 capture (Girimonte et al., 2019).

Overall, due to its exceptional adsorption properties, stability, and reusability, zeolite 13X remains one of the most widely utilized adsorbents for CO_2 capture and gas purification (Cavenati et al., 2004).

Zeolites can be classified into various natural and synthetic types, and they are commonly used in different forms, such as powders, pellets, or beads, depending on the application.

1.2.2.6. Synthetic Zeolites

The first synthetic zeolites were produced in the 1940s by Barrer and Milton, who introduced a method based on the alkaline treatment of aluminum- and silicon-containing materials in an aqueous medium (Gao et al., 2023). Today, synthetic zeolites are widely used in gas separation, catalysis, and adsorption due to their well-defined crystalline structures and high surface areas.

Recent advancements have focused on synthesizing fine zeolite powders, including nano-sized materials, which offer advantages over conventional micron-sized zeolites. Smaller particle sizes increase external surface area, reduce diffusion limitations, and enhance adsorption efficiency (Charkhi et al., 2012).

Zeolite powders can be produced through direct synthesis from highly pure precursor gels or by converting natural minerals into zeolitic materials. Common synthetic zeolites, such as A, X, and NaY, are typically synthesized by preparing a homogeneous aluminosilicate gel, followed by controlled crystallization at around 120°C. The resulting material is then filtered, washed to maintain a pH between 9 and 12, and dried using spray drying or heat treatment to ensure structural stability (Gleichmann et al., 2016).

Although powdered zeolites are widely studied for CO_2 adsorption due to their high surface area, they present challenges for large-scale industrial applications. One of the main drawbacks is the high pressure drop they cause in adsorption columns, particularly in pressure swing adsorption (PSA) processes. Fine powders can also lead to fluidization and bed instability during gas flow, reducing adsorption efficiency and making handling more difficult.

For these reasons, structured adsorbents—such as pellets, beads, or monoliths—are preferred in industrial applications. These forms improve gas flow distribution, prevent bed movement, and simplify handling during adsorption, regeneration, and replacement cycles. Additionally, structured zeolites enhance process efficiency by reducing pressure losses and maintaining system stability (Orsikowsky-Sanchez et al., 2021; Park et al., 2016).

1.2.2.6.1. Binder Free Zeolites

Although powdered adsorbents are widely used in laboratory-scale adsorption studies, their direct application in industrial processes presents challenges. To overcome these limitations, zeolite-based adsorbents must be shaped into structured forms such as granules, spheres, rings, tablets, honeycombs, or interlocked structures. These larger solid bodies help optimize gas flow, minimize pressure drops, and improve mechanical stability, making them more suitable for large-scale adsorption and catalysis applications (David, 2015; Mondragon et al., 1990).

In the past two decades, research on binder-free zeolites, particularly zeolites A and X, has gained attention due to their superior adsorption capacity and mechanical strength compared to binder-containing zeolites. The absence of inactive binder components maximizes available adsorption sites (and therefore adsorption capacity), enhances mass transfer efficiency, and improves overall adsorption performance. These advantages make binder-free zeolites a promising alternative for CO_2 capture and gas purification processes (Pavlov et al., 2012; Schumann et al., 2011).

To produce structured zeolites, conventional shaping techniques involve mixing powdered zeolites with 1–50 wt.% of inorganic binders (e.g., bentonite, kaolinite) and fillers (e.g., starch, carboxymethyl cellulose) before forming the material through spray drying, extrusion, or pressing (Charkhi et al., 2012). However, binders can reduce adsorption efficiency by blocking micropores, decreasing surface area, and lowering pore volume. Studies have shown that adding 20 wt.% of binders to pristine zeolites can reduce adsorption capacity by up to 20% (Silva et al., 2012), see figure 4. This reduction can significantly impact the performance of adsorbents in selective CO_2 capture applications, as demonstrated in studies evaluating binder effects on CO_2, CH_4, and N_2 adsorption on zeolite 13X (Najafi et al., 2023).

To address these challenges, binder-free zeolite synthesis has emerged as a viable solution, eliminating the need for inert binders while maintaining mechanical stability. This process typically involves mixing zeolite powder with metakaolin and sodium-silicon compounds, followed by granulation or extrusion. The material then undergoes aging, reaction treatments to remove temporary binders, and final washing, drying, and activation steps (Gleichmann et al., 2016).

An important advancement in sustainable zeolite production is the use of environmentally friendly raw materials. Synthetic zeolites can now be produced from ecological and industrial waste sources such as rice husk ash, coal fly ash, oil shale ash, bagasse fly ash, high-silicon fly ash, paper sludge, waste porcelain, and kaolinite. These alternative raw materials offer a cost-effective and sustainable approach to zeolite synthesis while reducing industrial waste disposal issues (Abdullahi et al., 2017).

Among these materials, kaolinite has gained particular interest for its role in binder-free zeolite production. The transformation of kaolinite into zeolite involves two key steps:

Metakaolinization Conversion of kaolin clay into metakaolin through chemical activation. And zeolitization Treatment of metakaolin with an aqueous alkali solution to form zeolite structures.

The influence of binders on adsorption efficiency is further illustrated in **Figure 4**, where a significant decrease in static adsorption capacity is observed for binder-containing NaMsX zeolites. This reduction is attributed to micropore obstruction and diminished pore volume caused by inert binder components (Schumann et al., 2011).

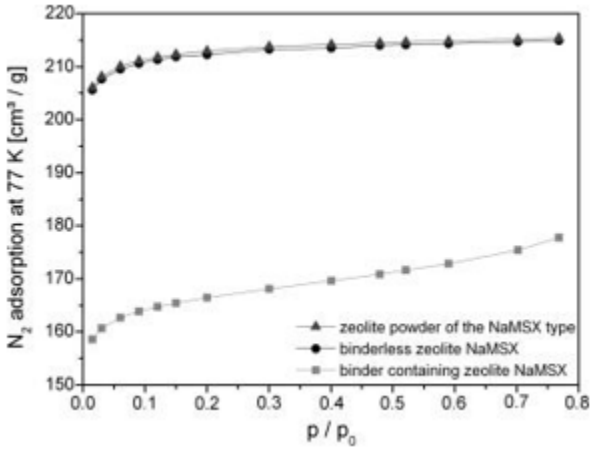

Figure 4. Comparison of the static adsorption capacity of NaMsX zeolite powder with and without a binder. Source from (Schumann et al., 2011) with permission of Elsevier, copyright 2025.

1.3. Adsorption Isotherm Modeling

Adsorption isotherms are essential tools for understanding adsorption processes, as they describe how the amount of adsorbed material changes with pressure (or concentration) at a constant temperature. These models provide valuable insights into adsorption capacity, surface properties, and the mechanisms governing gas-solid interactions (Mozaffari Majd et al., 2021).

Adsorption isotherm models fall into two main categories: empirical and theoretical. Empirical models are derived from experimental data and effectively fit adsorption behavior, even

if they do not fully explain molecular interactions. Theoretical models, on the other hand, are based on physical and chemical principles, offering a deeper understanding of adsorption mechanisms (Henrique, 2015).

Porous materials like zeolites are commonly analyzed using mathematical models that fit experimentally measured adsorption isotherms. These isotherms, obtained from single-component gas adsorption experiments, help determine porous properties and adsorption capacity. Various analytical techniques can be used to explore CO_2 adsorption mechanisms in zeolite structures, providing essential information on gas uptake and interaction with the adsorbent (Tao et al., 2024).

The quantity of adsorbed gas (q) in equilibrium conditions can be expressed as a function of temperature (T) and pressure (P). Adsorption generally occurs through two primary mechanisms: chemisorption, which involves strong chemical bonding and forms a monolayer, and physisorption, which relies on weaker van der Waals interactions and can lead to multilayer adsorption (Al Ezzi & Ma, 2017). Adsorption isotherms are also useful for evaluating adsorption affinity and capacity. Their equations are often rearranged into linear forms for easier analysis, and if the experimental data align with a straight-line equation, it indicates that the selected model accurately represents the adsorption process (Tazikeh et al., 2022).

One of the most widely used adsorption models is the Langmuir isotherm, introduced by Irving Langmuir in 1918. This model assumes that adsorption occurs on a uniform surface with a fixed number of identical sites, with each site accommodating only one adsorbate molecule. It also assumes that adsorption reaches equilibrium when the rate of adsorption equals the rate of desorption. Despite its simplicity, the Langmuir model effectively describes monolayer adsorption on homogeneous surfaces (Do, 1998).

For more complex adsorption systems, the Dual-Site Langmuir model extends the Langmuir isotherm by considering adsorption on two distinct types of sites. This approach is particularly useful for materials with heterogeneous surfaces, where adsorption sites exhibit different affinities for the adsorbate. By accounting for these variations, the Dual-Site Langmuir model provides a more precise representation of adsorption behavior (Ruthven, 1984).

In this study, both the Langmuir and Dual-Site Langmuir models were applied to analyze adsorption isotherms. These models help in understanding the adsorption characteristics of the studied materials, particularly in the context of CO_2 capture and separation processes.

1.3.1. Langmuir Model

The Langmuir adsorption isotherm, originally proposed in 1918, describes the adsorption of gas molecules onto a solid surface (Langmuir, 1918). This model assumes that adsorption occurs in a monolayer, meaning that only a single layer of molecules can form on the surface. Each adsorption site is considered identical and independent, with no interactions between adsorbed molecules, even at adjacent sites (Foo & Hameed, 2010). Additionally, the model assumes that all adsorption sites have the same energy and that once a molecule occupies a site, no further adsorption can occur at that location (Ye et al., 2021).

The model is based on the following assumptions:

1. Molecules are adsorbed at discrete active sites on the surface.
2. Each active site adsorbs only one molecule.
3. The adsorbing surface is generally uniform.
4. There is no interaction between the adsorbed molecules (Ye et al., 2021).

Due to its simplicity and accuracy, the Langmuir equation is widely used to describe adsorption equilibrium for single-component systems across various adsorbents (Foo & Hameed, 2010). It is applicable over a range of pressures and provides insights into how adsorption capacity changes as a function of partial pressure or concentration at a constant temperature.

For a single-component adsorption system, the Langmuir equation can be represented by the following equation:

$$q = q_M \frac{bp}{1-bp} \quad (1)$$

where q ($mol.kg^{-1}$) represents the adsorbed concentration at equilibrium conditions, q_M ($mol.kg^{-1}$) denotes the maximum saturation capacity, p (kPa) is the pressure of adsorbate species, and b (kPa^{-1}) is the adsorption affinity constant, which reflects the strength of attraction between the adsorbate molecule and the adsorbent surface.

The effect of temperature on the adsorption affinity constant b, is taken into account by the integrated Van't Hoff equation:

$$b = b_\infty e^{\left(\frac{-\Delta H}{RT}\right)} \quad (2)$$

where b_∞ (kPa^{-1}) represents the pre-exponential factor of the affinity constant at infinite temperature, R (J.mol^{-1}.K^{-1}) is the ideal gas constant, $-\Delta H$ (J.mol^{-1}) denotes the heat of adsorption, and T (K) is the temperature.

Since adsorption is an exothermic process, the value of b decreases as temperature increases since ΔH is negative. This reflects the tendency of adsorption to become less favorable at higher temperatures.

1.3.2. Dual-site Langmuir Model

The Dual-Site Langmuir (DSL) model is an extension of the classical Langmuir isotherm, designed to describe adsorption on heterogeneous surfaces. It is particularly useful for pressure swing adsorption (PSA) processes, where gas separation and purification rely on selective adsorption (Wang et al., 2020). Unlike the traditional Langmuir model, which assumes a single type of adsorption site, the DSL model considers two distinct adsorption sites, each with its own binding energy and adsorption capacity (Foo & Hameed, 2010).

In the DSL model, the adsorbate molecules distribute themselves between two different types of adsorption sites, both following the fundamental principles of the Langmuir isotherm but exhibiting different adsorption capacities and affinities. The equilibrium equation for single-component adsorption is given by:

$$q = \left(q_{m1}\frac{b_1 p}{1+b_1 p}\right)_{site1} + \left(q_{m2}\frac{b_2 p}{1+b_2 p}\right)_{site\,2} \quad (3)$$

Where q_{m1} and q_{m2} are the maximum adsorption capacities at sites 1 and 2, respectively; b_1 and b_2 are the adsorption affinity constants at each site; p (kPa) is the partial pressure of the adsorbate.

The presence of two distinct adsorption sites accounts for surface heterogeneity and variations in adsorption energy. If only one site is considered, the DSL model simplifies to the standard Langmuir equation (Equation 1).

The extended DSL model isotherm to multicomponent systems (component i and j) is given by the following equation:

$$q_i = q_{m1,i} \frac{b_{1,i} p_i}{1+\sum_{j=1}^{n} b_{1j} p_j} + q_{m2,i} \frac{b_{2,i} p_i}{1+\sum_{j=1}^{n} b_{2j} p_j} \quad (4)$$

Where $q_{m1,i}$,i and $q_{m2,i}$ are the maximum adsorption capacities of component i at sites 1 and 2 per unit mass of adsorbent; $b_{1,i}$ and $b_{2,i}$ are the affinity parameters between the adsorbent and adsorbate at sites 1 and 2,;b_i and b_j is the partial pressure of component i and j.

This model effectively captures competitive adsorption behavior, making it a valuable tool for studying gas separation in industrial PSA applications. The DSL model provides a more detailed representation of adsorption in heterogeneous systems, where different sites contribute uniquely to the overall adsorption capacity.

1.3.3. Adsorption Selectivity

Adsorption selectivity, often expressed as α or separation factor, measures how effectively an adsorbent can distinguish and retain one gas species over another in a mixture. This thermodynamic parameter is essential for assessing the efficiency of materials used in gas separation processes. The selectivity of component *i* over *j* is typically calculated as:

$$\alpha_{i/j} = \frac{(q_i/q_j)}{(p_i/p_j)} \quad (5)$$

where q_i and q_j are the equilibrium adsorption capacities of each component, and p_i and p_j represent their respective partial pressures under the same temperature (Aly et al., 2024).

1.3.4. Working Capacity

The working capacity, commonly symbolized as β, refers to the usable amount of gas that an adsorbent can retain and release under specified operational conditions. This parameter is particularly important in cyclic adsorption processes like Pressure Swing Adsorption (PSA) or Temperature Swing Adsorption (TSA), where adsorption and desorption alternate in successive cycles. It is mathematically defined as:

$$\beta = q(T_1, P_1) - q(T_2, P_2) \tag{6}$$

Here, $q(T_1, P_1)$ denotes the gas uptake during the adsorption phase (at higher pressure or lower temperature), and $q(T_2, P_2)$ represents the amount remaining after the desorption step (at lower pressure or higher temperature) (Aly et al., 2024).

1.3.5. Fixed Bed Column Adsorption

Fixed-bed adsorption is a widely used method for gas and liquid purification, particularly in large-scale industrial applications where continuous operation and efficient separation are required. This process involves the passage of a fluid stream through a packed bed of adsorbent, enabling selective removal of target components. Due to its ability to handle significant volumes with high separation efficiency, fixed-bed adsorption is extensively applied in gas separation, CO_2 capture, and air purification.

Fixed-bed adsorption systems consist of a column packed with an adsorbent material through which the fluid flows, allowing the selective removal of target components. In industrial applications, adsorption in fixed-bed columns is often performed using two parallel columns, enabling continuous operation by alternating between adsorption and regeneration phases through a purge stream applied to the saturated column (Seader & Henley, 2001).

The performance of a fixed-bed adsorption system is governed by kinetic and thermodynamic factors. The breakthrough curve, a fundamental tool for analyzing adsorption dynamics, represents the progression of the mass transfer zone (MTZ) through the column over time. This curve provides insights into the saturation profile of the adsorbent, from the initial contact between the adsorbate and the adsorbent surface to the point where the column reaches saturation (Nascimento et al., 2014; Ferreira Melo, 2017).

A schematic representation of the fixed-bed adsorption process (Figure 5) illustrates how the adsorbate (gas) with an initial concentration C_o interacts with the adsorbent. Initially, the outlet concentration is zero, but as adsorption sites become saturated, the outlet concentration gradually increases. The breakthrough point occurs when the relative concentration C/C_o reaches 0.05, while full saturation is reached at $C/C_o = 1$ (Saraiva et al., 2024). The MTZ, where the most intense adsorption occurs, is influenced by temperature, flow rate, adsorption kinetics, and mass transfer resistance.

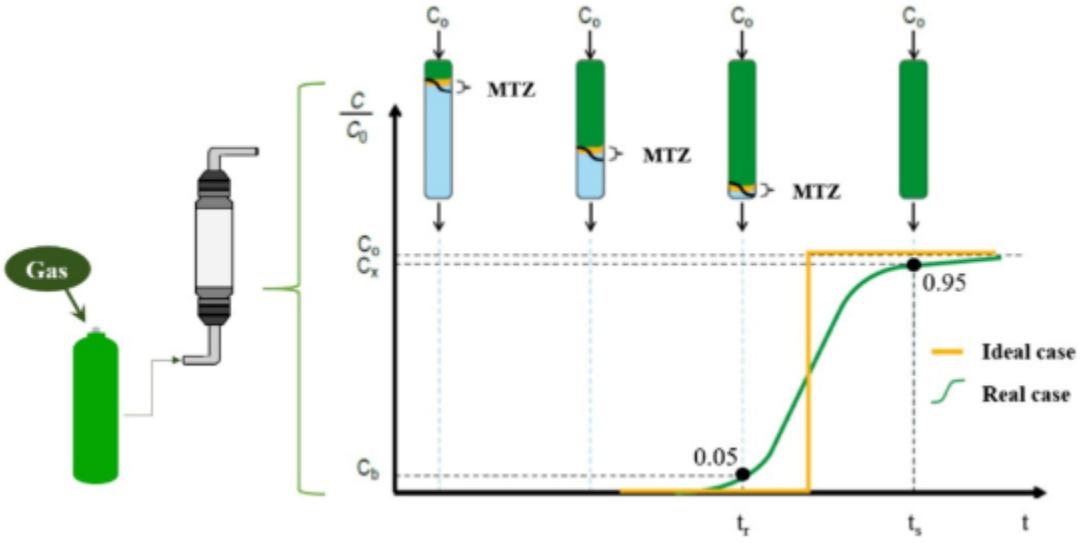

Figure 5. Schematic representation of the adsorption process in a fixed bed.

Source from (Saraiva et al., 2024).

The shape and position of the breakthrough curve provide valuable information about the adsorption mechanism. A sharp breakthrough curve suggests fast adsorption kinetics and strong

adsorbate-adsorbent interactions, while a more gradual curve indicates significant mass transfer limitations. Understanding these dynamics is crucial for optimizing column operation and ensuring efficient separation performance.

1.3.6. Pressure Swing Adsorption (PSA) Separation Processes

Pressure Swing Adsorption (PSA) is a widely used gas separation and purification technology that exploits the differences in adsorption affinities of gas molecules under varying pressure conditions. Since its commercial introduction in the 1960s by Skarstrom (Mosca, 2009), PSA has been extensively applied in industrial processes such as hydrogen purification, air separation, methane purification, and gas drying. The process operates in cyclic stages, with adsorption occurring at high pressure and desorption at low pressure, utilizing solid adsorbents such as zeolites, activated carbon, and molecular sieves (Subraveti et al., 2019).

PSA technology plays a crucial role in CO_2 capture, particularly in post-combustion and pre-combustion applications, as well as in biogas upgrading and flue gas treatment. Most PSA-based CO_2 separations rely on equilibrium-driven adsorption, where different gases interact with the adsorbent based on variations in binding forces (Subraveti et al., 2019). The adsorption performance depends strongly on pressure, as higher pressures typically lead to greater gas uptake. However, process efficiency is also influenced by the choice of adsorbent, given that different gases exhibit distinct affinities for various solid surfaces.

Zeolites are among the most extensively studied adsorbents for CO_2 capture in PSA processes. Zeolites X, Y, A, CHA, and ZK-5 are known for their high CO_2 adsorption capacity, though their CO_2/CH_4 selectivity varies (Liang et al., 2021). Research has confirmed the efficiency of both synthetic and natural zeolites in biogas purification and upgrading (Kadam & Panwar, 2017). In particular, zeolite 13X has been widely investigated for PSA applications. Dantas et al. (2011) developed a PSA model for CO_2/N_2 separation, demonstrating its effectiveness. Aleksandrzak et al. (2024) optimized PSA operational parameters such as pressure and temperature to enhance performance with zeolite 13X. Chue et al. (1995) reported that zeolite 13X achieved high CO_2 purity (>99%) and recovery rates of 53% for low CO_2 concentrations and 70% for high

concentrations, outperforming activated carbon. Additionally, Henrotin et al. (2024) highlighted that zeolite 13X can be efficiently regenerated, contributing to process sustainability. Fauziah et al. (2024) further confirmed that increasing pressure enhances gas separation efficiency in PSA processes using zeolite LiX.

A variant of PSA, known as Vacuum Swing Adsorption (VSA), desorbs gases under vacuum instead of reducing pressure to ambient levels. This approach is particularly advantageous when high recovery of the preferentially adsorbed species is required. Both PSA and VSA are suitable for bulk separations due to their rapid cycle times, which typically range from seconds to minutes (Subraveti et al., 2019). The selectivity of PSA systems arises from either equilibrium interactions (where gases exhibit different adsorption affinities) or kinetic effects (where adsorption rates vary among gas species).

Proper selection of adsorbent materials and process optimization are crucial for achieving high selectivity, adsorption capacity, and efficiency while minimizing breakthrough of undesired gases (Mosca, 2009). Overall, PSA technology remains a key method for industrial gas separation and CO_2 capture, with zeolite 13X standing out due to its high adsorption performance, regenerability, and process efficiency. Continued research and technological advancements are essential for further improving PSA-based gas separation processes.

Chapter 2
Material and Methods

2. Experimental Techniques for Gas Adsorption Studies

In gas adsorption research, two fundamental parameters are typically evaluated for the development of an adsorption process: adsorption equilibrium capacity and kinetics of sorption. Adsorption capacity quantifies the amount of gas retained per unit mass of adsorbent, while the kinetics characterizes the rate at which gas molecules penetrate the porous structure of the adsorbent. These parameters are essential for assessing material performance and optimizing adsorption-based separation processes.

To determine these properties, experimental techniques analyze the system's response to variations in operating conditions. The obtained adsorption capacities and kinetic values aid in predicting selectivity and guiding the selection and design of adsorption systems. Among the widely employed techniques for gas adsorption measurements are volumetric, gravimetric, and gas chromatographic methods, each offering specific advantages depending on the nature of the study.

- **Volumetric Method for Gas Adsorption Measurements**

The volumetric method is a widely used technique for determining adsorption capacity and diffusivity in porous materials. This approach involves the controlled expansion of gas from a reference cell into an evacuated adsorption cell containing a pre-treated adsorbent under isothermal conditions. By precisely measuring pressure changes and applying the real gas equation of state, it is possible to determine the quantity of gas adsorbed at equilibrium through a mass balance analysis of the gas phase before and after adsorption (Wang et al., 2019).

This method is extensively applied for obtaining adsorption isotherms and assessing diffusional properties, as it can be integrated with complementary techniques. However, the process requires highly sensitive pressure measurement equipment and may involve prolonged equilibrium times, especially for materials with slow diffusion rates (Heule et al., 2022).

Gas expansion behavior within the volumetric system is influenced by temperature, pressure differentials, and gas properties, making precise control and calibration essential. The use of differential pressure systems and advanced volume measurement techniques has improved the accuracy and efficiency of volumetric adsorption studies, further enhancing their applicability in industrial and research settings (Avdiaj et al., 2015).

- **Gravimetric Method**

The gravimetric method determines gas adsorption by measuring the weight change of an adsorbent exposed to a pure gas at constant temperature and pressure. A high-precision microbalance records mass variations as adsorption occurs, providing a direct measurement of the adsorbed amount (Wang et al., 2020).

This method is highly accurate and allows for the evaluation of adsorption kinetics and diffusivity by tracking weight changes over time. However, it requires sensitive equipment, as external factors such as vibrations and buoyancy effects can impact measurements (Yang, 2013). Despite these challenges, the gravimetric method remains a reliable tool for studying adsorption equilibrium and kinetics in various systems.

The two equilibrium methods are therefore favored for systems with relatively slow diffusion and moderate conditions (temperature and pressure).

- **Flow Gas chromatography method**

Flow gas chromatography (GC) is a widely used analytical technique in various fields, including petrochemicals, gas industry, environmental monitoring, and scientific research. It provides an alternative to conventional gravimetric and volumetric methods for determining adsorption equilibrium isotherms. The flow gas chromatographic process works by injecting an adsorbable gas component into a carrier gas stream, typically an inert gas like helium and directed to a fixed bed column containing the adsorbent allowing to measure a breakthrough curve that contains information about the adsorption equilibrium and kinetics (Yadav et al., 2018).

To determine adsorption equilibrium isotherms, a mixed carrier gas containing the adsorbable component (CO_2) and a non-adsorbable carrier gas (helium) in known proportions is introduced into the system. The retention time of small pulses of CO_2 is measured at different carrier compositions. Two primary methods can be used to derive the isotherm from the obtained chromatographic data:

Moment Method: This technique involves numerical integration of chromatographic response peaks to determine the first and second moments, providing insights into adsorption equilibrium and kinetic behavior. The mean retention time reflects the adsorption equilibrium (Henry's Law constant), while the dispersion of response peaks is influenced by mass transfer resistance and axial mixing. To ensure accuracy, experiments are performed at low sorbate concentrations within the Henry's Law region, where retention time remains independent of pulse size, validating the assumption of linearity (Tazikeh et al., 2022).

Breakthrough Curve Method: A breakthrough curve plots the adsorbate concentration in the effluent against time. Initially, as the gas mixture flows through a zeolite-packed bed, the adsorbate is retained while the carrier gas exits free of the adsorbed component. Adsorption continues until the zeolite reaches saturation, after which the adsorbate begins to appear in the effluent stream. The breakthrough curve is typically S-shaped and characterized by its midpoint, steepness, and overall shape. Factors influencing breakthrough behavior include gas flow rate, adsorbate concentration, bed size, zeolite quality, and operating temperature. Higher temperatures generally decrease adsorption capacity, leading to shorter breakthrough times. This method provides direct insights into adsorption equilibrium and kinetics through mathematical modeling (Tazikeh et al., 2022).

Gas chromatographic methods offer several advantages over conventional static techniques, including faster data acquisition, applicability over a wider temperature and pressure range, and suitability for analyzing low sorbate concentrations. However, while the moment method is limited to low-concentration regions and requires numerous experimental runs to generate a full isotherm at a given temperature, the breakthrough curve approach allows a more direct and efficient determination of adsorption equilibrium and kinetics.

In this study, the adsorption equilibrium CO_2, CH_4 and N_2 in both commercial binder-free zeolite 13X (13X-BF) (that can be used directly in cyclic adsorption processes such as PSA or TSA) and in the powder form. (13X-P) was studied by using a flow chromatographic technique (by the measurement of breakthrough curves) providing a comprehensive understanding on how commercial binder-free beads manufacture technique can affect or not the overall performance of zeolites as synthesized in powder form.

2.1. Experimental Apparatus to Perform Fixed-Bed Adsorption: Experiments

Fixed-bed adsorption systems play a critical role in industrial gas separation, offering a balance of operational efficiency, design simplicity, and adaptability across a range of applications. They are widely employed in processes such as natural gas purification, air separation, and flue gas treatment (Sherman & Yon, 2000; S, 1995). These systems utilize packed columns filled with porous adsorbents typically zeolites, activated carbons, or metal-organic frameworks which selectively capture gas molecules from flowing mixtures (Da Silva et al., 1999)

The adsorption mechanism is inherently dynamic: as the gas flows through the bed, target species are adsorbed onto the solid surface, while other components continue downstream. Over time, saturation occurs, leading to the formation of breakthrough curves that describe the evolution of outlet concentration over time. These curves provide essential insight into mass transfer rates, equilibrium capacity, and adsorption kinetics parameters critical for performance evaluation and scale-up (Weber, 1980; Shafeeyan et al., 2014).

In this part, we describe the experimental methodology employed to assess the adsorption performance of zeolite 13X in both powder and binder-free forms, for single-component (CO_2, CH_4, N_2). The chapter presents the experimental setup for equilibrium measurements, the breakthrough testing procedures, and the characteristics of the adsorbents studied. These experimental investigations form the basis for the subsequent analysis of breakthrough curves and isotherm modeling using the Langmuir and Dual-Site Langmuir models.

2.2. Experimental Setup for Equilibrium Adsorption Equilibrium and Dynamic Studies

A custom-built fixed-bed breakthrough system was developed to investigate the adsorption behavior of CO_2, CH_4, and N_2 on zeolite 13X in both powder and binder-free forms. The apparatus, shown schematically in Figure 6, is designed to conduct single-component and multicomponent (binary and ternary) experiments under controlled temperature and pressure conditions. It consists of three interconnected sections: gas preparation, adsorption column, and analytical detection by gas chromatography.

In the gas preparation section, high-purity gases CO_2 (99.998%), CH_4 (99.95%), N_2 (99.999%), and helium (99.9998%) are supplied by Air Liquide. Helium serves as both a carrier gas and the reference stream for the Thermal Conductivity Detector (TCD), which measures the concentration of gases based on their thermal conductivity. It is introduced into the system via two independent lines: one directly feeds the reference side of the TCD to establish a baseline signal, while the second is combined with the adsorbate gases to form the desired gas mixture. Flow rates are precisely regulated using mass flow controllers (MFCs; Bronkhorst High-Tech B.V., Netherlands), and the total pressure is maintained using an electronic back-pressure controller (BPC; Bronkhorst High-Tech B.V., Netherlands).

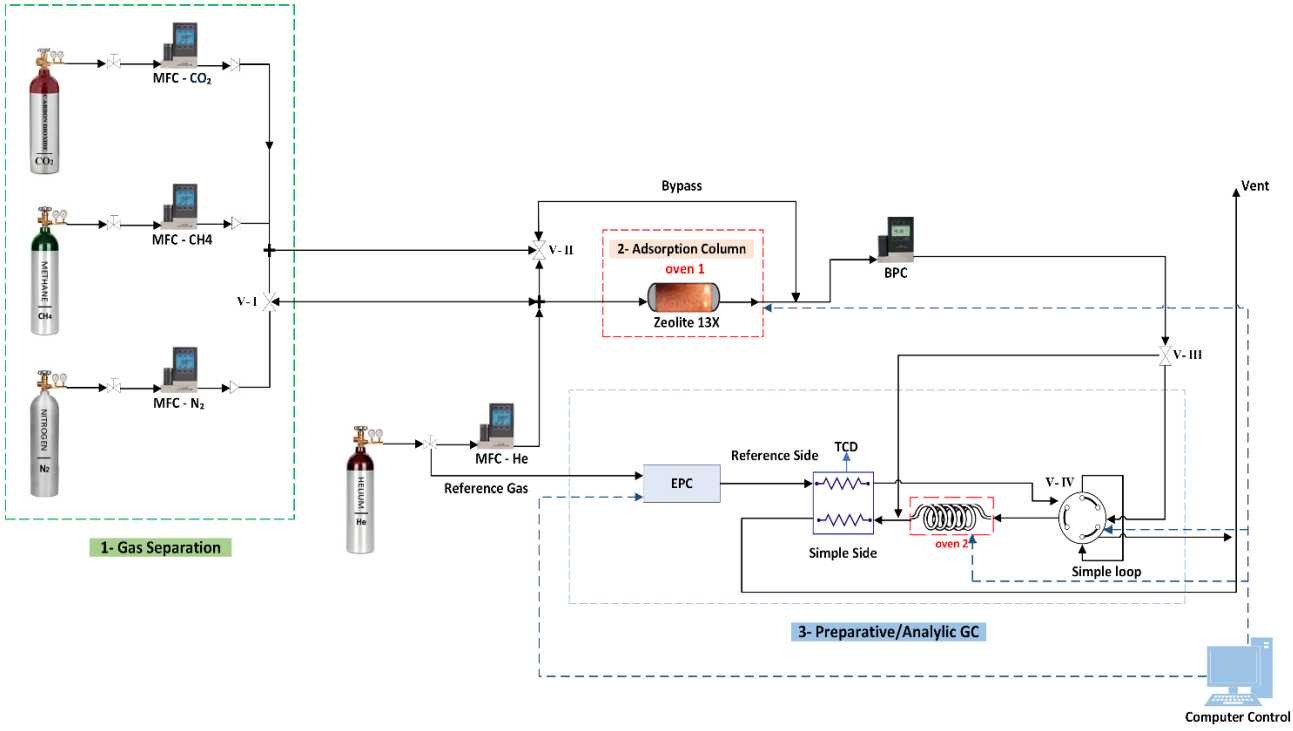

Figure 6. Schematic drawing of the experimental set-up used to perform single- and multicomponent breakthrough experiments to measure the adsorption equilibrium and study the dynamics of adsorption in a fixed bed column.

The mixed gas stream then enters a stainless-steel fixed-bed adsorption column, located within a temperature-controlled oven (Oven 1). The column is packed with zeolite 13X, and its physical characteristics such as column length, internal diameter, adsorbent mass, and particle size are summarized in Table 4. The oven allows for precise thermal control between 306 K and 444 K, relevant to various industrial applications. A thermocouple (TC08; Omega Engineering, USA) placed at the column midpoint ensures stable isothermal conditions throughout each run.

A multi-position valve (V-III) allows the system to operate in either single-component or multicomponent mode. In single-component tests, the column effluent flows directly to the TCD detector (SRI 8610C Gas Chromatograph, USA) for real-time monitoring. For binary or ternary systems, the outlet is directed through a VICI-Valco six-way valve (V-IV) equipped with a fixed-volume sampling loop. In position A, the effluent fills the loop; switching to position B sweeps the

loop's contents with helium into a capillary column housed in a second oven (Oven 2), enabling component separation prior to detection.

The analytical section features a HayeSep packed chromatographic column coupled with a TCD. Data acquisition and analysis are performed using PeakSimple Chromatography Software (USA), allowing for accurate quantification of gas concentrations and breakthrough behavior. The system operates at pressures up to 350 kPa and provides high-resolution insights into both adsorption equilibrium and dynamic response.

This experimental setup forms the basis for the systematic evaluation of gas adsorption on zeolite 13X. It supports detailed analysis of single- and multicomponent adsorption isotherms and enables comparison of performance between the powder and binder-free adsorbent forms under relevant process conditions.

Table 4. Column, Adsorbent and Operating Conditions.

Properties	Value
Bed	
Length (m)	0.07
Internal diameter (m)	0.01
Wall thickness (m)	0.00180
Wall specific heat capacity ($J \cdot kg^{-1} \cdot K^{-1}$)	502
Wall heat conductivity ($W \cdot m^{-1} \cdot K^{-1}$)	15.0
Wall density ($kg \cdot m^{-3}$)	8000
Adsorbent	
Total weight (g)	3.77 (13X-BF) 2.38 (13-P)
Bed density ($kg \cdot m^{3}$)	685 (13X-BF) 432 (13-P)
Bead diameter (mm)	1.20–2.00

2.3. Experimental Procedure for Measuring Breakthrough Curves

The experimental procedure for gas adsorption measurements follows a systematic approach, beginning with adsorbent activation and concluding with the interpretation of breakthrough curves to determine equilibrium loading.

Initially, the zeolite 13X adsorbent is thermally activated within the packed column to remove any moisture or pre-adsorbed species. This is accomplished by heating the column to 623 K for 12 hours under vacuum, while flowing high-purity helium at 10 $mL.min^{-1}$ through the system. This ensures that the adsorbent surface is clean and ready for consistent adsorption measurements.

Following activation, the gas mixture is prepared using mass flow controllers (MFCs), which accurately regulate the flow rates of the inert helium and the target adsorbate gases (CO_2, CH_4, and N_2) to establish the desired partial pressures. The total volumetric flow rate is checked using a bubble flow meter, which can be accessed through a bypass line controlled by valve V2. For additional safety, the bypass can also direct gas flow through a ventilator equipped with electrochemical (EC) sensors. The system pressure is stabilized and maintained via a back-pressure controller (BPC).

Once the gas mixture is prepared, valve V3 is set to initiate either a single-component or multicomponent adsorption experiment. The gas stream is introduced into the adsorption column, and the outlet composition is monitored continuously by a Thermal Conductivity Detector (TCD). The TCD provides a signal that is directly proportional to the concentration of gas exiting the column.

At the onset of each run, the adsorbate is selectively retained by the zeolite bed while helium continues to pass through. As adsorption proceeds and the adsorbent approaches saturation, the outlet concentration of the adsorbate gradually increases. Equilibrium is reached once the outlet concentration equals the inlet. This transition is captured in a breakthrough curve, which typically displays a smooth S-shape profile. These curves provide crucial information on the adsorption behavior and are used to calculate equilibrium parameters.

The adsorbed amount at equilibrium is calculated by integrating the breakthrough curve using the following expression:

$$q_{exp,i} = \frac{1}{m_{ads}} \left(F_{i0} t_n - \int_0^{t_n} F_i \, dt - \varepsilon_b V_c C_{0i} \right) \quad (7)$$

Where:

- $q_{exp,i}$: equilibrium adsorption capacity for component *i* (mol·kg^{-1})
- m_{ads}: mass of adsorbent in the column (kg)
- F_{i0}: molar flow rate of component *i* at the column inlet (mol·s^{-1})
- F_i: molar flow rate at the outlet as a function of time (mol·s^{-1})
- t_n: saturation time when the outlet concentration equals the inlet
- ε_b: bed porosity (–)
- V_c: volume of the packed bed (m³)
- C_{0i}: initial gas-phase concentration of component *i* at the inlet (mol·m^{-3})

2.4. Adsorbents

Two types of zeolites 13X were employed in this study, both supplied by Chemiewerk Bad Köstritz GmbH (Germany). The first material is a binder-free zeolite 13X, commercially available under the trade name Köstrolith® 13XBFK. It exhibits a FAU-type crystalline structure with a Si/Al ratio of 1.18 and is provided in spherical bead form, with particle diameters ranging from 1.2 to 2.0 mm Figure 7(right), named as 13X-BF.

The second material is a micron-sized powdered zeolite 13X, marketed as NaMSXP, named as 13X-P. This sample consists of well-defined crystals with an average particle size of approximately 3.5 µm and a SiO_2/Al_2O_3 ratio of 1.35, as reported by Brandt et al. (2009) Figure 7(left).

Figure 7. Zeolite 13X powder (left) and beads of binder free (right).

2.4.1. Zeolite 13 X Binder Free

To evaluate the surface and structural properties of the binder-free zeolite 13X (Köstrolith® 13XBFK), a series of textural characterization techniques were performed. This material, synthesized without binders, was analyzed using nitrogen adsorption–desorption, mercury intrusion porosimetry, and scanning electron microscopy (SEM). All measurements were conducted at the Laboratory of Porous Solids, University of Málaga.

Nitrogen Adsorption–Desorption Analysis

Textural properties were determined through N_2 adsorption–desorption measurements at 77 K using a Micromeritics ASAP® 2420 surface area and porosimetry analyzer. Prior to the measurements, the samples were degassed under vacuum at 573 K for 12 hours.

The resulting isotherm, shown in Figure 8**,** is classified as Type I according to the updated IUPAC classification, characteristic of microporous materials. A steep uptake in the low relative pressure region ($p/p_o = 10^{-4}$ to 10^{-2}) confirms the presence of micropores, while a slight increase in uptake at higher p/p_o values (up to 0.9) suggests the presence of a small fraction of meso- and macropores.

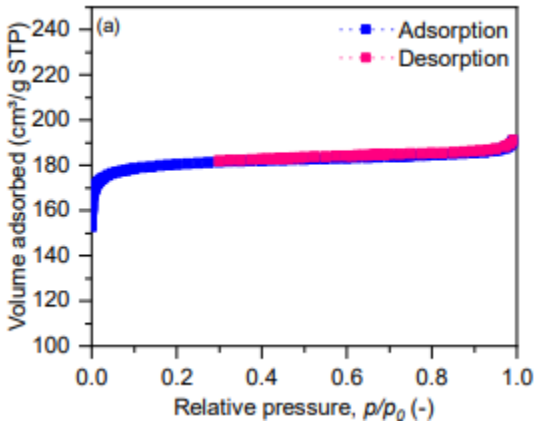

Figure 8. N2 adsorption equilibrium isotherm at 77 K on binder-free (a) 13X.

Table 5. Textural properties of the binder-free 13X.

Adsorbent Type	13XBFK
N_2 adsorption / desorption	
Langmuir surface area ($S_{Langmuir}$)	792 $m^2.g^{-1}$
External surface area (S_{ext})	9.95 $m^2 . g^{-1}$
Micropore surface area (S_{mic})	782 $m^2 .g^{-1}$
Micropore volume (V_{mic})	276 $mm^3 .g^{-1}$
Total Pore Volume (V_{Total})	475 $mm^3 .g^{-1}$

Mercury Intrusion Porosimetry

Further porosity characterization was performed using mercury (Hg) intrusion porosimetry (MIP), conducted using a pore size analyzer (Micromeritics AutoPore IV 9500). The measurements were conducted after sample activation, using a contact angle of 130° and covering a pressure range from 0.003 to 207 MPa. The results confirm the predominantly microporous nature of 13XBFK, with additional transport macropores that may facilitate mass transfer during dynamic adsorption processes.

Table 6. Summary of mercury porosimetry results.

Adsorbent Type	13XBFK
Mercury porosimetry	
Total intrusion volume	0.238 mL. g^{-1}
Total pore area	4.61 m^2. g^{-1}
Median pore diameter (volume)	600 nm
Median pore diameter (area)	18.9 nm
Average pore diameter (4V/A)	207 nm
Bulk density at 0.0036 MPa	1.22 g .mL^{-1}
Apparent (skeletal) density	1.73 g. mL^{-1}
Porosity	0.292

Scanning Electron Microscopy (SEM)

SEM images were obtained using a JEOL JSM-6490 microscope operating at a resolution of 3.0 nm. The binder-free zeolite 13X particles are observed in spherical bead form, exhibiting a polycrystalline morphology. The crystals within each bead are approximately 1 µm in size and display mostly cubic to slightly rounded shapes. At ×15000 magnification, crystal intergrowth and

a highly textured surface are evident features that are potentially favorable for internal diffusion and gas accessibility (see figure 9).

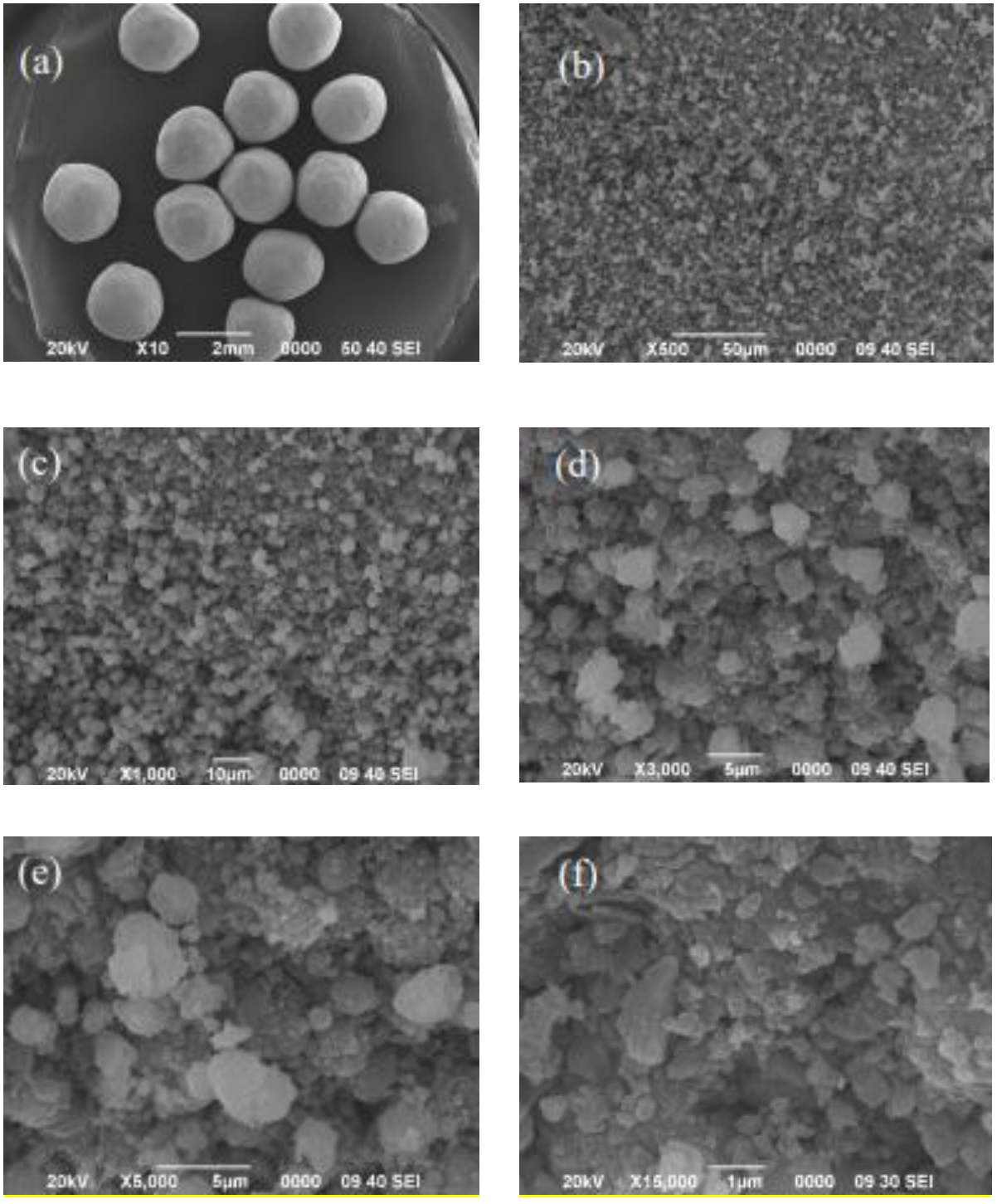

Figure 9. SEM images of 13X-BF at different scales and magnification: (a) ×10, (b) ×500, (c) ×1000, (d) ×3000, (e) ×5000, and (f) ×15000.

2.4.2. Zeolite 13X Powder

The NaMSXP zeolite 13X was supplied in powder form, which necessitated agglomeration prior to its use in the fixed-bed adsorption experiments. The direct use of powdered adsorbents was avoided due to the risk of increasing pressure drop and potential clogging within the adsorption column, which could compromise the flow dynamics and operational stability of the system.

To agglomerate the crystals, the powder was compacted using a stainless-steel cylindrical mold and piston, coupled with a hydraulic press (SPECAC, Orpington, UK) rated for 15 tons. The pressing procedure was carried out at a load of 2.0 tons, applied consistently for 5 minutes (Henrique, 2015).

After compaction, the pellets were mechanically broken into smaller agglomerates and sieved to achieve a controlled particle size distribution. For the adsorption experiments, a 5.1 mm mesh sieve was used to ensure uniformity of particle size within the packed bed (see figure 10).

Figure 10. Zeolites 13X powder agglomerates (13X-P).

2.4.2.1. Structural and Textural Properties of Zeolite Powder

This material consists of pure zeolite 13X crystals in microsized powder form, without binders or additives. In scientific literature, such powders are commonly referred to as "13X crystals," as they correspond to the intrinsic, unmodified crystalline phase of zeolite.

According to Dirar & Loughlin (2013) the 13X zeolite crystals used in their adsorption studies exhibit a typical faujasite (FAU) structure with well-defined cubic morphology. The average crystal size ranges between 2.5 and 3.5 µm, which is consistent with the specifications of the NaMSXP sample used in the present work.

The NaMSXP zeolite refers to the powdered 13X material employed as the raw precursor for the synthesis of binder-free NaMSX molecular sieves. These binder-free materials offer superior adsorption performance owing to their purely crystalline zeolitic composition and a more favorable pore structure, characterized by reduced mesoporosity compared to conventional zeolites containing binders (Schumann et al., 2011).

Chapter 3
Results and Discussions

3. RESULTS AND DISCUSSION

3.1. Pure Component Adsorption

The adsorption equilibrium of pure CO_2, CH_4, and N_2 was extensively investigated on two distinct zeolite 13X adsorbents: a binder-free formulation (Köstrolith® 13XBFK-13X-BF) and a microsized powder agglomerates variant (NaMSXP-13X-P). The experiments were performed using a dynamic breakthrough method under carefully controlled conditions, three temperatures (308, 328, and 348 K) and partial pressures fixed at 10, 40, 120 and 350 kPa. A comprehensive summary of the experimental parameters including the individual flow rates of each adsorbate (N_2, CH_4, or CO_2), the inert carrier gas (helium), and the corresponding total and partial pressures is provided in Table 7 for the binder-free zeolite and in Table 8 for the powdered counterpart.

Table 7. Fixed bed experimental conditions for single component adsorption on binder-free 13X zeolite (13X-BF).

Run	temp. (K)	Total pressure (kPa)	Helium flow rate * (mL/min)	Adsorbed specie flow rate * (mL/min)	Partial pressure adsorbate (kPa)	loading (mol/kg)
			CO_2			
1.1	308	100	52.0	5.8	10	4.24
1.2		100	34.5	23.0	40	5.53
1.3		300	34.9	23.2	120	6.26
1.4		500	17.2	40.3	350	6.99
2.1	328	100	48.5	5.4	10	3.16
2.2		100	33.4	22.3	40	4.91
2.3		300	32.2	21.4	120	5.68
2.4		500	16.3	37.8	350	6.51
3.1	348	100	45.5	5.1	10	2.60
3.2		100	30.5	20.3	40	3.85
3.3		300	30.4	20.2	120	4.99
3.4		500	15.2	35.4	350	5.95
			CH_4			
1.1	308	100	52.1	5.8	10	0.08
1.2		100	34.7	23.1	40	0.31
1.3		300	34.7	23.2	120	0.82
1.4		500	17.4	40.7	350	1.94
2.1	328	100	49.1	5.4	10	0.07
2.2		100	32.7	21.8	40	0.22
2.3		300	32.7	21.8	120	0.57
2.4		500	16.4	38.1	350	1.41
3.1	348	100	46.2	5.1	10	0.05
3.2		100	30.8	20.5	40	0.16
3.3		300	30.8	20.5	120	0.42
3.4		500	15.5	36.0	350	1.13
			N_2			
1.1	308	100	51.7	5.8	10	0.06
1.2		100	34.6	22.9	40	0.23
1.3		300	34.4	22.9	120	0.53
1.4		500	17.2	40.1	350	1.19
2.1	328	100	48.9	5.4	10	0.05
2.2		100	32.5	21.7	40	0.16
2.3		300	32.5	21.6	120	0.40
2.4		500	16.2	37.7	350	0.94
3.1	348	100	45.8	5.0	10	0.03
3.2		100	30.4	20.3	40	0.11
3.3		300	30.4	20.3	120	0.27
3.4		500	15.2	35.4	350	0.72

* Standard Temperature and Pressure condition (273.15 K, 100 kPa).

Table 8. Fixed bed experimental conditions for single component adsorption on powder form 13X zeolite (13X-P).

Run	temp. (K)	Total pressure (kPa)	Helium flow rate * (mL/min)	Adsorbed specie flow rate * (mL/min)	Partial pressure adsorbate (kPa)	loading (mol/kg)
			CO_2			
1.1	308	100	52.7	5.8	10	4.14
1.2		100	34.7	23.0	40	5.23
1.3		300	34.9	23.3	120	6.04
1.4		500	17.6	41.0	350	6.75
2.1	328	100	49.2	5.5	10	2.77
2.2		100	32.8	21.9	40	4.56
2.3		300	33.0	22.0	120	5.37
2.4		500	16.4	38.4	350	6.31
3.1	348	100	46.5	5.2	10	2.39
3.2		100	31.0	20.7	040	3.78
3.3		300	31.0	20.7	120	4.64
3.4		500	15.5	36.3	350	5.75
			CH_4			
1.1	308	100	51.7	5.7	10	0.09
1.2		100	34.4	23.0	40	0.35
1.3		300	34.5	22.9	120	0.87
1.4		500	17.3	40.4	350	1.89
2.1	328	100	48.6	5.4	10	0.07
2.2		100	32.3	21.7	40	0.25
2.3		300	33.0	22.0	120	0.57
2.4		500	16.5	38.5	350	1.45
3.1	348	100	46.6	5.2	10	0.05
3.2		100	31.0	20.7	40	0.18
3.3		300	31.1	20.6	120	0.44
3.4		500	15.5	36.4	350	1.20
			N_2			
1.1	308	100	52.3	5.8	10	0.06
1.2		100	34.9	23.3	40	0.25
1.3		300	35.1	23.4	120	0.54
1.4		500	17.7	41.1	350	1.23
2.1	328	100	49.4	5.5	10	0.04
2.2		100	32.9	21.9	40	0.17
2.3		300	32.9	22.0	120	0.37
2.4		500	16.4	38.4	350	1.00
3.1	348	100	46.5	5.1	10	0.03
3.2		100	30.8	20.4	40	0.12
3.3		300	30.8	20.3	120	0.30
3.4		500	15.5	36.1	350	0.80

* Standard Temperature and Pressure condition (273.15 K, 100 kPa).

The amount of gas adsorbed in each experiment was quantified directly from the breakthrough curves using the integration method described in Appendix (Equation 7). However, because different adsorbent masses were used for the two zeolites, because of their distinct bulk densities and physical morphologies, a direct comparison based on concentration versus time would not be appropriate and could lead to misleading conclusions about their performance.

To overcome this, an alternative normalization approach was employed for the axis of time. The comparison between the two materials was made by plotting the ratio of the normalized molar fraction of the adsorbed gas versus the molar flow of adsorbate fed per unit mass of adsorbent. The x-axis is thus expressed in terms of molar loading per unit mass, as follows:

$$\frac{tF_i}{m_s} = \left[\frac{\min mol_i}{kg\,min}\right] = \left[\frac{mol_i}{kg}\right] \quad (8)$$

Where, t is the time, F_i is the feed flux of the adsorbable species at the entrance of the column and m_s the mass of adsorbent in the column.

This approach enables a fair and quantitative comparison between the performance of the two zeolites under identical operating conditions, regardless of the physical amount of material used. It also allows for a more accurate evaluation of the intrinsic adsorption behavior and efficiency of each adsorbent toward individual gas components.

The normalized breakthrough curves for nitrogen (N_2), methane (CH_4), and carbon dioxide (CO_2) adsorption on zeolite 13X comparing the powder form (13X-P) and the binder-free form (13X-BF) were obtained under the aforementioned conditions. The detailed breakthrough profiles for each gas are presented and analyzed individually in the following sections as a function of temperature and pressure and for each component studied and the real time breakthroughs as measured in the SI.

3.1.1. Breakthrough Curves of Nitrogen (N_2)

The normalized breakthrough curves for nitrogen (N_2) adsorption on zeolite 13X, comparing the powder form (13X-P) and the binder-free form (13X-BF), are presented in Figure 11.

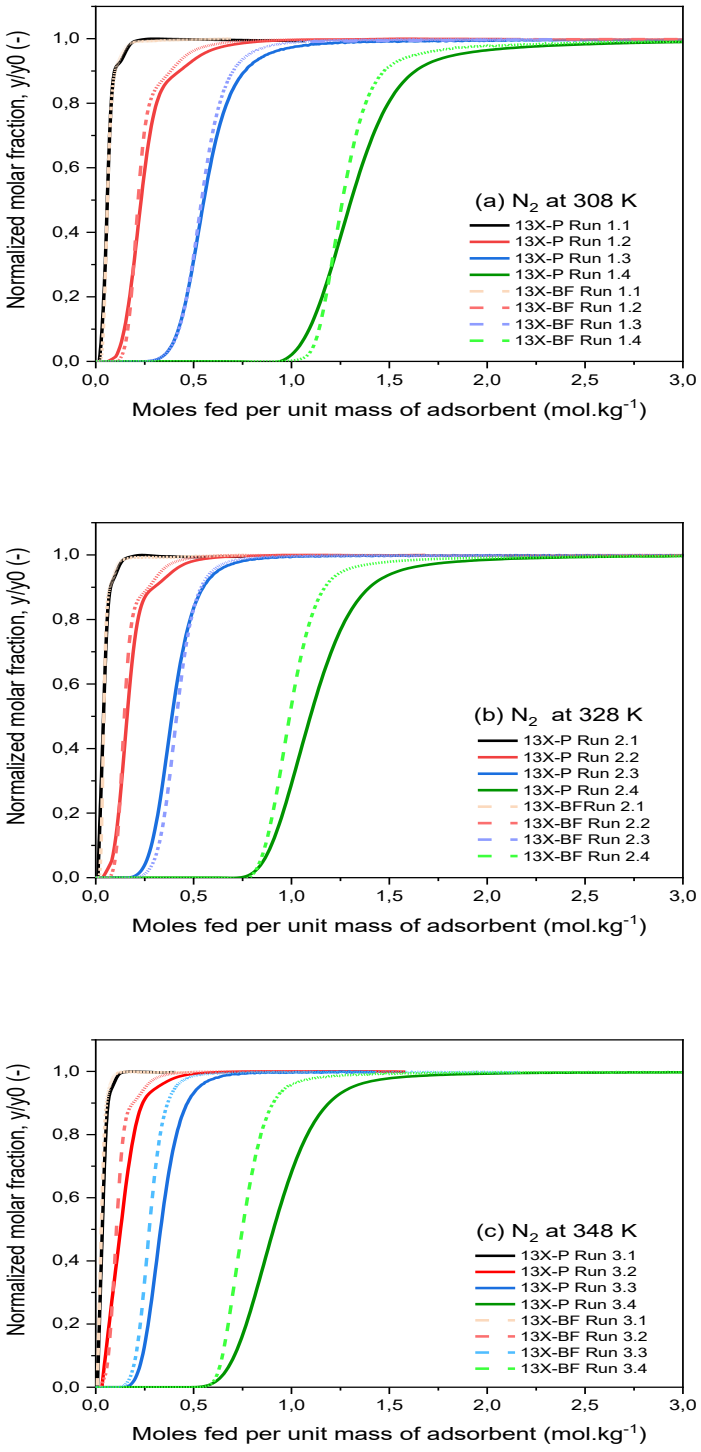

Figure 11. Experimental breakthrough curves for Nitrogen on zeolite 13X-BF and 13X-P at different temperatures: (a) 308 K, (b) 328 K, and (c) 348 K.

At 308 K, the adsorption capacity increased proportionally with pressure. The breakthrough curves for 13X-BF and 13X-P were practically superimposed in all runs, with minor delays observed for 13X-BF only in Run 1.4. The maximum relative difference was around 5–7%, indicating that both materials exhibit very similar dynamic performance under the tested conditions and adsorption loadings.

At 328 K, the adsorption capacity decreased slightly compared to the results at 308 K due to the exothermic nature of physisorption. The breakthrough curves remained nearly identical in the first three runs, with a slight delay for 13X-BF only in Run 2.4 (350 kPa). The relative difference remained below 5%, reinforcing the kinetic and equilibrium equivalence between both materials.

It is important to highlight that 13X-BF has a higher bulk density (685 kg/m³ vs. 432 kg/m³ for 13X-P), which may contribute to more uniform packing, reduced axial dispersion, and improved mass transfer efficiency.

At 348 K, the lowest adsorption capacities in the study were recorded, reflecting the effect of temperature on physisorption. At this temperature, breakthrough profiles remained superimposed in the initial runs. However, at 350 kPa (Run 3.4), 13X-P outperformed 13X-BF, displaying a higher saturation capacity. Although 13X-BF initially showed a faster adsorption kinetic profile, it tended to saturate earlier possibly due to internal diffusion limitations or reduced thermal dissipation capacity.

The lower overall adsorption capacity for N_2 compared to gases like CH_4 and CO_2 can be attributed to weak electrostatic interactions between N_2 and the cationic sites of zeolite 13X. This behavior results from the low quadrupole moment and poor polarizability of the N_2 molecule (Jedli et al., 2024; Falkowska et al., 2025).

Despite these limitations, the differences between 13X-BF and 13X-P were minimal, confirming that the binder-free form (13X-BF) maintains comparable efficiency to the agglomerated material (13X-P). These findings validate the experimental methodology and support the applicability of both zeolite 13X forms in gas separation processes.

3.1.2. Breakthrough Curves of Methane (CH_4)

The normalized breakthrough curves for methane (CH_4) adsorption on zeolite 13X, comparing the binder-free (13X-BF) and powdered agglomerates (13X-P), are presented in Figure 12 across the temperature range of 308–348 K and pressures parcial from 10 to 350 kPa. All experiments were conducted in a fixed-bed setup with pure CH_4 as feed gas. Cumulative molar uptake was normalized by adsorbent mass ($mol \cdot kg^{-1}$) to allow meaningful comparison between the two zeolite forms.

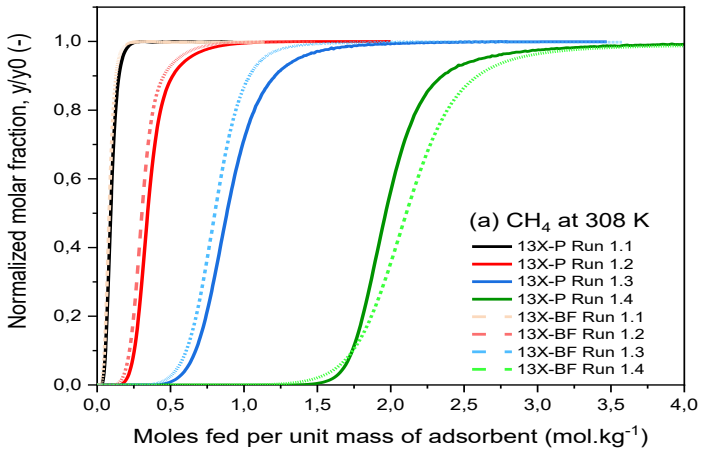

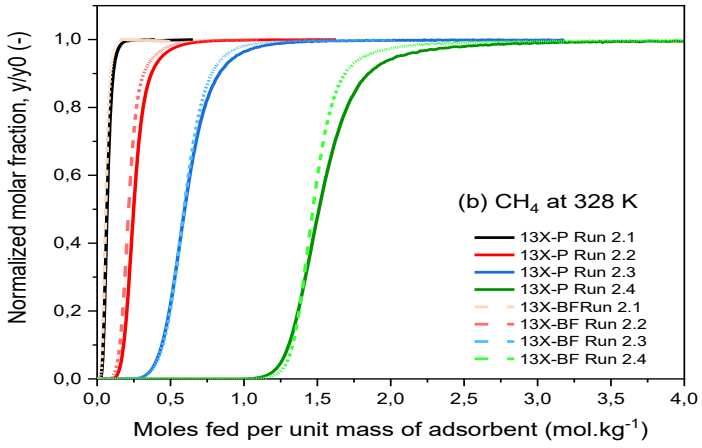

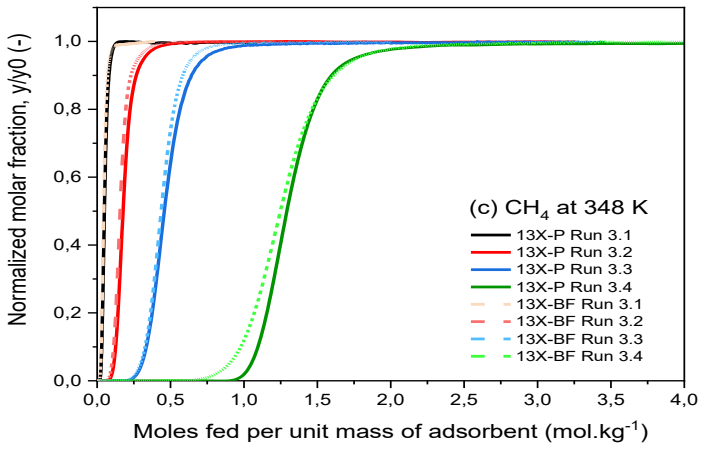

Figure 12. Experimental breakthrough curves for Methane on zeolite 13X-Powder and 13X-Binder-Free at different temperatures: (a) 308 K, (b) 328 K, and (c) 348 K.

At 308 K, the saturation capacity of CH_4 increased progressively with pressure, ranging from 0.375 mol·kg^{-1} (Run 1.1, 10 kPa) to 3.5 mol·kg^{-1} (Run 1.4, 350 kPa). In Runs 1.1 and 1.2, the breakthrough profiles for 13X-BF and 13X-P were nearly superimposed, indicating identical adsorption behavior under low and intermediate pressure conditions.

For Run 1.3 (120 kPa), a delay was observed in the 13X-BF breakthrough profile compared to 13X-P, with the 13X-BF curve displaying a slightly wider Mass Transfer Zone (MTZ). This observation is critical as it highlights a kinetic trade-off inherent to material morphology. The 13X-BF structure, presented as spherical beads with a significantly higher bulk density (685 kg·m^{-3} vs. 432 kg·m^{-3} for 13X-P), benefits from reduced axial dispersion and a more uniform flow distribution through the packed column. However, the slightly wider MTZ in the 13X-BF profile suggests a counteracting effect: an increased intraparticle diffusion resistance within its polycrystalline bead structure compared to the manually agglomerated powder (13X-P). While overall adsorption capacities remained similar, this kinetic difference indicates that the mass transfer within the binder-free particle itself may be marginally slower.

At 328 K, the total adsorption capacity decreased in all runs, as expected for an exothermic physisorption process. The breakthrough curves remained almost identical in all runs, with only a minor delay observed for 13X-BF in Run 2.4 (350 kPa), confirming that both adsorbents maintain comparable performance even at elevated temperatures.

At 348 K, the lowest adsorption capacities were recorded, ranging from 0.125 mol·kg^{-1} (Run 3.1) to ~2.125 mol·kg^{-1} (Run 3.4). In Run 3.4 (350 kPa), 13X-BF demonstrated slightly better initial accessibility, possibly due to reduced external film resistance or a higher accessible surface area. However, both forms reached saturation at the same time, and their total capacities converged, confirming equivalent equilibrium performance.

In summary, CH_4 adsorption dynamics were functionally equivalent between 13X-BF and 13X-P under all tested conditions. Pressure exerted a more significant influence on adsorption performance than temperature, highlighting the importance of thermodynamic driving force over adsorption capacity. Higher temperatures reduced CH_4 uptake, as expected for an exothermic process.

The higher packing density of 13X-BF (685 $kg \cdot m^{-3}$) provided slight advantages in axial homogeneity and reduced dispersion, though these were offset by internal diffusion limitations at high pressures. Both adsorbents proved suitable for dynamic methane separation processes such as Pressure Swing Adsorption (PSA). The choice between 13X-BF and 13X-P will depend on specific process requirements, such as prioritizing initial adsorption kinetics versus overall mass transfer efficiency.

3.1.3. Breakthrough Curves of Carbon Dioxide (CO_2)

The dynamic performance of carbon dioxide (CO_2) adsorption on zeolite 13X, comparing the binder-free form (13X-BF) and the agglomerated powder form (13X-P), is presented in Figure 13, under the same temperature and partial pressure conditions previously adopted.

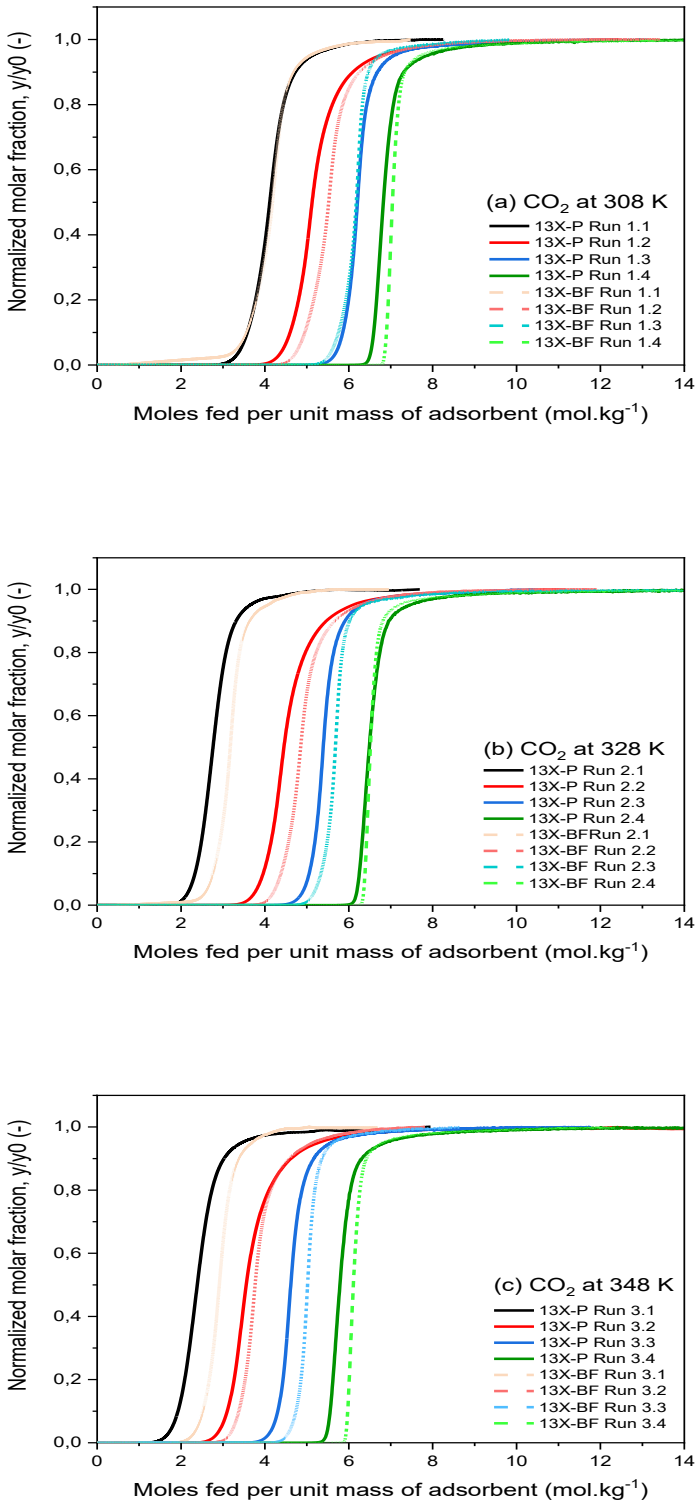

Figure 13. Experimental breakthrough curves for carbon Dioxide on zeolite 13X-Powder and 13X-Binder-Free at different temperatures: (a) 308 K, (b) 328 K, and (c) 348K.

At 308 K, saturation capacities increased with partial pressure, ranging from 6.5 mol·kg^{-1} at 10 kPa (Run 1.1), to approximately 8.5 mol·kg^{-1} at 40 and 120 KPa (Runs 1.2 and 1.3), and reaching up to 9.5 mol·kg^{-1} at 350 KPa (Run 1.4). In all cases, the breakthrough curves of 13X-BF and 13X-P were nearly superimposed, indicating similar adsorption behavior between the two materials.

A subtle difference was noted in the profile shapes, however, leading to an important structural insight. The 13X-BF material showed minor delays at partial pressures of 40 and 350 kPa, where the Mass Transfer Zone (MTZ) appeared slightly broader. This indicates a kinetic trade-off resulting from the binder-free bead morphology. While the higher packing density of 13X-BF (685 kg·m $^{-3}$) contributes to superior bed homogeneity and reduced axial dispersion, these advantages are partially offset by increased intraparticle diffusion resistance within the highly compacted, polycrystalline bead structure compared to the manually agglomerated powder (13X-P).

At 328 K, a moderate reduction in adsorption capacities was observed, with values ranging from 5.5 mol·kg^{-1} (Run 2.1, 10 KPa), 7.2 mol·kg^{-1} (Run 2.2, 40 KPa), 8.3 mol·kg^{-1} (Run 2.3, 120 KPa), and up to 9.0 mol·kg^{-1} (Run 2.4, 350 KPa), confirming the exothermic nature of CO_2 physisorption. A subtle delay in 13X-BF breakthrough appeared at low and intermediate pressures (10–120 KPa), though this difference became negligible at 350 KPa. This behavior is attributed to thermally induced reductions in adsorption affinity (Park et al., 2016).

At 348 K, adsorption capacities declined further due to thermal effects, ranging from 5.5 mol·kg^{-1} (Run 3.1, 10 KPa), 7.4 mol·kg^{-1} (Runs 3.2 and 3.3, 40 and 120 KPa), and up to ~8.9 mol·kg^{-1} (Run 3.4, 350 KPa). These results emphasize the thermal sensitivity of CO_2 adsorption on zeolites and highlight the importance of temperature optimization in high-pressure applications.

Across all temperatures, the differences between 13X-BF and 13X-P remained once more minimal, with similar saturation times observed in most runs. This confirms that the binder-free form (13X-BF) performs equivalently to the micronized powder agglomerates (13X-P) under dynamic conditions.

The slightly lower axial dispersion of 13X-BF attributed to its higher packing density, may offer benefits in industrial applications such as PSA (Pressure Swing Adsorption) systems. However, both adsorbents demonstrated comparable total adsorption capacities for CO_2.

Among the three gases studied (N_2, CH_4, and CO_2), CO_2 consistently showed the highest adsorption capacity, reaching up to 9.5 $mol \cdot kg^{-1}$ at 350 kPa. This behavior is attributed to its high quadrupole moment and strong electrostatic interactions with Na^+ cations in the FAU structure of zeolite 13X. These interactions promote selective and efficient adsorption, making CO_2 the gas with the highest affinity for the adsorbent among the three.

CH_4 exhibited a moderate adsorption capacity, primarily influenced by London dispersion forces and sensitive to changes in pressure and temperature. While less polarizable than CO_2, CH_4 still interacts significantly with zeolite 13X, particularly under high-pressure conditions.

In contrast, N_2 showed the lowest adsorption capacities due to its weak electrostatic interactions with the cationic sites of the zeolite. The low quadrupole moment and limited polarizability of N_2 reduce its affinity for the adsorbent, resulting in significantly lower uptake compared to CO_2 and CH_4.

The results demonstrated a clear technical equivalence between the binder-free form (13X-BF) and the agglomerated powder form (13X-P) for all gases tested. The breakthrough curves of both materials were nearly identical under all conditions, with only minor kinetic delays observed for 13X-BF at high flow rates or elevated temperatures. The higher packing density (685 $kg \cdot m^{-3}$) of 13X-BF may reduce axial dispersion and improve bed homogeneity. The absence of binders may also facilitate initial accessibility to adsorption sites, particularly under low-pressure conditions. However, at high pressures or elevated temperatures, slower intraparticle diffusion can result in a broader mass transfer zone (MTZ), limiting adsorption kinetics compared to 13X-P.

Furthermore, as partial pressure increased, the number of moles fed before breakthrough also increased, reflecting thermodynamic consistency and behavior aligned with Type I isotherms. Conversely, for a given pressure, the number of moles fed per unit mass of adsorbent decreased with increasing temperature, confirming the exothermic nature of the physisorption process and the reduced affinity of CO_2 for the adsorbent under higher thermal conditions.

In summary, this study provides a solid foundation for the application of zeolite 13X in gas separation processes, particularly for CO_2 capture. The equivalent performance of 13X-BF and 13X-P, combined with the structural and mechanical advantages of the binder-free form, supports its viability in industrial applications.

3.2. Single component adsorption equilibrium isotherms

The analysis of breakthrough curves plays a crucial role, as it enables the determination of adsorption isotherms. These isotherms describe the relationship between the amount of gas adsorbed and the equilibrium pressure at constant temperature and are essential for evaluating adsorbent performance.

The experimental data was fitted using established equilibrium models. For N_2 and CH_4, the Langmuir model was applied due to their simpler adsorption behavior. In contrast, the Dual-Site Langmuir (DSL) model was employed for CO_2 to account for its stronger affinity to the zeolite surface and its more complex adsorption characteristics.

Model fitting was performed using a numerical procedure that minimizes the absolute deviation (Δq) between the experimental values (q) and the predicated or calculated values (q_{cal}) across all experimental runs (M) by appling the Langmuir model (equation .1), and using the DSL model (equation.3) and the same numerical procedure (minimizing equation.7). The objective function used in the optimization was:

$$\Delta q = \sum_{i=1}^{M} (q_{cal} - q\ )^2 \tag{9}$$

Beyond capacity estimation, adsorption isotherm models also offer critical insights into the physicochemical properties of porous materials, such as energetic heterogeneity. These parameters are deeply influenced by the nature of the interaction between the adsorbate and the adsorbent, which in turn governs the shape and features of the resulting isotherms. Thus, modeling adsorption equilibrium is not only essential for process design but also for understanding the underlying mechanisms at the molecular level.

In this study, the adsorption isotherms of N_2, CH_4, and CO_2 were measured at three temperatures (308, 328, and 348 K) using two forms of zeolite 13X: powder and binder-free. The experiments were conducted in five partial pressures 10 ,25,50,150 and 350 kPa.

3.2.1. Physicochemical Properties of Adsorbates and Their Role

Nitrogen (N_2), methane (CH_4), and carbon dioxide (CO_2) were selected as adsorbates due to their relevance in gas separation and environmental applications. Their key molecular properties, which directly influence adsorption behavior, are summarized in Table 9.

Table 9. Molecular properties of the studied gases (Source from Golipour et al., 2019).

Gas	Properties			
	Kinetic diameter (Å)	**Dipole moment (*10^{18} seu cm)**	**Quadrupole moment (*10^{-26} seu cm^2)**	**Polarizability ($Å^3$)**
N_2	3.63	0	1.52	1.76
CH_4	3.80	0	0	2.45
CO_2	3.28	0	4.30	2.51

The interaction between these gas molecules and the zeolitic framework is strongly influenced by their respective physicochemical properties. In particular, the presence of exchangeable cations such as Na^+ in the FAU structure of zeolite 13X creates local electric fields that can interact favorably with molecules exhibiting polarizability or quadrupole moments.

Carbon dioxide (CO_2), despite being non-polar, has a relatively small kinetic diameter and the highest quadrupole moment among the three gases. This makes it especially responsive to the electrostatic fields near cationic sites, resulting in strong adsorption interactions and higher capacities. Such behavior has been consistently reported in the literature (Golipour et al., 2019).

Methane (CH_4), while lacking a quadrupole or dipole moment, possesses significant polarizability. This allows temporary induced dipoles to form in the presence of the zeolite's electric field, facilitating moderate adsorption via dispersion forces.

Nitrogen (N_2) presents the lowest adsorption capacity among the three gases, which can be attributed to its relatively small quadrupole moment and low polarizability. Although it does experience weak electrostatic interactions, these are insufficient to generate strong adsorption, particularly when compared to CO_2 (Harlick & Tezel, 2004).

The trend in adsorption capacity ($CO_2 > CH_4 > N_2$) aligns closely with the increasing quadrupole moment and polarizability of the gases. These physicochemical properties are essential for interpreting the isotherm behavior presented in the following sections.

3.2.2. Adsorption Equilibrium of CO_2 in Both of Zeolite 13X

Carbon dioxide (CO_2) exhibits a high quadrupole moment and significant polarizability, properties that strongly influence its adsorption behavior. Due to its uneven charge distribution, CO_2 interacts intensely with the electric fields near cationic sites on adsorbent surfaces, especially those found in zeolites such as 13X (Mulgundmath et al., 2011). Zeolite 13X, a sodium-form aluminosilicate with a faujasite-type structure (NaX), is rich in Na^+ cations and exhibits a heterogeneous electrostatic surface, which promotes selective and strong adsorption of polar molecules such as CO_2 (Golipour et al., 2019). Furthermore, its well-defined microporous structure provides molecular sieving properties, enabling the preferential adsorption of smaller and more polarizable gases like CO_2 over non-polar species such as N_2 and CH_4 (Cavenati et al., 2004).

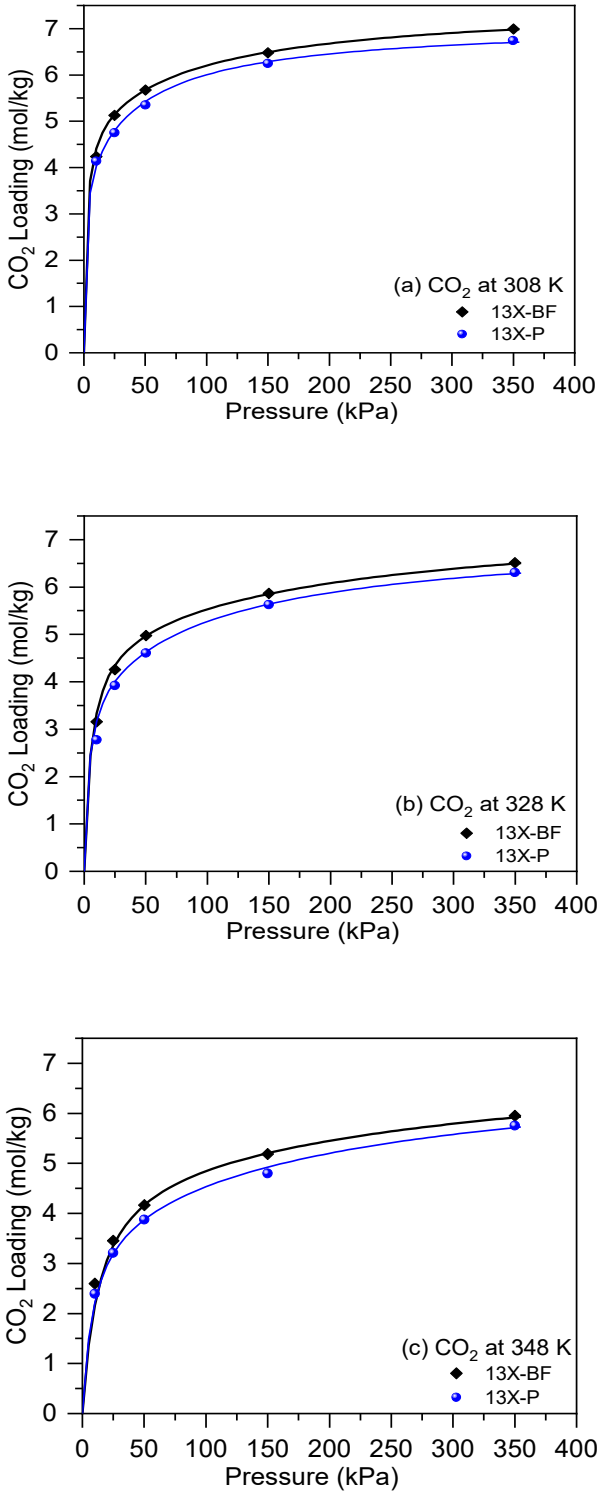

Figure 14. Comparison of CO_2 adsorption isotherms at (a) 308, (b) 328, and (c) 348 K between binder-free 13X and powder-form 13X zeolites. Experimental = symbols; Numerical = lines.

Figure 14 displays the experimental CO_2 adsorption isotherms obtained at three temperatures (308, 328, and 348 K) for both the powder (13X-P) and binder-free (13X-BF) forms of zeolite 13X. The resulting curves exhibit Type I isotherm behavior, which is characteristic of microporous materials, indicating high initial affinity followed by gradual saturation as pressure increases. A pronounced adsorption uptake at low pressures reflects strong initial interactions between CO_2 and the active adsorption sites. This behavior aligns with typical physisorption processes, which are known to be exothermic in nature (Streb & Mazzotti, 2021).

When comparing the two forms, the binder-free zeolite (13X-BF) shows slightly higher or equivalent adsorption capacities compared to the agglomerated powder form (13X-P) under the various conditions tested. This behavior is not due to chemical differences between the samples, but rather to physical and structural factors resulting from the preparation method.

The pressure effect is clearly visible in both materials, with CO_2 uptake increasing as pressure rises. For example, at 308 K, CO_2 adsorption on 13X-BF increases from 4.24 mmol/g at 10 kPa to 6.99 mmol/g at 350 kPa, while 13X-P ranges from 4.14 mmol/g to 6.74 mmol/g over the same interval. The effect of temperature follows expected exothermic behavior. At 10 kPa, 13X-BF capacity drops from 4.24 mmol/g (308 K) to 2.45 mmol/g (348 K), and for 13X-P from 4.14 mmol/g to 2.39 mmol/g.

At 328 K, differences become more evident at low pressure: at 10 kPa, binder-free material exhibits a 14% higher capacity (3.16 vs. 2.77 mmol/g), while at 350 kPa the difference narrows to ~3%. This suggests that 13X-BF is particularly suitable for low partial pressure CO_2 capture such as post-combustion applications. Even at 348 K, where capacity is generally lower due to increased temperature, binder-free material retains an 8.8% advantage at 10 kPa. This sustained superiority may be linked to greater thermal stability and improved access to active sites.

These results confirm the stronger adsorption performance of the binder-free 13X across operational conditions. Furthermore, values obtained here (e.g., 6.99 mmol/g at 350 kPa, 308 K) compare favorably with those reported in literature for standard 13X. For instance, Cavenati et al. (2004) reported values around 3–4 mmol/g at 298 K and 1 bar. The performance of both forms in

this study especially binder-free highlights the significant role of material preparation in CO_2 capture.

Following the direct comparison of isotherm data, the adsorption model parameters obtained via fitting with the Dual-Site Langmuir (DSL) equation (Table 10) provide a complementary perspective on the adsorption mechanisms. This section focuses on the theoretical maximum capacities, affinity constants, and adsorption enthalpies for the two zeolite 13X forms.

Table 10. Adsorption equilibrium model parameters for sorption of CO_2 on binder-free and powder 13X zeolite.

	Species	q_m (mol·kg^{-1})		b (kPa^{-1})[a]		(ΔH_i) (kJ·mol^{-1})	
		q_{m1}	q_{m2}	b_1	b_2	$(\Delta H_i)_1$	$(\Delta H_i)_2$
13X-BF	CO_2	4.96	2.61	0.521	0.0105	-43.6	-34.5
13X-P		3.88	3.23	0.859	0.0203	-44.7	-35.0

[a] The reference temperature used is 308 K.

Table 10 presents the adsorption model parameters of CO_2 fitted using the Dual-Site Langmuir (DSL) equation for both binder-free (BF) and compacted powder (P) forms of zeolite 13X. The BF sample exhibits a slightly higher total adsorption capacity (7.57 mol·kg^{-1}) compared to the powder form (7.11 mol·kg^{-1}), in agreement with the experimental performance observed previously. This can be attributed to its higher bed density (685 kg/m^3 vs. 432 kg/m^3), absence of binder, and improved micropore accessibility, or even experimental errors.

The affinity constants (b_1 = 0.859 kPa^{-1} and b_2 = 0.0203 kPa^{-1}) obtained for the powder form were higher than those of the binder-free sample (b_1 = 0.521 kPa^{-1}; b_2 = 0.0105 kPa^{-1}). This difference may be related to variations in particle morphology. However, it does not imply a higher overall adsorption capacity, which was found to be comparable or even slightly superior for the binder-free.

The adsorption enthalpies support this interpretation. The more negative values for the powder ($(\Delta H_i)_1$ = –44.7 kJ·mol^{-1}; $(\Delta H_i)_2$ = –35.0 kJ·mol^{-1}) compared to BF ($(\Delta H_i)_1$ = –43.6 kJ·mol^{-1}; $(\Delta H_i)_2$ = –34.5 kJ·mol^{-1}) suggest slightly stronger interactions in the powder.

When compared with literature, the modeled total capacities for both forms are consistent with Streb & Mazzotti (2021), who report 7.268 mol·kg^{-1} for zeolite 13X, and Cavenati et al. (2004), who found 7.901 mol·kg^{-1} using a multisite model. However, they fall below the ideal saturation value of 10.358 mol·kg^{-1} reported by Caravella et al. (2023). The adsorption enthalpies in this study (–44.7 to –34.5 kJ·mol^{-1}) are more negative than those in previous studies (e.g., –36.3 kJ·mol^{-1} in Streb & Mazzotti; –37.2 kJ·mol^{-1} in Cavenati; –22.017 kJ·mol^{-1} in Caravella), suggesting stronger interactions with CO_2, likely due to the binder-free morphology and optimized compacted structure.

These findings confirm that the physical form of zeolite significantly affects not only the total adsorption capacity but also the underlying adsorption mechanisms, which must be carefully considered in the design of industrial CO_2 capture processes.

3.2.3. Adsorption Equilibrium of N_2 and CH_4

Nitrogen (N_2) and methane (CH_4) exhibit distinct adsorption behaviors on zeolite 13X due to differences in their physicochemical characteristics. N_2, with a weak quadrupole moment and low polarizability, interacts only weakly with the polar surface of the zeolite, resulting in limited adsorption capacity. In contrast, CH_4, although lacking a permanent dipole or quadrupole moment, displays higher polarizability, enabling stronger van der Waals interactions with the adsorbent surface (Golipour et al., 2019). This difference translates into significantly higher uptake for CH_4 compared to N_2 under the same conditions.

The adsorption performance of nitrogen (N_2) and methane (CH_4) on zeolite 13X, in both binder-free (13X-BF) and powder (13X-P) forms, highlights the influence of adsorbate physicochemical properties and adsorbent structure. Experimental isotherms were recorded at 308 K, 328 K, and 348 K up to 350 kPa.

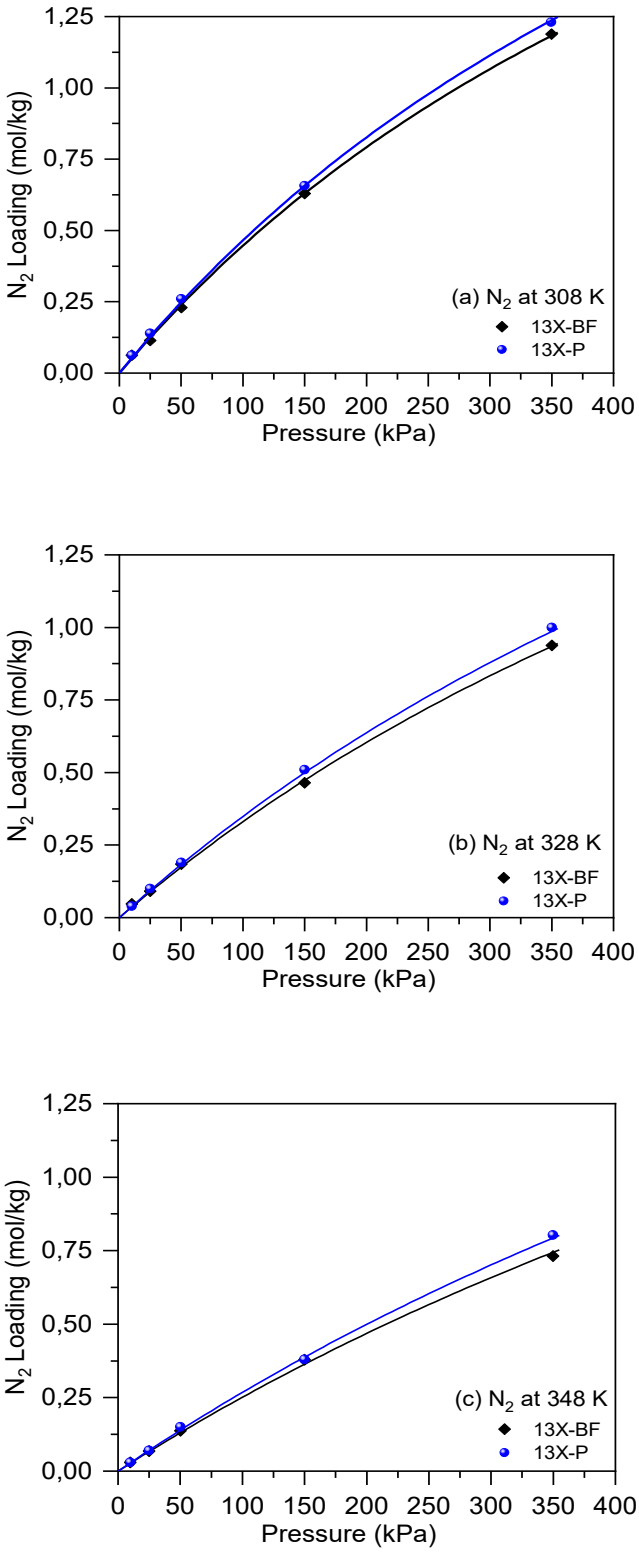

Figure 15. Comparison of N_2 adsorption isotherms at (a) 308, (b) 328, and (c) 348 K between binder-free 13X and powder-form 13X zeolites. Experimental = symbols; Numerical = lines.

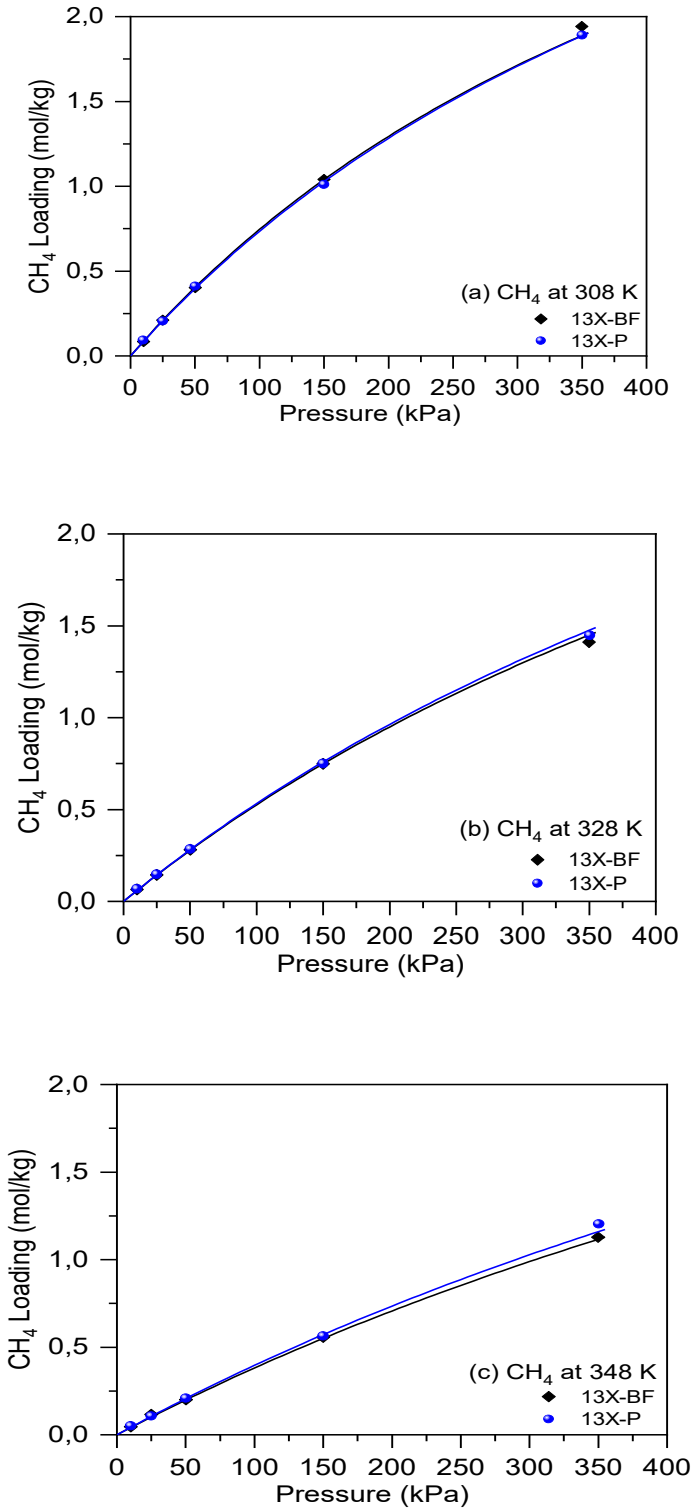

Figure 16. Comparison of CH_4 adsorption isotherms at (a) 308, (b) 328, and (c) 348 K between binder-free 13X and powder-form 13X zeolites. Experimental = symbols; Numerical = lines.

At all temperatures, the binder-free zeolite 13X consistently outperforms the powder form in terms of N_2 adsorption capacity in figure 15. This performance gap is particularly evident at intermediate and high pressures. For instance, at 308 K and 150 kPa, the adsorption capacity for the BF sample is 0.63 mol/kg, compared to 0.66 mol/kg in powder, a marginal difference of -4.5%. However, at 350 kPa, the BF form reaches 1.19 mol/kg, compared to 1.23 mol/kg for the powder, representing a smaller difference of -3.3%.

At lower pressures (e.g., 25 kPa), the BF zeolite shows similar or slightly higher uptake compared to the powder. This suggests that the enhanced microporosity and absence of binder in the BF material improve accessibility to adsorption sites, particularly at low partial pressures. Temperature effects follow the expected behavior for physisorption: as temperature increases, adsorption capacity decreases in both materials. At 348 K and 350 kPa, the BF sample reaches 0.73 mol/kg, while the powder reaches 0.80 mol/kg, showing a reduction of ~8.8% in the BF sample compared to the lower temperature.

In terms of performance with increasing temperature, the powder zeolite exhibits a drop of ~35% from 1.23 mol/kg (308 K) to 0.80 mol/kg (348 K), whereas the BF material drops ~38.6% (from 1.19 mol/kg to 0.73 mol/kg), highlighting comparable thermal sensitivity in both forms. These observations are clearly illustrated in Figure 16, which compares the adsorption isotherms of N_2 for both materials.

In contrast with N_2, methane adsorption shows almost identical behavior between powder and binder-free forms. Across all temperatures and pressures, the adsorption capacities remain closely aligned. At 308 K and 350 kPa, the powder form reaches 1.89 mol/kg, while the BF sample reaches 1.96 mol/kg an increase of only 3.7%. At lower pressures, such as 25 kPa, the BF form adsorbs 0.21 mol/kg, compared to 0.21 mol/kg in the powder indicating no difference. These results confirm that the presence or absence of binder does not significantly impact CH_4 uptake under the studied conditions.

However, at 348 K and 350 kPa, 13X-P outperformed 13X-BF (1.13 vs. 0.80 mmol/g), indicating better thermal stability and preserved accessibility in the powder form under elevated temperatures. The linear shape of the CH_4 isotherms at all temperatures suggests weak saturation

and a dominant role of London dispersion interactions. These findings are depicted in Figure 17, which presents the adsorption isotherms of CH_4 for both forms of zeolite 13X.

In summary, while both gases exhibit weak overall adsorption compared to CO_2, N_2 shows slightly more sensitivity to structural differences in the adsorbent, with the BF form performing modestly better at lower pressures. For CH_4, see in figure 16, the differences are negligible across the entire pressure and temperature range, demonstrating that its interaction is governed more by polarizability than by the electrostatic features of the adsorbent surface.

These results confirm that the performance enhancements observed for CO_2 in binder-free zeolites do not significantly extend to weakly adsorbed gases like CH_4 or N_2. Nonetheless, the binder-free structure may still be favorable in low-concentration separation or multi-component systems where competitive adsorption plays a role.

Table 11 presents the Langmuir parameters for CH_4 and N_2. For CH_4, the powder form had a slightly higher maximum capacity 3.67 mol·kg^{-1} compared to BF 3.47 mol·kg^{-1}. The affinity constants (b) were similar (0.00145 vs. 0.00148 kPa^{-1}), and the heats of adsorption were −13.6 and −14.2 kJ·mol^{-1}, respectively, indicating moderate interactions. For N_2, the maximum capacity was 5.05 mol·kg^{-1} for powder and 4.87 mol·kg^{-1} for BF. The BF form exhibited a slightly higher b (0.00181 vs. 0.00170 kPa^{-1}) and more negative the heats of adsorption (−16.8 vs. −15.4 kJ·mol^{-1}), suggesting stronger micropore interactions.

Table 11. Adsorption equilibrium model parameters for sorption of CH_4 and N_2 on powder and binder-free 13X zeolite.

	Species	q_m (mol·kg^{-1})	b (kPa^{-1})[a]	(ΔH_i) (kJ·mol^{-1})
13X-BF	CH_4	3.47	0.00148	-14.2
	N_2	4.87	0.00181	-16.8
13X-P	CH_4	3.67	0.00145	-13.6
	N_2	5.05	0.00170	-15.4

[a] The reference temperature used is 308 K.

When compared with literature, the q_m values for CH_4 (3.47–3.67 mol·kg^{-1}) are close to those of Streb & Mazzotti (2021) (4.473 mol·kg^{-1}), lower than Cavenati et al. (2004) (9.842 mol·kg^{-1}), and higher than Golipour et al. (2019) (1.109 mol·kg^{-1}). For N_2, the obtained values (4.87–5.05 mol·kg^{-1}) are higher than those of Khoramzadeh et al. (2019) (2.596–2.837 mol·kg^{-1}) and Golipour et al. (1.793 mol·kg^{-1}), but lower than Cavenati et al. (8.00 mol·kg^{-1}). The adsorption enthalpies (−13.6 to −16.8 kJ·mol^{-1}) are in line with Cavenati et al. (−14.2 and −14.9 kJ·mol^{-1}), and less negative than those from Golipour (−17.86 and −19.23 kJ·mol^{-1}) and Khoramzadeh (−19 kJ·mol^{-1}), indicating moderate interaction strength.

The experimental data demonstrate that CO_2 exhibits the highest adsorption capacity on zeolite 13X, followed by N_2 and CH_4. This hierarchy is attributed to the distinct nature of gas-zeolite interactions: CO_2 establishes strong electrostatic interactions with Na^+ exchange sites, while N_2, despite its weaker quadrupole moment, maintains a moderate affinity. CH_4, interacting primarily through London dispersion forces, presents the lowest affinity and adsorption capacity. Both 13X-BF and 13X-P materials consistently followed this adsorption trend. These interaction characteristics suggest a potential for enhanced CO_2/N_2 and CO_2/CH_4 selectivity, thereby improving the efficiency of CO_2 separation processes. Both of zeolites 13X as a promising candidate for CO_2 removal from combustion gas streams and for CO_2/CH_4 separation in biogas upgrading applications.

3.3. Equilibrium Selectivity and work capacity

3.3.1. Equilibrium Selectivity of CO_2/N_2 and CO_2/CH_4

Based on the experimental data for single-component adsorption, ideal selectivity calculations were performed for the CO_2/N_2 and CO_2/CH_4 mixtures using the two types of zeolite 13X: the binder-free form (13X-BF) and the powder form (13X-P) can be calculated with equation 5. The results are presented in Figures 17(a–c) and 18(a–c), as a function of pressure parcial (10–

350 kPa) at three temperatures: 308 K, 328 K, and 348 K. The Dual-Site Langmuir (DSL) model was employed to fit the data.

Across all tested conditions, CO_2/N_2 selectivity values were consistently higher than CO_2/CH_4, reflecting the stronger affinity of CO_2 compared to the non-polar N_2 molecule. This distinction is especially pronounced at low pressures, where the high initial uptake of CO_2 can be attributed to its larger quadrupole moment and stronger electrostatic interactions with the cations in the zeolite framework.

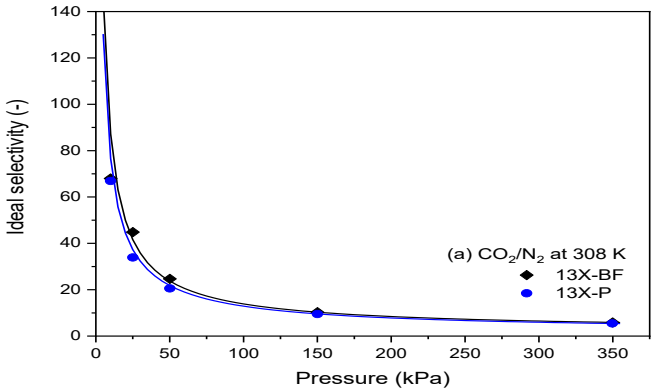

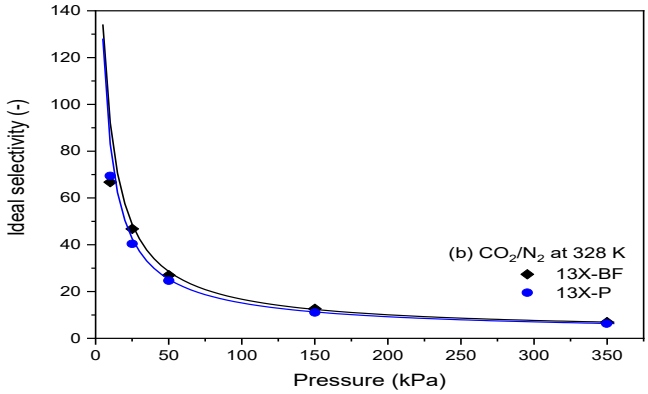

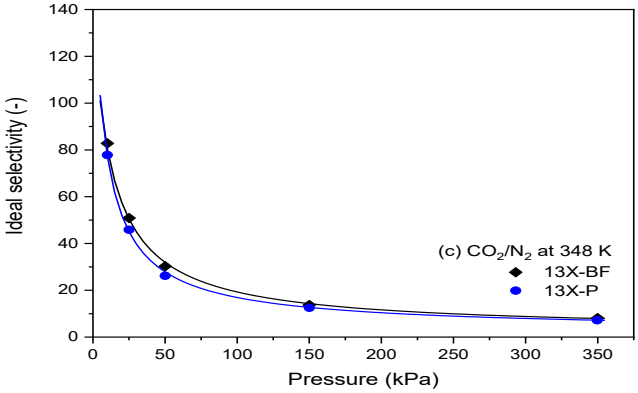

Figure 17. Ideal Selectivity of CO_2/N_2 at (a) 308, (b) 328, and (c) 348 K binder-free 13X and powder-form 13X zeolite. Experimental = symbols; DSL isotherm = lines.

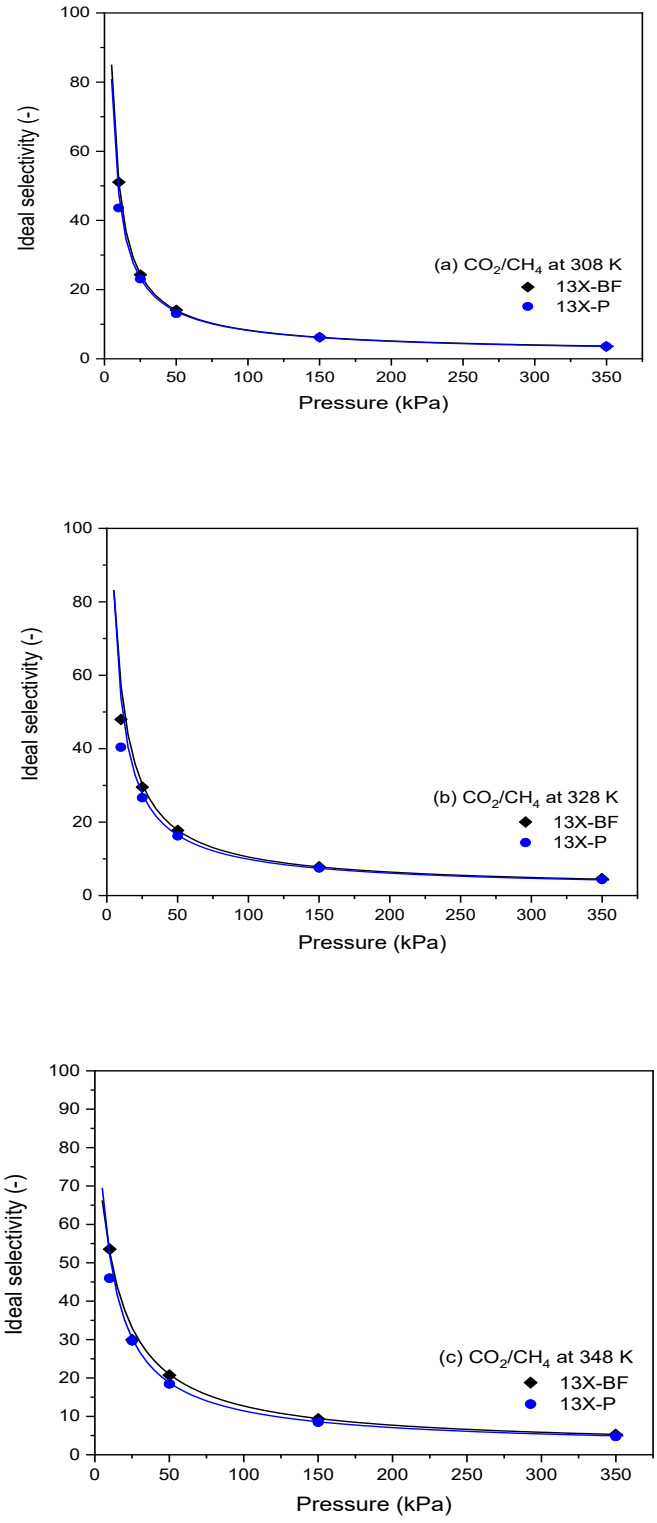

Figure 18. Ideal Selectivity of CO_2/CH_4 at (a) 308, (b) 328, and (c) 348 K binder-free 13X and powder-form 13X zeolite. Experimental = symbols; DSL isotherm = lines.

CO_2/N_2 Selectivity as shown in Figure 18, at 308 K and 25 kPa, 13X-BF exhibited a selectivity of 45, which is 32.3% higher than the 34 observed for 13X-P under the same conditions. This performance advantage is maintained throughout the pressure range of 25–50 kPa at all temperatures. For instance, at 348 K and 50 kPa, 13X-BF reached a selectivity of 30.3, which is 15.7% greater than the 26 measured for 13X-P.

At very low pressure (10 kPa), both materials showed similarly high values, exceeding 68 at 308 K and reaching approximately 83 for 13X-BF at 348 K. However, as pressure increased to 350 kPa, selectivity declined for both materials due to progressive saturation of adsorption sites. At 350 kPa and 328 K, 13X-BF recorded a selectivity of 6.94, slightly outperforming the 6.3 of 13X-P.

The CO_2/CH_4 selectivity, shown in Figure 19, followed similar trends but with overall lower values due to the closer adsorption affinities between CO_2 and CH_4. At 308 K and 25 kPa, 13X-BF showed a selectivity of 24, compared to 23.1 for 13X-P. At 328 K, 13X-BF achieved 30, which is 11.0% higher than the 27 measured for 13X-P. At 348 K and 50 kPa, 13X-BF maintained a selectivity of 21, outperforming 13X-P (18.4) by 12.5%.

At 10 kPa and 308 K, 13X-BF reached a selectivity of 51, which is 17.1% higher than the 44 observed for 13X-P. Similarly, at 348 K and 10 kPa, selectivity rose to 54 for 13X-BF compared to 46 for 13X-P. As with CO_2/N_2, selectivity in this system also dropped significantly with increasing pressure due to site saturation. At 350 kPa and 328 K, 13X-BF retained a selectivity of 4.6, while 13X-P recorded 4.4 under the same conditions.

In both separation scenarios, 13X-BF consistently least matched 13X-P, which represents pure compacted powder zeolite. This improved performance, particularly at low to moderate pressures, can be attributed to better accessibility of adsorption sites and enhanced pore connectivity in the binder-free structure.

Moreover, temperature effects suggest that selectivity tends to increase with temperature at low pressures, reflecting the exothermic nature of CO_2 adsorption. This leads to greater discrimination in favor of CO_2 when the overall adsorption capacity decreases. Such behavior is especially beneficial for post-combustion CO_2 capture (PCC), which typically operates at near-atmospheric pressures and moderate to high temperatures, where selective CO_2 uptake is essential.

3.3.2. Working Capacity

The working capacity refers to the usable amount of adsorbate that can be cyclically adsorbed and desorbed between the adsorption and regeneration stages. It is calculated by Eq. 6 as the difference between the amount of gas adsorbed under process conditions (e.g., high pressure or low temperature) and the residual amount retained after regeneration (e.g., low pressure or high temperature). This parameter is particularly relevant in cyclic processes such as Pressure Swing Adsorption (PSA) or Temperature Swing Adsorption (TSA), where the efficiency of the adsorbent is directly tied to its regeneration capacity (Pérez-Botella et al., 2022).

Binary Adsorption Experiments for CO_2/N_2 Mixture under typical PCC conditions

Experimental results (Table 12) show that the binder-free zeolite 13X-BF achieved a CO_2 uptake of 4.69 mol·kg^{-1}, outperforming the powder-based 13X-P, which reached 4.33 mol·kg^{-1}. This advantage was also reflected in CO_2/N_2 selectivity (15/85 mol%), with values of 70 for 13X-BF compared to 61 for 13X-P, indicating a higher affinity for CO_2 in 13X-BF.

Table 12. Comparison of adsorbent metrics between zeolites 13X-BF and 3X-P under PCC Conditions.

Flue Gas Conditions: CO_2/N_2 (15/85 mol%), 308 K, 101 kPa					
Zeolites	Binary CO_2 loading $q_{b_{CO2}}$ (mol ·kg $^{-1}$)	Binary CO_2/N_2 selectivity $\alpha_{b_{CO2/N2}}$ (−)	Working capacity β_1 (mol ·kg $^{-1}$)	Working capacity β_2 (mol ·kg $^{-1}$)	Working capacity β_3 (mol ·kg $^{-1}$)
13X-BF	<u>4.69</u>	<u>70</u>	<u>3.10</u>	1.79	1.45
13X-P	4.33	61.2	2.56	<u>1.98</u>	<u>1.65</u>

Conditions:

$\beta_1$ads: q (T1, P1) = q (308 K, 101 kPa). $\beta_1$des: q (T2, P2) = q (308 K, 3 kPa).

$\beta_2$ads: q (T1, P1) = q (308 K, 101 kPa). $\beta_2$des: q (T2, P2) = q (308 K, 10 kPa).

$\beta_3$ads: q (T1, P1) = q (308 K, 101 kPa). $\beta_3$des: q (T2, P2) = q (308 K, 15 kPa).

Working capacities were calculated for three regeneration scenarios (3, 10, and 15 kPa), simulating conditions typical of Vacuum Swing Adsorption (VSA) processes. At 3 kPa, 13X-BF showed a working capacity of 3.10 $mol \cdot kg^{-1}$, which is 21.1% higher than the 2.56 $mol \cdot kg^{-1}$ observed for 13X-P. However, this trend reverses at higher regeneration pressures: at 10 kPa, 13X-P outperforms 13X-BF by 9.6% (1.98 vs. 1.79 $mol \cdot kg^{-1}$), and at 15 kPa, by 12.1% (1.65 vs. 1.45 $mol \cdot kg^{-1}$).

This behavior suggests that 13X-BF performs better under deep vacuum conditions, likely due to its more accessible pore structure and absence of binder, which may enhance regeneration efficiency at low pressures. However, it appears more sensitive to regeneration pressure, while 13X-P demonstrates greater robustness under milder desorption conditions.

Overall, both kind of forms of zeolites kept comparable performance. Nevertheless, achieving extremely low desorption pressures (≤ 3 kPa) poses significant industrial challenges, especially due to the high energy demand associated with maintaining deep vacuum conditions in large-scale adsorption columns (Aly et al., 2024). This highlights the importance of balancing material performance with overall process energy efficiency.

In summary, binder-free 13X-BF offers superior performance under aggressive vacuum regeneration.

Adsorption Experiments for CO_2/CH_4 Mixture under typical biogas upgrading conditions.

To evaluate adsorbent performance under conditions representative of biogas upgrading, the working capacity was also calculated for binary mixtures CO_2/CH_4. This setup realistically simulates industrial biogas purification processes, where the main objective is the selective removal of CO_2 to obtain high-purity CH_4.

The results, summarized in Table 13, compare the performance of 13X-BF and 13X-P zeolites in terms of CO_2/CH_4 selectivity, and working capacity. In conventional Pressure Swing Adsorption (PSA) processes for biogas upgrading, the gas is typically compressed to pressures between 400 and 1000 kPa before entering the adsorption column, with desorption occurring at atmospheric

pressure (~101 kPa). Accordingly, the working capacity (β_4) was calculated as the difference in CO_2 uptake between 400 kPa and 101 kPa, reflecting an energy-efficient and cost-effective operational cycle (Magomnang et al., 2018).

Table 13. Comparison of adsorbent metrics between 13X-BF and 13X-P zeolites under biogas upgrading conditions.

Biogas Upgrading Conditions: CO_2/CH_4 (50/50 mol%), 308 K, 101 kPa

Zeolites	Binary CO_2 loading $q_{T_{CO2}}$ (mol ·kg $^{-1}$)	CO_2/CH_4 selectivity $\alpha_{CO2/CH4}$ (–)	Working capacity β_4 (mol ·kg $^{-1}$)
13X-BF	<u>5.33</u>	<u>20</u>	<u>0.84</u>
13X-P	5.29	18	0.74

Conditions:

$\beta_4$ads: q (T1, P1) = q (308 K, 400 kPa). $\beta_1$des: q (T2, P2) = q (308 K, 100 kPa).

According to Table 13, the binder-free 13X-BF exhibited a slightly higher binary CO_2 uptake (5.33 mol·kg^{-1}) than the powder-form 13X-P (5.29 mol·kg^{-1}). CO_2/CH_4 selectivity was also greater for 13X-BF (20 vs. 18), suggesting a stronger preferential interaction with CO_2 in competitive multicomponent environments. In terms of working capacity, 13X-BF achieved 0.84 mol·kg^{-1} approximately 13.5% higher than the 0.74 mol·kg^{-1} recorded for 13X-P indicating greater cyclic efficiency.

Together, these results demonstrate that both from of the zeolites exhibit balanced and effective performance in CH_4 purification via biogas upgrading. However, 13X-BF slightly outperformed 13X-P across all evaluated parameters, positioning it as a viable alternative to the compacted pure powder form.

Chapter 4
Conclusion and Future Work

4. Conclusion

This research systematically demonstrated that the binder-free Zeolite 13X (13X-BF) offers enhanced performance metrics, structural advantages, and superior suitability for industrial-scale CO_2 capture and biogas upgrading keeping overall similar results achieved in laboratory-agglomerated Zeolite 13X powder (13X-P) as synthesized as demonstrated through the adsorption equilibrium isotherms in both forms measured in this work. Adsorption capacities for both materials consistently followed the desired affinity order of $CO_2 > N_2 > CH_4$. Specifically, 13X-BF achieved a maximum CO_2 uptake of 7.57 mol·kg^{-1} at 308 K and 150 kPa, even surpassing the 7.11 mol.kg $^{-1}$ of the powder form. Furthermore, under post-combustion conditions CO_2/N_2 (15/85 mol%), 308 K, 101 kPa, 13X-BF confirmed its higher thermodynamic affinity for CO_2, yielding a CO_2/N_2 selectivity of 70 The similar results obtained in both forms prove the excellent properties of the material developed by CWK.

Also, the analysis of the working capacity (β) exposed a crucial kinetic and economic trade-off for cyclic adsorption processes. 13X-BF demonstrated a superior working capacity 3.10 mol.kg $^{-1}$ when regeneration was conducted under energy-intensive deep vacuum conditions (3 kPa), suggesting its structural accessibility is optimized for aggressive desorption. Conversely, the powder agglomerate (13X-P) showed a slightly better working capacity (1.98 mol.kg^{-1} vs. 1.79 mol.kg $^{-1}$) under milder, less energy-demanding vacuum regeneration (10 kPa and 15 kPa), which proved once more the superior performance of the binder-free beads. This material-dependent efficiency is complemented by a kinetic trade-off observed in dynamic breakthrough experiments: the 13X-BF spherical beads provided superior macroscopic benefits (higher bulk density, reduced axial dispersion) with only a marginally wider MTZ in some runs probably due to increased macropore intraparticle diffusion resistance in the compacted beads structure.

In summary, the binder-free Zeolite 13X successfully preserves the high intrinsic adsorption characteristics of the pure powder zeolite form while offering enhanced operational benefits and superior mechanical strength, confirming its high potential for large-scale application. 13X-BF is

certainly one of the recommended material for scale-up processes in PCC due to its inherent mechanical stability, higher selectivity, and superior performance under deep vacuum regeneration.

Future research should concentrate on deeper kinetic and dynamic breakthrough modeling studies. This includes the determination of kinetic parameters from the breakthrough curves using models like the Linear Driving Force (LDF) model. This detailed modeling is essential to accurately simulate the performance of 13X-BF in industrial-scale cyclic processes like PSA and VPSA, optimizing cycle times and column configurations to fully capitalize on its working capacity advantage.

Chapter 5
References

5. References

Abdullahi, T., Harun, Z., & Othman, M. H. D. (2017). A review on sustainable synthesis of zeolite from kaolinite resources via hydrothermal process. Advanced Powder Technology, 28(8), 1827–1840. https://doi.org/10.1016/j.apt.2017.04.028

Al Ezzi, A., & Ma, H. (2017). Equilibrium Adsorption Isotherm Mechanism of Water Vapor on Zeolites 3A, 4A, X, and Y. Volume 6: Energy. https://doi.org/10.1115/imece2017-72601

Aleksandrzak, T., Zabielska, K., & Gabruś, E. (2024). Modeling and experimental studies of carbon dioxide separation on zeolite fixed bed by cyclic pressure swing adsorption. Polish Journal of Chemical Technology, 26(1), 8–15. https://doi.org/10.2478/pjct-2024-0002

Aly, E., Zafanelli, L. F. A. S., Henrique, A., Gleichmann, K., Rodrigues, A. E., Da Silva Freitas, F. A., & Silva, J. A. C. (2024). Separation of CO_2/N_2 in Ion-Exchange binder-free beads of zeolite NaY for Post-Combustion CO_2 capture. Separation and Purification Technology, 348, 127722. https://doi.org/10.1016/j.seppur.2024.127722

Auerbach, S. M., Carrado, K. A., & Dutta, P. K. (2003). Handbook of zeolite science and technology. M. Dekker.

Avdiaj, S., Setina, J., & Erjavec, B. (2015). Volume Determination of Vacuum Vessels by Gas Expansion Method. MAPAN, 30(3), 175–178. https://doi.org/10.1007/s12647-015-0137-1

Bahamon, D., & Vega, L. F. (2016). Systematic evaluation of materials for post-combustion CO_2 capture in a Temperature Swing Adsorption process. Chemical Engineering Journal, 284, 438–447. https://doi.org/10.1016/j.cej.2015.08.098

Berg, F., Pasel, C., Eckardt, T., & Bathen, D. (2019). Temperature Swing Adsorption in Natural Gas Processing: A Concise Overview. ChemBioEng Reviews. https://doi.org/10.1002/cben.201900005

Braga, A. A. C., & Morgon, N. H. (2007). Descrições estruturais cristalinas de zeólitos. Química Nova, 30(1), 178–188. https://doi.org/10.1590/s0100-40422007000100030

Caravella, A., Prenesti, G., Luca, S. D., Turano, M., Testa, F., & Girimonte, R. (2023). Evaluation of CO2 Adsorption Parameters in Fluidised Zeolite 13X Beds Using Non-Linear Multivariate Optimisation. Separations, 10(11), 558–558. https://doi.org/10.3390/separations10110558

Cavenati, S., Grande, C. A., & Rodrigues, A. E. (2004). Adsorption Equilibrium of Methane, Carbon Dioxide, and Nitrogen on Zeolite 13X at High Pressures. Journal of Chemical & Engineering Data, 49(4), 1095–1101. https://doi.org/10.1021/je0498917

Charkhi, A., Kazemeini, M., Ahmadi, S. J., & Kazemian, H. (2012). Fabrication of granulated NaY zeolite nanoparticles using a new method and study the adsorption properties. Powder Technology, 231, 1–6. https://doi.org/10.1016/j.powtec.2012.06.041

Chen, S., Fu, Y., Huang, Y., & Tao, Z. (2016). Adsorption characteristics analysis of CO_2 and N_2 in 13X zeolites by molecular simulation and N2 adsorption experiment. Journal of Porous Materials, 23(3), 713–723. https://doi.org/10.1007/s10934-016-0126-y

Chue, K. T., Kim, J. N., Yoo, Y. J., Cho, S. H., & Yang, R. T. (1995). Comparison of Activated Carbon and Zeolite 13X for CO_2 Recovery from Flue Gas by Pressure Swing Adsorption. Industrial & Engineering Chemistry Research, 34(2), 591–598. https://doi.org/10.1021/ie00041a020

Cordova, S. S., Gustafsson, M., Eklund, M., & Svensson, N. (2023). What should we do with CO_2 from biogas upgrading?. Journal of CO_2 Utilization, 77, 102607–102607. https://doi.org/10.1016/j.jcou.2023.102607

D'Alessandro, Deanna M., Smit, B., & Long, Jeffrey R. (2010). Carbon Dioxide Capture: Prospects for New Materials. Angewandte Chemie International Edition, 49(35), 6058–6082. https://doi.org/10.1002/anie.201000431

Da Silva, F. A., Silva, J. A., & Rodrigues, A. E. (1999). A General Package for the Simulation of Cyclic Adsorption Processes. Adsorption, 5(3), 229–244. https://doi.org/10.1023/a:1008974908427

Darde, V., Thomsen, K., van Well, W. J. M., & Stenby, E. H. (2009). Chilled ammonia process for CO_2 capture. Energy Procedia, 1(1), 1035–1042. https://doi.org/10.1016/j.egypro.2009.01.137

David, E. (2015). Mechanical strength and reliability of the porous materials used as adsorbents/catalysts and the new development trends. Archives of Materials Science and Engineering. https://www.semanticscholar.org/paper/Mechanical-strength-and-reliability-of-the-porous-David/a749d3a6feee0eef85f6de1bc788e1e4b647c724

De Oliveira, J. C. A., Galdino, A. L., Gonçalves, D. V., Silvino, P. F. G., Cavalcante, C. L., Bastos-Neto, M., Azevedo, D. C. S., & Lucena, S. M. P. (2021). Representative Pores: An Efficient Method to Characterize Activated Carbons. Frontiers in Chemistry, 8. https://doi.org/10.3389/fchem.2020.595230

Di Gianfrancesco, A. (2017). 19 - Worldwide overview and trend for clean and efficient use of coal. ScienceDirect; Woodhead Publishing. https://www.sciencedirect.com/science/article/abs/pii/B9780081005521000191

Dirar, Q. H., & Loughlin, K. F. (2013). Intrinsic adsorption properties of CO_2 on 5A and 13X zeolite. Adsorption, 19(6), 1149–1163. https://doi.org/10.1007/s10450-013-9543-2

Do, D. D. (1998). Adsorption Analysis. ; Imperial College Press London SW7 2BT.

European Parliament. (2023). Climate change: the greenhouse gases causing global warming. European Parliament Climate and Environment. https://www.europarl.europa.eu/topics/en/article/20230316STO77629/climate-change-the-greenhouse-gases-causing-global-warming

Falkowska, M., Roebuck, L., & Bowron, D. (2025). Molecular insights into preferential N_2 adsorption on zeolite 13X via total neutron scattering. Adsorption, 31(5). https://doi.org/10.1007/s10450-025-00638-z

Fauziah, N. A., Kurniawan, T., & Irawan, A. (2024). Simulation of Pressure Swing Adsorption for Oxygen Concentrator Using LiX Zeolite. Applied Mechanics and Materials, 918, 195–203. https://doi.org/10.4028/p-w8r00m

Ferreira Falcão , G. (2005). CARACTERIZAÇÃO DE ZEÓLITA E SUA APLICAÇÃO COMO ADSORVENTE DE $(NH_4)_2SO_4$. Centro de Tecnologia Mineral - CETEM. http://mineralis.cetem.gov.br/handle/cetem/756

FERREIRA MELO, J. V. (n.d.). UM REATOR DE LEITO FIXO OPERADO EM BATELADA SEQUENCIAL NO TRATAMENTO DE EFLUENTE DE INDÚSTRIA FARMACÊUTICA . UFG - Universidade Federal de Goiás. https://eeca.ufg.br/p/23208-trabalhos-de-conclusao-de-curso-engenharia-ambiental-e-sanitaria-2017-2

Figueiredo, J. L., & Ribeiro, F. (1987). Catálise Heterogênea. https://fr.scribd.com/document/398341027/Figueiredo-Catalise-Heterogenea

Figueroa, J. D., Fout, T., Plasynski, S., McIlvried, H., & Srivastava, R. D. (2008). Advances in CO2 capture technology—The U.S. Department of Energy's Carbon Sequestration Program. International Journal of Greenhouse Gas Control, 2(1), 9–20. https://doi.org/10.1016/s1750-5836(07)00094-1

Foo, K. Y., & Hameed, B. H. (2010). Insights into the modeling of adsorption isotherm systems. Chemical Engineering Journal, 156(1), 2–10. https://doi.org/10.1016/j.cej.2009.09.013

Gao, S., Peng, H., Song, B., Zhang, J., Wu, W., Vaughan, J., Zardo, P., Vogrin, J., Tulloch, S., & Zhu, Z. (2023). Synthesis of zeolites from low-cost feeds and its sustainable environmental applications. Journal of Environmental Chemical Engineering, 11(1), 108995–108995. https://doi.org/10.1016/j.jece.2022.108995

Gibbins, J., & Chalmers, H. (2008). Carbon capture and storage. Energy Policy, 36(12), 4317–4322. https://doi.org/10.1016/j.enpol.2008.09.058

Girimonte, R., Brunello Formisani, & Testa, F. (2019). CO_2 adsorption in a confined fluidized bed of zeolite pellets: Influence of operating velocity. Particuology, 46, 67–74. https://doi.org/10.1016/j.partic.2018.08.004

Gleichmann, K., Unger, B., & Brandt, A. (2016). Industrial Zeolite Molecular Sieves. Zeolites - Useful Minerals. https://doi.org/10.5772/63442

Golipour, H., Mokhtarani, B., Mafi, M., Khadivi, M., & Godini, H. R. (2019). Systematic Measurements of CH_4 and CO_2 Adsorption Isotherms on Cation-Exchanged Zeolites 13X. Journal of Chemical & Engineering Data, 64(10), 4412–4423. https://doi.org/10.1021/acs.jced.9b00473

Goncalves, M. B., Schmidt, D. V. C., dos Santos, F. S., Cipriano, D. F., Gonçalves, G. R., Freitas, J. C. C., & de Pietre, M. K. (2020). Nanostructured faujasite zeolite as metal ion adsorbent: kinetics, equilibrium adsorption and metal recovery studies. Water Science and Technology, 83(2), 358–371. https://doi.org/10.2166/wst.2020.580

Gür, T. M. (2022). Carbon Dioxide Emissions, Capture, Storage and Utilization: Review of Materials, Processes and Technologies. Progress in Energy and Combustion Science, 89, 100965. https://doi.org/10.1016/j.pecs.2021.100965

Gutierrez-Ortega, A., Montes-Morán, M. A., Parra, J. B., Sempere, J., Nomen, R., & Gonzalez-Olmos, R. (2022). Comparative study of binderless zeolites and carbon molecular sieves as adsorbents for CO_2 capture processes. Journal of CO_2 Utilization, 61, 102012. https://doi.org/10.1016/j.jcou.2022.102012

Harben, P. W., & Miloš Kužvart. (1997). Industrial Minerals.

Harlick, P. J. E., & Tezel, F. H. (2003). Adsorption of carbon dioxide, methane and nitrogen: pure and binary mixture adsorption for ZSM-5 with $SiO_2/Al2O_3$ ratio of 280. Separation and Purification Technology, 33(2), 199–210. https://doi.org/10.1016/S1383-5866(02)00078-3

Harlick, P. J. E., & Tezel, F. H. (2004). An experimental adsorbent screening study for CO_2 removal from N_2. Microporous and Mesoporous Materials, 76(1-3), 71–79. https://doi.org/10.1016/j.micromeso.2004.07.035

Hedlund, J., Garcia, G., Balsamo, M., Zhou, M., & Mouzon, J. (2021). Microchannel zeolite 13X adsorbent with high CO_2 separation performance. Separation and Purification Technology, 277, 119483. https://doi.org/10.1016/j.seppur.2021.119483

Henrique, A. (2015a). Purificação do Biogás em Sólidos Porosos. Escola Superior de Tecnologia E Gestão Instituto Politécnico de Bragança.

Henrique, A. (2015b). Purificação do Biogás em Sólidos Porosos . Escola Superior de Tecnologia e Gestão Instituto Politécnico de Bragança) .

Henrotin, A., Heymans, N., Duprez, M. E., Mouchaham, G., Serre, C., Wong, D., Robinson, R., Mulrooney, D., J. Casaban, & G. De Weireld. (2024). Lab-scale pilot for CO_2 capture vacuum

pressure swing adsorption: MIL-160(Al) vs zeolite 13X. Carbon Capture Science & Technology, 12, 100224–100224. https://doi.org/10.1016/j.ccst.2024.100224

Heule, X. van, Paepe, M. D., & Lecompte, S. (2022). Two-Phase Volumetric Expanders: A Review of the State-of-the-Art. Energies, 15(14), 4991–4991. https://doi.org/10.3390/en15144991

Ho, M. T., Allinson, G. W., & Wiley, D. E. (2008). Reducing the Cost of CO_2Capture from Flue Gases Using Pressure Swing Adsorption. Industrial & Engineering Chemistry Research, 47(14), 4883–4890. https://doi.org/10.1021/ie070831e

IPCC. (2023). Climate Change 2023: Synthesis Report. Contribution of Working Groups I, II and III to the Sixth Assessment Report of the Intergovernmental Panel on Climate Change [Core Writing Team, H. Lee and J. Romero (eds.)]. IPCC, Geneva, Switzerland. Climate Change 2023 Synthesis Report, 186, 35–115. https://doi.org/10.59327/ipcc/ar6-9789291691647

Jedli, H., Bouzgarrou, S. M., Hassani, R., Sabi, E., & Slimi, K. (2024). Adsorption of CO_2, CH_4 and H_2 onto zeolite 13 X: Kinetic and equilibrium studies. Heliyon, 10(23), e40672. https://doi.org/10.1016/j.heliyon.2024.e40672

Kadam, R., & Panwar, N. L. (2017). Recent advancement in biogas enrichment and its applications. Renewable and Sustainable Energy Reviews, 73, 892–903. https://doi.org/10.1016/j.rser.2017.01.167

Khnifira, M., Mahsoune, A., E. Belghiti, M., Khamar, L., Sadiq, M., Abdennouri, M., & Barka, N. (2021). Combined DFT and MD simulation approach for the study of SO_2 and CO_2 adsorption on graphite (111) surface in aqueous medium. Current Research in Green and Sustainable Chemistry, 4, 100085–100085. https://doi.org/10.1016/j.crgsc.2021.100085

Khoramzadeh, E., Mofarahi, M., & Lee, C.-H. (2019). Equilibrium Adsorption Study of CO_2 and N_2 on Synthesized Zeolites 13X, 4A, 5A, and Beta. Journal of Chemical & Engineering Data, 64(12), 5648–5664. https://doi.org/10.1021/acs.jced.9b00690

Kumar, S., Srivastava, R., & Koh, J. (2020). Utilization of zeolites as CO_2 capturing agents: Advances and future perspectives. Journal of CO_2 Utilization, 41, 101251. https://doi.org/10.1016/j.jcou.2020.101251

Leung, D. Y. C., Caramanna, G., & Maroto-Valer, M. M. (2014). An overview of current status of carbon dioxide capture and storage technologies. Renewable and Sustainable Energy Reviews, 39, 426–443. https://doi.org/10.1016/j.rser.2014.07.093

Liang, D., Hu, Y., Bao, Q., Zhang, J., Feng, J., Sun, P., Ma, Y., & Zhang, H. (2021). A suitable zeolite Rho for separating CO_2/CH_4 in pressure swing adsorption (PSA) process. Inorganic Chemistry Communications, 127, 108547. https://doi.org/10.1016/j.inoche.2021.108547

Lins, T., Rodrigues, A. E., & Regina. (2012). Separation of Carbon Dioxide from Flue Gas Using Adsorption on Porous Solids. ResearchGate, 57–80. https://doi.org/10.13140/2.1.2092.6404

Liu, K., Yin, Z., Luo, R., Qiu, B., Chen, Y., Yang, C., Luo, Y., Hong, Z., & Xue, M. (2023). Durable Co(OH)2/stearic acid-based superhydrophobic/superoleophilic nanocellulose membrane for highly efficient oil/water separation and simultaneous removal of soluble dye. Industrial Crops and Products, 203, 117190. https://doi.org/10.1016/j.indcrop.2023.117190

Lorenzo, R., Sanchez, D. L., Realmonte, G., Baldocchi, D., & D'Odorico, P. (2021). The Water Footprint of Carbon Capture and Storage Technologies. Renewable and Sustainable Energy Reviews, 138, 110511. https://doi.org/10.1016/j.rser.2020.110511

Luna, F. J., & Schuchardt, U. (2001). Modificação de zeólitas para uso em catálise. Química Nova, 24(6), 885–892. https://doi.org/10.1590/s0100-40422001000600027

Luz, A. B. (1995). Zeólitas: propriedades e usos industriais. http://mineralis.cetem.gov.br/bitstream/cetem/132/1/stm-68

Magalhães Ferreira, P. (n.d.). ALTERAÇÕES CLIMÁTICAS E DESENVOLVIMENTO (FEC | Fundação Fé e Cooperação, Vol. 154). Plataformaongd.pt. https://www.plataformaongd.pt/uploads/subcanais2/estudoalteracoesclimaticas-coerencia

Magomnang, A. A. S. M., Jr, A. L. M., & Villanueva, S. C. C. and E. P. (2018). Evaluating the System Performance of a Pressure Swing Adsorption (PSA) Unit by Removing the Carbon Dioxide

from Biogas. Indian Journal of Science and Technology, 11(17), 1–17. https://doi.org/10.17485/ijst/2018/v11i17/120992

MAT, M. (2023, November 7). Zeólitas: Minerais, Propriedades, Ocorrência, Usos»Ciência Geológica. Geology Science. https://pt.geologyscience.com/minerais/ze%C3%B3lito/#google_vignette

Mccabe, W. L. (1993). Unit operations of chemical engineering (J. C. Smith & P. Harriott, Eds.; 5th ed.). Mcgraw-Hill.

Meng, Y., Ju, T., Han, S., Gao, Y., Liu, J., & Jiang, J. (2020). Exploring the stability on exposure to acid impurities of polyethyleneimine-functionalized silica for post-combustion CO2 capture. Chemical Engineering Journal, 127754. https://doi.org/10.1016/j.cej.2020.127754

Metz, B., Davidson, O., Coninck, H., Loos, M., & Meyer, L. (2005). Carbon Dioxide Capture and Storage — IPCC. https://www.ipcc.ch/report/carbon-dioxide-capture-and-storage/

Meynen, V., Cool, P., & Vansant, E. F. (2009). Verified syntheses of mesoporous materials. Microporous and Mesoporous Materials, 125(3), 170–223. https://doi.org/10.1016/j.micromeso.2009.03.046

Mondragon, F., Rincon, F., Sierra, L., Escobar, J., Ramirez, J., & Fernandez, J. (1990). New perspectives for coal ash utilization: synthesis of zeolitic materials. Fuel, 69(2), 263–266. https://doi.org/10.1016/0016-2361(90)90187-u

Mosca, A. (2009). Structured Zeolite Adsorbents for PSA Applications. https://www.diva-portal.org/smash/get/diva2:999566/FULLTEXT01

Mulgundmath, V. P., Tezel, F. H., Saatcioglu, T., & Golden, T. C. (2011). Adsorption and separation of CO_2/N_2 and CO_2/CH_4 by 13X zeolite. The Canadian Journal of Chemical Engineering, 90(3), 730–738. https://doi.org/10.1002/cjce.20592

Najafi, A. M., Soltanali, S., Khorashe, F., & Ghassabzadeh, H. (2023). Effect of binder on CO_2, CH_4, and N_2 adsorption behavior, structural properties, and diffusion coefficients on extruded zeolite 13X. 324, 138275–138275. https://doi.org/10.1016/j.chemosphere.2023.138275

Nanda, S., Reddy, S. N., Mitra, S. K., & Kozinski, J. A. (2016). The progressive routes for carbon capture and sequestration. Energy Science & Engineering, 4(2), 99–122. https://doi.org/10.1002/ese3.117

Nascimento , R. F. do, Lima, A. C. A. de, Vidal, C. B., de Quadros Melo, D., & Cabral Raulino, G. S. (2014). Adsorção aspectos teoricos e ambientais. Academia.edu. https://doi.org/1017723/71491743/59937338/s200_r_gis

Neves, C. de F. C., & Schvartzman, M. M. de A. M. (2005). Separação de CO_2 por meio da tecnologia PSA. Química Nova, 28(4), 622–628. https://doi.org/10.1590/s0100-40422005000400013

Orsikowsky-Sanchez, A., Franke, C., Sachse, A., Ferrage, E., Petit, S., Brunet, J., Plantier, F., & Miqueu, C. (2021). Gas Porosimetry by Gas Adsorption as an Efficient Tool for the Assessment of the Shaping Effect in Commercial Zeolites. Nanomaterials, 11(5), 1205. https://doi.org/10.3390/nano11051205

Park, S., Lee, E. S., & Sulaiman, W. R. W. (2015). Adsorption behaviors of surfactants for chemical flooding in enhanced oil recovery. Journal of Industrial and Engineering Chemistry, 21, 1239–1245. https://doi.org/10.1016/j.jiec.2014.05.040

Park, Y., Ju, Y., Park, D., & Chang Ha Lee. (2016). Adsorption equilibria and kinetics of six pure gases on pelletized zeolite 13X up to 1.0 MPa: CO_2 , CO, N_2 , CH_4 , Ar and H_2. Chemical Engineering Journal, 292, 348–365. https://doi.org/10.1016/j.cej.2016.02.046

Pavlov, M. L., Travkina, O. S., & Kutepov, B. I. (2012). Grained binder-free zeolites: Synthesis and properties. Catalysis in Industry, 4(1), 11–18. https://doi.org/10.1134/s2070050412010096

Pera-Titus, M. (2013). Porous Inorganic Membranes for CO2 Capture: Present and Prospects. Chemical Reviews, 114(2), 1413–1492. https://doi.org/10.1021/cr400237k

Pérez-Botella, E., Valencia, S., & Rey, F. (2022). Zeolites in Adsorption Processes: State of the Art and Future Prospects. Chemical Reviews, 122(24), 17647–17695. https://doi.org/10.1021/acs.chemrev.2c00140

Pinault, J.-L. (2018). Anthropogenic and Natural Radiative Forcing: Positive Feedbacks. Journal of Marine Science and Engineering, 6(4), 146. https://doi.org/10.3390/jmse6040146

Pires, J. C. M., Martins, F. G., Alvim-Ferraz, M. C. M., & Simões, M. (2011). Recent developments on carbon capture and storage: An overview. Chemical Engineering Research and Design, 89(9), 1446–1460. https://doi.org/10.1016/j.cherd.2011.01.028

Plasynski, S. I., Litynski, J. T., McIlvried, H. G., & Srivastava, R. D. (2009). Progress and New Developments in Carbon Capture and Storage. Critical Reviews in Plant Sciences, 28(3), 123–138. https://doi.org/10.1080/07352680902776440

Powroznik, K. D., & Alonso, M. C. (2018). Natural and synthetic zeolites. Synthesis of zeolite X. https://rucforsk.ruc.dk/ws/portalfiles/portal/63722849/NIB_2018__5th_semester_project__1_

Raganati, F., Miccio, F., & Ammendola, P. (2021). Adsorption of Carbon Dioxide for Post-combustion Capture: A Review. Energy & Fuels, 35(16), 12845–12868. https://doi.org/10.1021/acs.energyfuels.1c01618

Rao, A. B., & Rubin, E. S. (2002). A Technical, Economic, and Environmental Assessment of Amine-Based CO_2 Capture Technology for Power Plant Greenhouse Gas Control. Environmental Science & Technology, 36(20), 4467–4475. https://doi.org/10.1021/es0158861

Rezaei, S., Liu, A., & Hovington, P. (2023). Emerging technologies in post-combustion carbon dioxide capture & removal. Catalysis Today, 423, 114286. https://doi.org/10.1016/j.cattod.2023.114286

Rouquerol, J., Rouquerol, F., Sing, K. S. W., Llewellyn, P. L., & Maurin, G. (2014). Adsorption by powders and porous solids : principles, methodology and applications. Elsevier/Ap.

Ruthven, D. M. (1984). Principles of adsorption and adsorption processes. Wiley.

S, K. K. (1995). For your next separation consider adsorption. Chemical Engineering, 102(11). http://www.osti.gov/scitech/biblio/131740-your-next-separation-consider-adsorption

Samanta, A., Zhao, A., Shimizu, G. K. H., Sarkar, P., & Gupta, R. (2011). Post-Combustion CO_2 Capture Using Solid Sorbents: A Review. Industrial & Engineering Chemistry Research, 51(4), 1438–1463. https://doi.org/10.1021/ie200686q

Saraiva, B., Paula, A., Costa, D. S., Silva, W. B., Rodrigues, E. C., & Estumano, D. C. (2024). Parameter Estimation of Breakthrough Curve Models in the Adsorption Process of H2S and CO2 Using the Markov Chain Monte Carlo Method. Applied Sciences, 14(16), 6956–6956. https://doi.org/10.3390/app14166956

Sayari, A., Belmabkhout, Y., & Serna-Guerrero, R. (2011). Flue gas treatment via CO_2 adsorption. Chemical Engineering Journal, 171(3), 760–774. https://doi.org/10.1016/j.cej.2011.02.007

Schumann, K., Unger, B., Brandt, A., & Scheffler, F. (2011). Investigation on the pore structure of binderless zeolite 13× shapes. Microporous and Mesoporous Materials, 154, 119–123. https://doi.org/10.1016/j.micromeso.2011.07.015

Seader, J. D., & Henley, E. J. (2001). Separation process principles. Wiley India.

Selim, M. M., Tounsi, A., Gomaa, H., & Shenashen, M. (2024). Enhancing carbon capture efficiency in biogas upgrading: A comprehensive review on adsorbents and adsorption isotherms. AIP Advances, 14(4). https://doi.org/10.1063/5.0208686

Shafeeyan, M. S., Wan Daud, W. M. A., & Shamiri, A. (2014). A review of mathematical modeling of fixed-bed columns for carbon dioxide adsorption. Chemical Engineering Research and Design, 92(5), 961–988. https://doi.org/10.1016/j.cherd.2013.08.018

Sherman, J. D., & Yon, C. M. (2000). Adsorption, Gas Separation. Kirk-Othmer Encyclopedia of Chemical Technology. https://doi.org/10.1002/0471238961.0104191519080518.a01

Silva, J. A. C., & Rodrigues, A. (2014). Biogas upgrading and CO_2 capture by adsorption technologie. Proceedings of the Energy and Environment Knowledge .

Silva, J. A. C., Schumann, K., & Rodrigues, A. E. (2012). Sorption and kinetics of CO_2 and CH_4 in binderless beads of 13X zeolite. Microporous and Mesoporous Materials, 158, 219–228. https://doi.org/10.1016/j.micromeso.2012.03.042

Sir Nicholas Stern. (2016, June 3). Sobre as alterações climáticas — Agência Europeia do Ambiente. Www.eea.europa.eu. https://www.eea.europa.eu/pt/themes/climate/about-climate-change

Song, C., Liu, Q., Deng, S., Li, H., & Kitamura, Y. (2019). Cryogenic-based CO_2 capture technologies: State-of-the-art developments and current challenges. Renewable and Sustainable Energy Reviews, 101, 265–278. https://doi.org/10.1016/j.rser.2018.11.018

Song, C., Liu, Q., Ji, N., Deng, S., Zhao, J., Li, Y., Song, Y., & Li, H. (2018). Alternative pathways for efficient CO_2 capture by hybrid processes—A review. Renewable and Sustainable Energy Reviews, 82, 215–231. https://doi.org/10.1016/j.rser.2017.09.040

Songolzadeh, M., Ravanchi, M. T., & Soleimani, M. (2012). Carbon Dioxide Capture and Storage: A General Review on Adsorbents. International Journal of Chemical and Molecular Engineering, 6(10), 906–913.

Souza Pinto, J., Daniel, C., Carlos, J., Zambiasi, M., Tadeu, M., Ferreira, L., & Junior, A. (2018). Eficiência da Terra de Diatomácea e Zeólita para Controle de Sitophilus zeamais em Grãos de Trigo Armazenados .

Streb, A., & Mazzotti, M. (2021). Adsorption for efficient low carbon hydrogen production: part 1—adsorption equilibrium and breakthrough studies for $H_2/CO_2/CH_4$ on zeolite 13X. Adsorption, 27(4), 541–558. https://doi.org/10.1007/s10450-021-00306-y

Subraveti, S. G., Pai, K. N., Rajagopalan, A. K., Wilkins, N. S., Rajendran, A., Jayaraman, A., & Alptekin, G. (2019). Cycle design and optimization of pressure swing adsorption cycles for pre-combustion CO_2 capture. Applied Energy, 254, 113624. https://doi.org/10.1016/j.apenergy.2019.113624

Tao, Z., Tian, Y., Wu, W., Liu, Z., Fu, W., Kung, C.-W., & Shang, J. (2024). Development of zeolite adsorbents for CO_2 separation in achieving carbon neutrality. Npj Materials Sustainability, 2(1). https://doi.org/10.1038/s44296-024-00023-x

Tazikeh, S., Shafiei, A., Yerkenov, T., Abenov, A., Seitmaganbetov, N., & Atabaev, T. Sh. (2022). A systematic and critical review of asphaltene adsorption from macroscopic to microscopic scale: Theoretical, experimental, statistical, intelligent, and molecular dynamics simulation approaches. Fuel, 329, 125379–125379. https://doi.org/10.1016/j.fuel.2022.125379

Thommes, M., Kaneko, K., Neimark, A. V., Olivier, J. P., Rodriguez-Reinoso, F., Rouquerol, J., & Sing, K. S. W. (2015). Physisorption of gases, with special reference to the evaluation of surface area and pore size distribution (IUPAC Technical Report). Pure and Applied Chemistry, 87(9-10), 1051–1069. https://doi.org/10.1515/pac-2014-1117

Vizcarra Valencia, C. A. (2007). Aplicação da Adsorção em Carvão Ativado e outros Materiais Carbonosos no Tratamento de Águas Contaminadas por Pesticidas de Uso Agrícola. Puc-Rio.br. https://www.maxwell.vrac.puc-rio.br/10607/10607_1

W. Hölderich, Karge, H. G., Weitkamp, J., & Pfeifer, H. (1994). Zeolites and Related Microporous Materials: State of the Art 1994. Elsevier.

Wang, J., Mangano, E., & Brandani, S. (2019). Diffusion measurements using a volumetric differential pressure apparatus. Diffusion-Fundamentals.

Wang, J., Wei, Y., & Ma, Z. (2020). Modified Dual-Site Langmuir Adsorption Equilibrium Models from A GCMC Molecular Simulation. Applied Sciences, 10(4), 1311–1311. https://doi.org/10.3390/app10041311

WEBER, W. J., & LIU, K. T. (1980). DETERMINATION OF MASS TRANSPORT PARAMETERS FOR FIXED-BED ADSORBERS. Chemical Engineering Communications, 6(1-3), 49–60. https://doi.org/10.1080/00986448008912520

Yadav, A., Shukla, S. K., Tirkey, J. V., & Pathak, S. (2018). Sustainable Biofuels for Automotive Applications. Elsevier EBooks, 809–838. https://doi.org/10.1016/b978-0-12-803581-8.11115-4

Yang, R. T. (2013). Gas Separation by Adsorption Processes. Butterworth-Heinemann.

Ye, W., Pan, Y., He, L., Chen, B., Liu, J., Gao, J., Wang, Y., & Yang, Y. (2021). Chapter 3 - Design with modeling techniques (H. D. Goodfellow & Y. Wang, Eds.). ScienceDirect; Academic Press. https://www.sciencedirect.com/science/article/abs/pii/B9780128166734000080

YONG, Z., MATA, V., & RODRIGUES, A. (2002). Adsorption of carbon dioxide at high temperature—a review. Separation and Purification Technology, 26(2-3), 195–205. https://doi.org/10.1016/s1383-5866(01)00165-4

Yuan, Z., Eden, M. R., & Gani, R. (2015). Toward the Development and Deployment of Large-Scale Carbon Dioxide Capture and Conversion Processes. Industrial & Engineering Chemistry Research, 55(12), 3383–3419. https://doi.org/10.1021/acs.iecr.5b03277

Zhou, X., Yi, H., Tang, X., Deng, H., & Liu, H. (2012). Thermodynamics for the adsorption of SO2, NO and CO2 from flue gas on activated carbon fiber. 200-202, 399–404. https://doi.org/10.1016/j.cej.2012.06.013

Chapter 6
Appendix

6. Appendix

The following figures show the real time breakthrough curves performed along this work to calculate the loadings shown by the isotherms in Figures 1 to 6 on both forms of 13X-BF and 13X-P

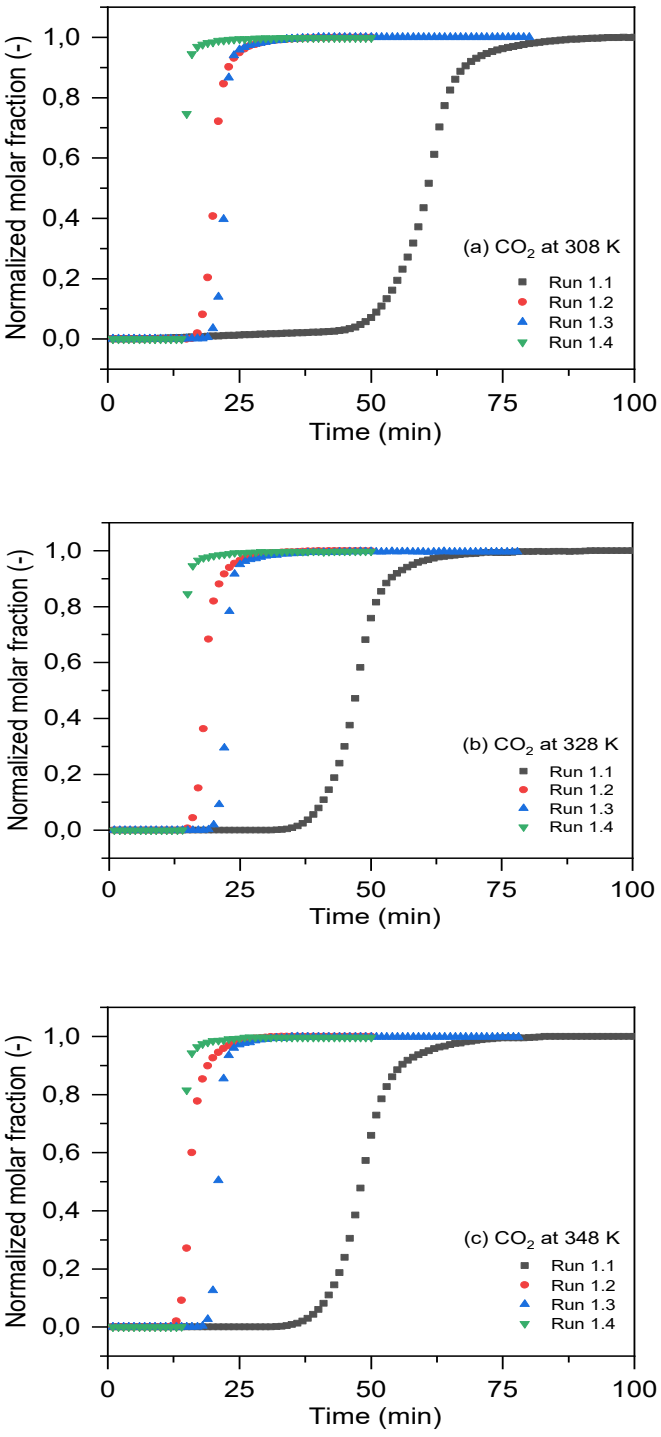

Figure 1. Real time breakthrough Curves of CO_2 on binder-free zeolite 13X at 308 K,328 K and 348 K.

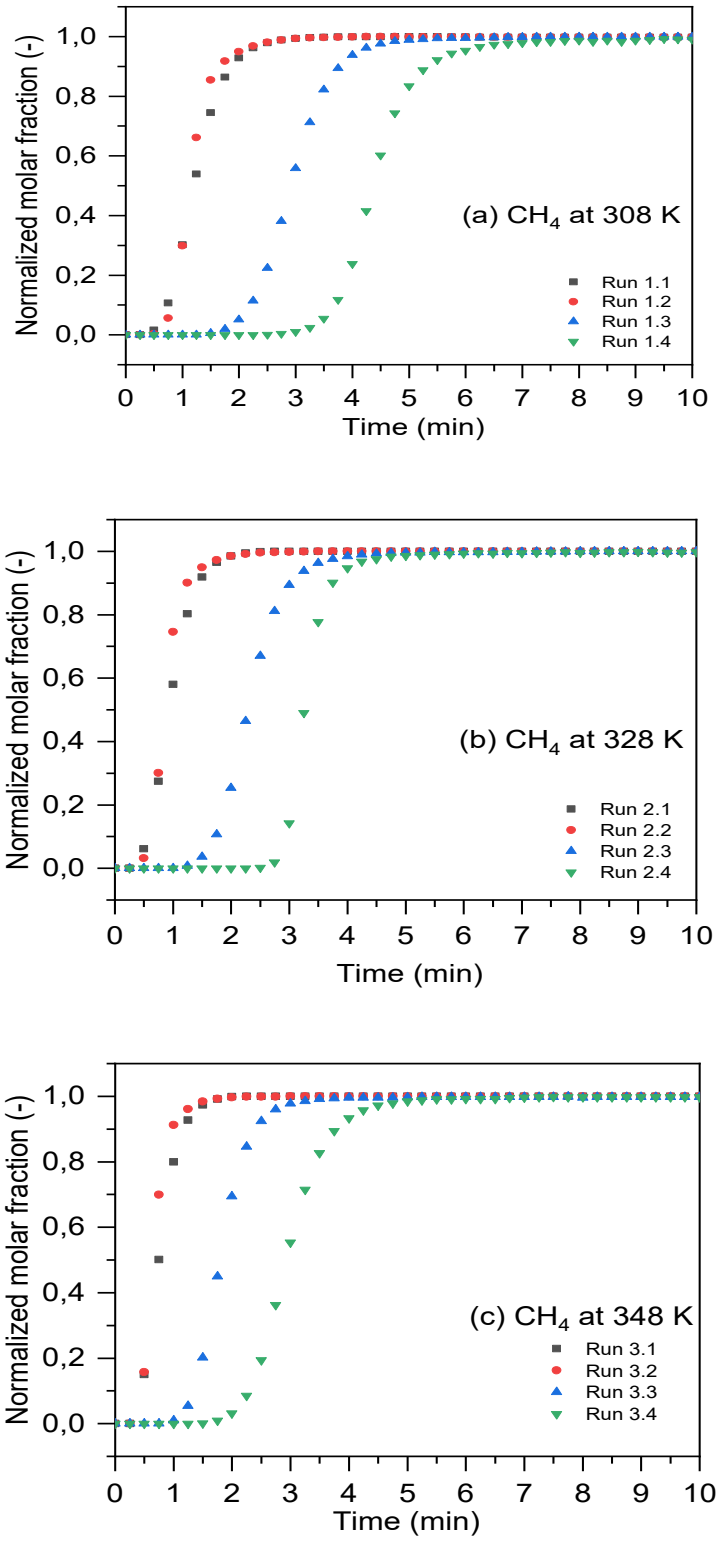

Figure 2. Real time breakthrough Curves of CH_4 on binder-free zeolite 13X at 308 K,328 K and 348 K.

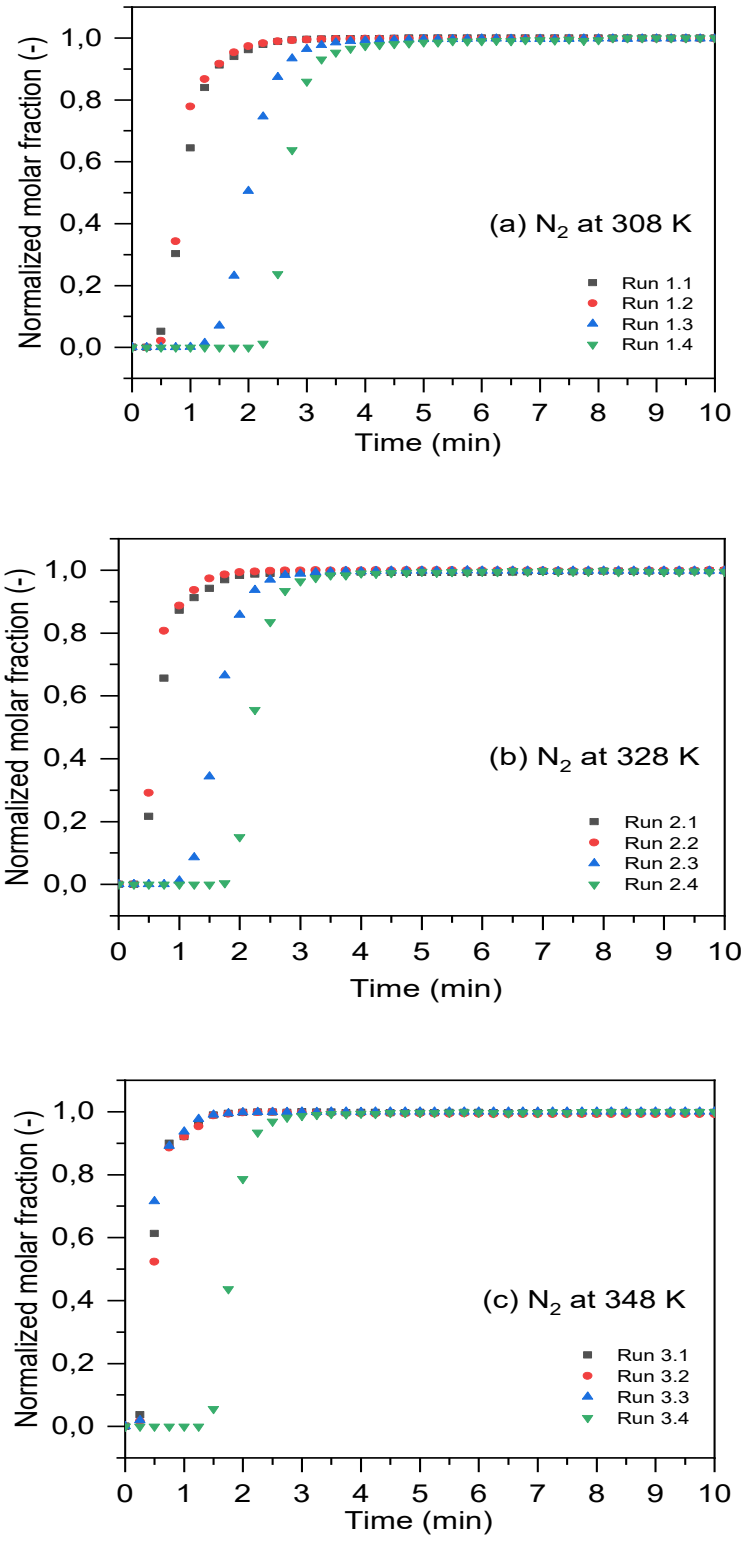

Figure 3. Real time breakthrough Curves of N_2 on binder-free zeolite 13X at 308 K,328 K and 348 K.

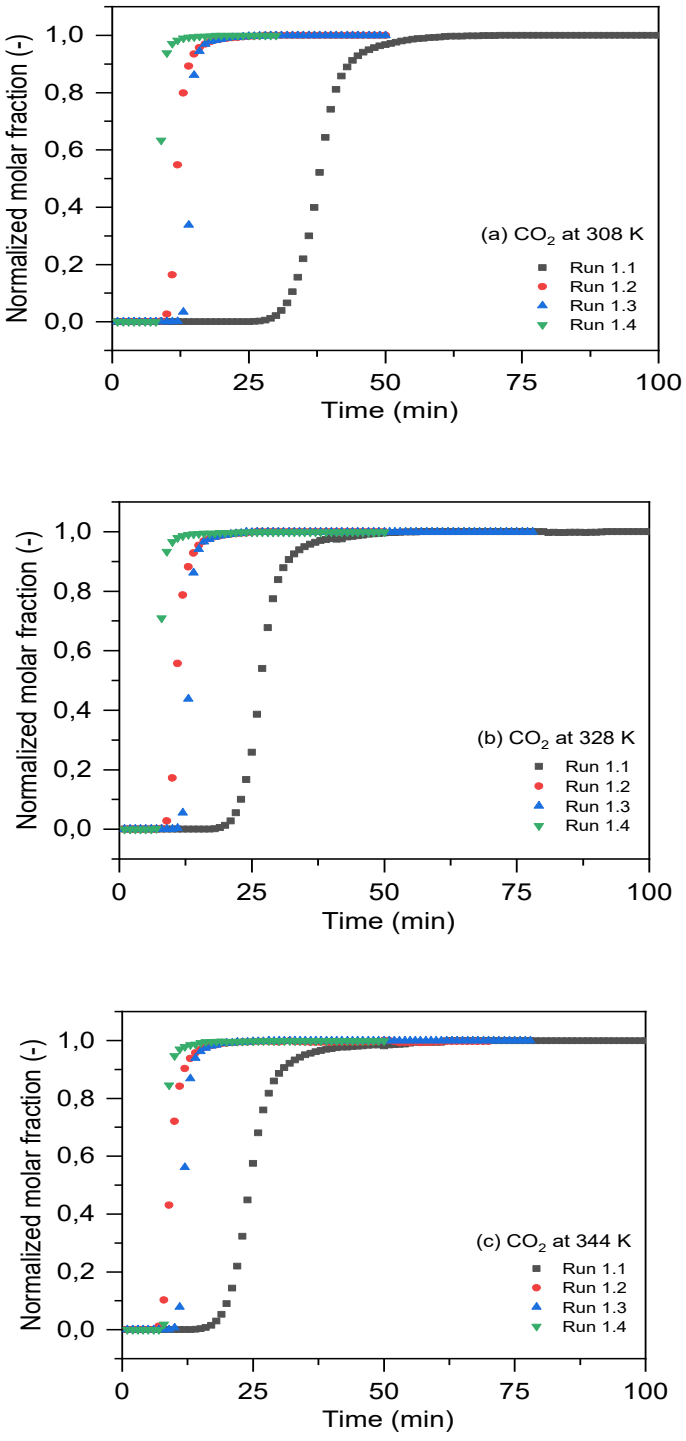

Figure 4. Real time breakthrough Curves of CO_2 for powder-from 13X zeolite at 308 K,328 K and 348 K.

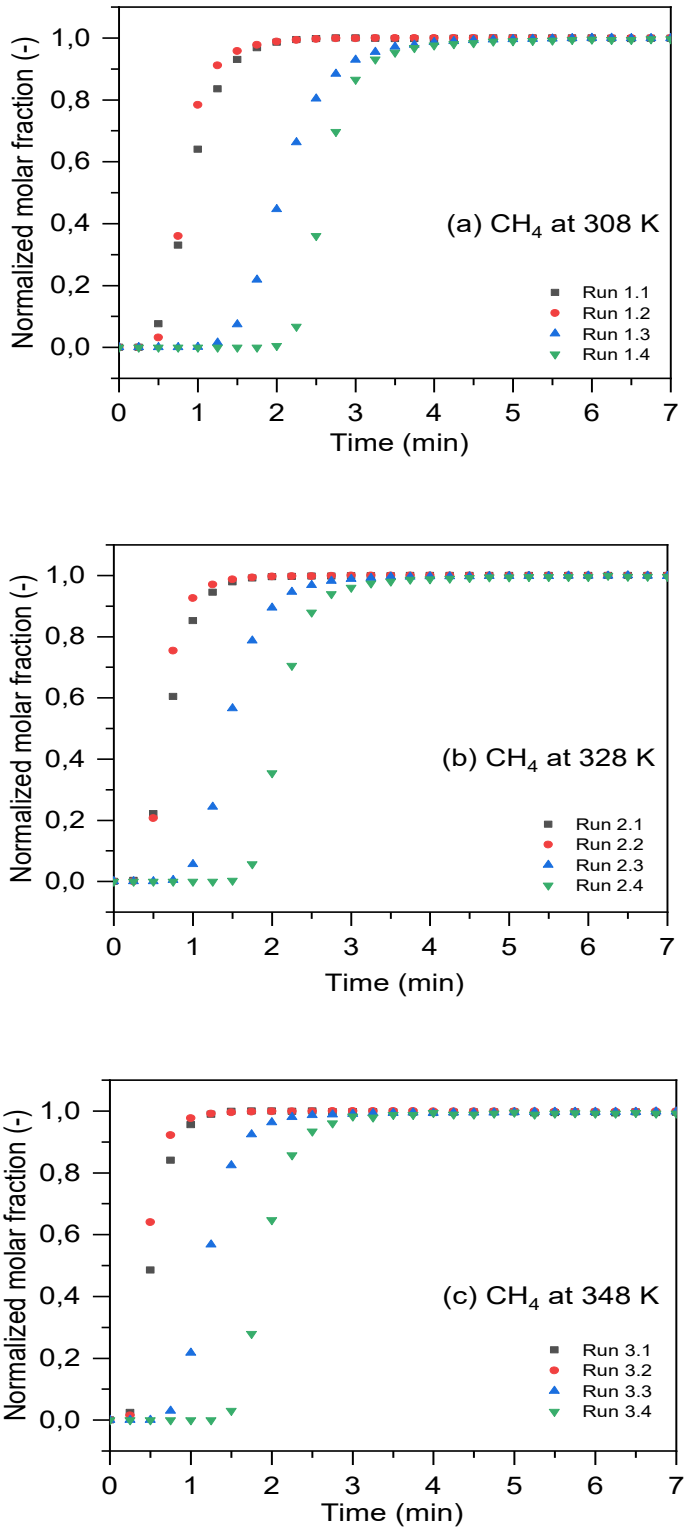

Figure 5. Real time breakthrough Curves of CH_4 for powder-from 13X zeolite at 308 K,328 K and 348 K.

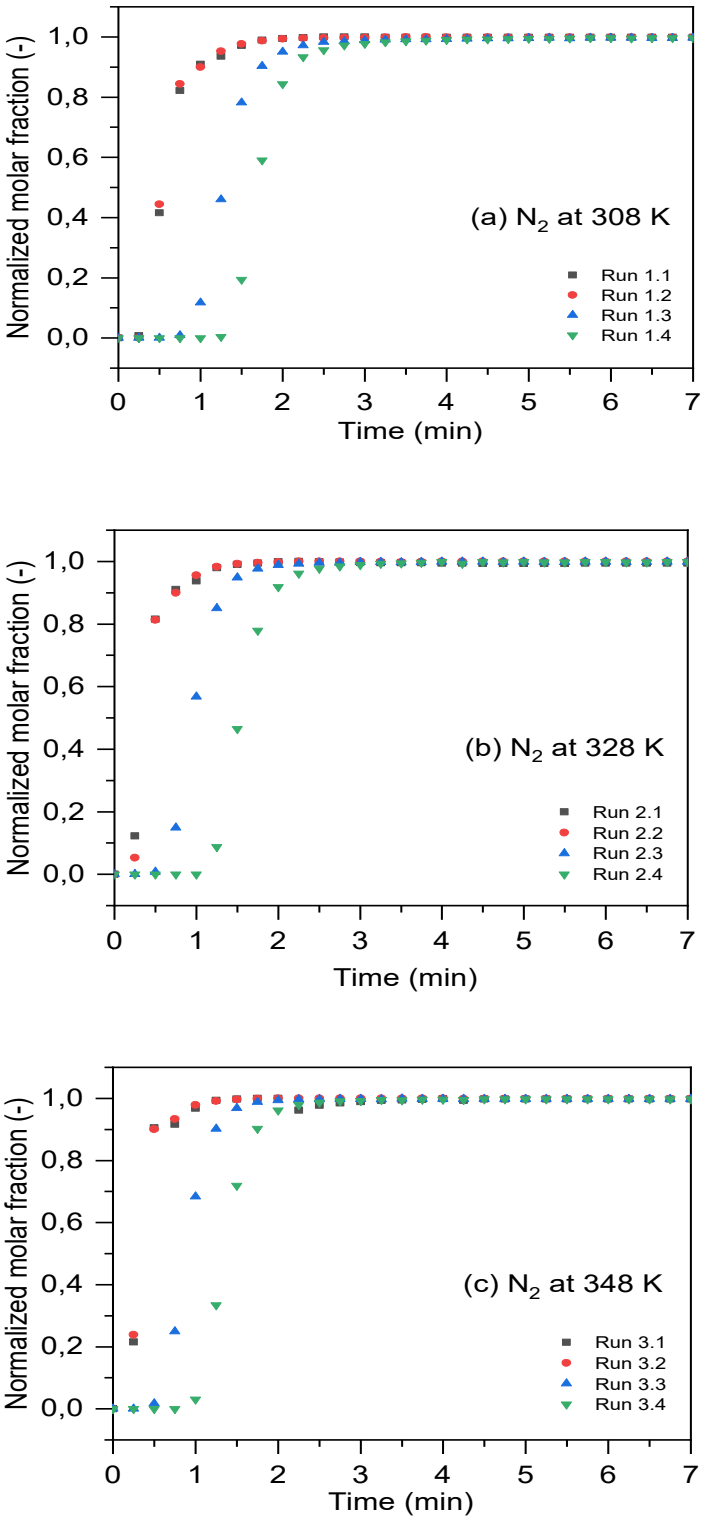

Figure 6. Real time breakthrough Curves of N_2 for powder-from 13X zeolite at 308 K,328 K and 348 K.